Application des techniques adaptatives à l'imagerie par résonance magnétique de perfusion

Marina Filipovic

Nancy-Université
Université Henri Poincaré

Ecole Doctorale BioSE (Biologie-Santé-Environnement)

Thèse

présentée et soutenue publiquement pour l'obtention du titre de

DOCTEUR DE L'UNIVERSITE HENRI POINCARE

Mention: Sciences de la Vie et de la Santé

par **Marina FILIPOVIĆ**

Application des techniques adaptatives à l'Imagerie par Résonance Magnétique de perfusion

le 6 juin 2011

Membres du jury :

Rapporteurs :	David Atkinson	Senior Lecturer, CeMIC, UCL, London, UK
	Christian Barillot	DR CNRS, IRISA, VisAGeS, Rennes
Examinateurs :	Klaas Pruessmann	Professeur, IBE, Université/ETH, Zurich
	Michel Claudon	PU/PH, CHU Nancy, Directeur de Thèse
	Pierre-Yves Marie	PU/PH, CHU Nancy
	Freddy Odille	Docteur d'Université, Laboratoire IADI

Laboratoire IADI - Imagerie Adaptative Diagnostique et Interventionnelle
INSERM U947, Nancy-Université U.H.P., CHU de Nancy - 54511
Vandoeuvre-Lès-Nancy

IADI

Nancy-Université
Université Henri Poincaré

Doctoral School BioSE (Biology-Health-Environment)

Thesis

presented and defended publicly for obtaining the title of

DOCTOR OF THE UNIVERSITY HENRI POINCARE

Mention: Life and Health Sciences

by **Marina FILIPOVIĆ**

Application of adaptive techniques to Magnetic Resonance Imaging of perfusion

on the 6th of July, 2011

Examination Panel:

Reviewers :	David Atkinson	Senior Lecturer, CeMIC, UCL, London, UK
	Christian Barillot	DR CNRS, IRISA, VisAGeS, Rennes
Examiners :	Klaas Pruessmann	Professor, IBE, University/ETH, Zurich
	Michel Claudon	PU/PH, CHU Nancy, PhD Supervisor
	Pierre-Yves Marie	PU/PH, CHU Nancy
	Freddy Odille	PhD, Laboratory IADI

Laboratory IADI - Adaptive Diagnostic and Interventional Imaging
INSERM U947, Nancy-Université U.H.P., CHU de Nancy - 54511
Vandoeuvre-Lès-Nancy

IADI

Remerciements

L'issue d'une thèse dépend de nombreux facteurs qui ne relèvent pas du travail personnel. L'encadrement, officiel ou officieux, est d'une importance primordiale, car les études doctorales sont autant une formation qu'un travail. Un environnement propice, au niveau scientifique et humain, est aussi nécessaire, ainsi qu'un support financier et administratif stable.

J'ai eu l'immense privilège de bénéficier de tous ces facteurs pendant mes études doctorales. Le laboratoire IADI dispose d'une ambiance scientifique et humaine remarquable, surtout grace à la direction du professeur Jacques Felbinger. Mes premiers remerciements vont naturellement à Jacques, pour sa bienveillance et sa générosité, et pour son investissement personnel auprès de chacun de ses employés. Sans être le directeur officiel, il s'est investi dans ma thèse, et encore plus dans mon avenir, et ceci tout en prenant en compte mes décisions personnelles qui allaient parfois à l'encontre de ses plans. Au début, il avait pris le risque de m'accepter en stage, sans connaître ma formation, et il s'est débattu jusqu'au bout avec le chaos administratif pour l'accueil des étrangers.

Concernant l'encadrement scientifique, ma plus grande reconnaissance va à Pierre-André Vuissoz, qui a été l'encadrant officieux de cette thèse. L'étendue de ses connaissances et son inventivité sont exceptionnels, et j'ai eu l'immense chance d'en profiter. Je ne compte plus le nombre de fois où je me sentais bloquée dans mon travail, sans issues, et qu'une conversation (d'une longueur notoire) avec Pierre-André m'a immédiatement ouvert différentes voies pour continuer. J'ai aussi particulièrement apprécié ses critiques, que ce soit pour des présentations, la rédaction d'article ou de thèse. Elles étaient très pertinentes, et m'ont appris qu'il était très important et très difficile de s'exprimer de façon claire, didactique et avec recul.

Je remercie tous les membres du jury de m'avoir fait honneur de leur présence: mon directeur de thèse, Michel Claudon, les rapporteurs, David Atkinson et Christian Barillot, qui m'ont fait part de remarques constructives sur mon manuscrit, le président du jury, Klaas Pruessmann, ainsi que Pierre-Yves Marie. Leurs remarques et questions pendant la soutenance étaient très intéressantes et édifiantes.

Je voudrais particulièrement remercier Freddy Odille, collègue et examinateur,

pour sa cordialité, au travail ou en dehors, et pour avoir été ouvert à toute question ou sollicitation, que ce soit à Nancy ou à Londres.

Je remercie bien sûr tous les gens avec qui j'ai partagé les pauses café au cours de ces 4 années: Julien et Romain pour leur jovialité dont ils animaient le labo; Laure pour de bons souvenirs de chambre partagée aux congrès; mon collègue de bureau, Brice, pour avoir supporté mes questions fréquentes et l'odeur de mes déjeuners exotiques; Damien pour son professionnalisme et sa gentillesse; Marine pour son dynamisme et sa cordialité; ainsi que Emilien, Maélène, Cédric, Anou, Lucas, Michelle, Marion, Hélène, Anne, Christophe, Z'hor, Slavisa, Gabriela, Emmanuelle, Céline, Mélanie, Pauline, Adnane, Tristan, et d'autres.

Mon séjour à Londres était une expérience merveilleuse. Je remercie Philip Batchelor, d'avoir permis et organisé cet échange, et pour sa cordialité et sa disponibilité pour diverses sollicitations et questions. Je remercie Sebastian Kozerke, pour les discussions et les données qu'il m'a fourni, ainsi que tous les gens de the Division of Imaging Sciences, King's College London.

Je remercie mes parents, d'avoir été un soutien inconditionnel depuis toujours, mon petit frère, qui pourra maintenant taquiner à volonté un docteur d'université, et toute ma famille. Je remercie Nicole et Francis Pierucci, pour leur soutien et immense gentillesse dès le début. Et ce serait presque ridicule de remercier en quelques mots, aussi beaux soient-ils, ma deuxième moitié, Antoine...

Abstract

Magnetic Resonance Imaging (MRI) requires tools for managing physiological and other motion of the patient. The generation of MR images consists of three steps: data acquisition with a pulse sequence, image reconstruction and image post-processing. Adaptive image reconstruction techniques aim at integrating motion information into the process of image generation from the acquired data, in order to compensate for motion-induced artefacts and problems. Dynamic contrast-enhanced (DCE) MRI is a technique designed for assessing the function of organs, by following dynamically the passage of a contrast agent in the body after a bolus injection. Motion-induced problems, especially in abdominal and thoracic DCE-MRI, consist of motion artefacts and misregistration. A new image reconstruction method, DCE-GRICS (Dynamic Contrast-Enhanced Generalized Reconstruction by Inversion of Coupled Systems), has been developed for solving these issues. Motion is estimated with a non rigid linear model based on physiological signals obtained from external sensors. Dynamic intensity changes caused by the passage of the contrast agent are described using a linear contrast change model based on B-splines. The method is applied and validated on myocardial perfusion imaging. Motion-induced inaccuracies in intensity-time curves are compensated, in order to allow for more reliable myocardial perfusion quantification by curve post-processing.

Résumé

L'Imagerie par Résonance Magnétique (IRM) nécessite des outils pour gérer le mouvement physiologique et autre du patient. La création des images par l'IRM comporte trois étapes: l'acquisition des données avec une séquence d'impulsions, la reconstruction d'images, et le post-traitement. Les techniques adaptatives de reconstruction d'images visent à intégrer des informations liées au mouvement dans le processus de génération d'images à partir de données acquises, ceci dans le but de compenser les artéfacts et problèmes provoqués par le mouvement. L'IRM dynamique avec rehaussement de contraste est une technique destinée à l'estimation de la fonction d'organes, en suivant le passage d'un produit de contrast dans le corps. Les problèmes dus au mouvement, surtout dans l'application thoraco-abdominale de cette technique, se présentent sous forme d'artéfacts de mouvement et de décalages. Une nouvelle méthode de reconstruction d'images, DCE-GRICS (Reconstruction généralisée dynamique avec rehaussement de contraste par inversion des systèmes couplés), a été développée pour résoudre ces problèmes. Le mouvement est estimé avec un modèle linéaire non rigide basé sur les signaux physiologiques issus de capteurs externes. Les changements d'intensité causés par le passage de l'agent de contraste sont rendus avec un modèle linéaire de changement de contraste basé sur les fonctions B-spline. Cette méthode a été appliquée et validée sur l'imagerie de la perfusion myocardique. Les inexactitudes causées par le mouvement dans les courbes intensité-temps sont compensées, afin de rendre plus fiable le post-tratement des courbes pour l'estimation de la perfusion myocardique.

Abbreviations and Notions

IADI	Imagerie Adaptative Diagnostique et Interventionnelle
ISMRM	International Society for Magnetic Resonance in Medicine
MRI	Magnetic Resonance Imaging
DCE	Dynamic Contrast-Enhanced
DSC	Dynamic Susceptibility Contrast
AIF	Arterial Input Function
ROI	Region of interest
ECG	Electrocardiogram/graph
RR interval	Interval between two R peaks in the ECG
TR	Repetition time
TE	Echo time
TD	Delay time
SAEC	Signal Analyser and Event Controller
SVD	Singular Value Decomposition
PCA	Principal Component Analysis
PSF	Point Spread Function
FOV	Field-of-view
SNR	Signal-to-noise ratio
SSFP	Steady State Free-Precession MRI pulse sequence
T	Tesla
T_1	Longitudinal relaxation time
R_1	Longitudinal relaxation rate
T_2	Transverse relaxation time
T_2^*	Transverse relaxation time including magnetic field inhomogeneities

Contents

List of Figures

List of Tables

Introduction

The importance of diagnostic imaging in medicine is constantly increasing. Imaging technology is advancing in parallel with new demands and requirements. Each imaging modality has its own aims and characteristics, so that different modalities are more often complementary than in competition. Magnetic resonance imaging (MRI) is a rather complex technique, from both technological and interpretative point of view. It is based on many assumptions: in practice, some of them are very good approximations of the reality, whereas some of them require corrections, depending on the application. One of the basic assumptions is the stationarity of the imaged object (human body): the object doesn't move and its intrinsic characteristics don't change. Motion has various sources: voluntary or involuntary movement of the patient, physiology (breathing, cardiac activity, peristalsis), etc. It may or may not require compensation and correction, depending on its nature and characteristics, and on the MRI technique employed. Corrections can be introduced in different stages of MR image generation: prospectively, before/during data acquisition, or retrospectively, in image reconstruction or image post-processing.

These doctoral studies were conducted in the Laboratory IADI (Adaptive, Diagnostic and Interventional Imaging), Nancy, France, except for 6 months spent in the Division of Imaging Sciences, King's College London, London.

The main activity of the IADI lab focuses on the management of motion in MRI. Developments range from hardware for motion measurement and for control of the MRI scanner, to software for motion compensation. Being situated at the University Hospital of Nancy-Brabois, the laboratory has access to two MRI scanners, a 1.5T and 3T (Signa HDxt, General Electric), which are used both for clinical examinations and research. The environment for these studies was very favourable from the start, since a significant support was already in place in the laboratory, in terms of hardware/software and accumulated knowledge. Previous work had dealt with sensors for measuring physiological motion (hardware development, correction of MRI-induced artefacts), with parallel imaging, adaptive ECG and respiratory gating/triggering, etc.

Notably, a new image reconstruction algorithm, GRICS, was developed in order to perform motion compensation based on physiological signals acquired

synchronously with MR data. However, the method was not directly applicable to all MRI techniques in need of motion compensation, such as abdominal and thoracic Dynamic Contrast-Enhanced (DCE) MRI. This MRI application is heavily disturbed by motion, in terms of image quality and quantitative analysis. These unsolved problems generated the subject of this thesis : extend and generalise GRICS in order to apply it to Dynamic Contrast-Enhanced MRI.

The Division of Imaging Sciences, King's College London, is a multi-disciplinary group working on different imaging modalities in medicine. Research topics range from chemical development of new contrast agents, through image acquisition to image post-processing. One of the subjects focuses on image reconstruction and motion compensation in MRI, thus being closely linked to the work in the IADI lab. Notably, considerable research deals with a new method for image reconstruction from undersampled data, applied to myocardial perfusion DCE-MRI. Therefore, a collaboration was put in place in order to combine image reconstruction with motion compensation, developed in the IADI lab, with image reconstruction from undersampled data implemented in the Division of Imaging Sciences.

The first part of this dissertation is dedicated to the state-of-the-art in different fields of science and research encompassed by the subject of this thesis:

1. General description of the imaging process, tools for generating images from data acquired with imaging devices, and the specific case of image reconstruction in MRI

2. The nature of motion occurring in human imaging, its various effects on MR images, and solutions proposed today for motion compensation

3. Theory of contrast agent kinetics and assesment of the perfusion of different organs using Dynamic Contrast-Enhanced MRI

The second part focuses on topics explored in the IADI laboratory, and on contributions and achievements of these doctoral studies:

1. Sensors for physiological motion, explored or developed in IADI, and signal analysis for new sensors done during these studies

2. Image reconstruction with motion compensation (GRICS), and the main achievement of this thesis: a new image reconstruction method (DCE-GRICS), designed for motion compensation of Dynamic Contrast-Enhanced MRI

3. Combination of DCE-GRICS with the accelerated image acquisition and reconstruction from undersampled data implemented in the Division of Imaging Sciences, which resulted in a new method, k-t GRICS, designed for motion compensation of accelerated Dynamic Contrast-Enhanced MRI

Finally, the prospect of this work is explored, in terms of future applications and developments.

Introduction

L'importance de l'imagerie diagnostique en médecine augmente constamment. La technologie avance en parallèle avec les besoins et les demandes nouvelles. Chaque modalité d'imagerie se distingue par ses propres objectifs et caractéristiques. Ainsi, les différentes modalités sont plus souvent complémentaires qu'en compétition. L'Imagerie par Résonance Magnétique (IRM) est une modalité d'imagerie plutôt complexe, du point de vue de la technologie et de l'interprétation. Elle est fondée sur plusieurs hypothèses: en pratique, certaines d'entre elles représentent une très bonne approximation de la réalité, tandis que d'autres peuvent devenir fausses et exigent des corrections. Une hypothèse fondamentale est celle sur la stationarité de l'objet imagé (corps human): l'object ne bouge pas et ses caractéristiques intrinsèques ne changent pas. Le mouvement provient de plusieurs sources: mouvement volontaire ou involontaire du patient, la physiologie (respiration, activité cardiaque, peristaltisme), etc. Des corrections/compensations peuvent être exigées, selon la nature du mouvement, selon ses caractéristiques, et selon la technique d'IRM utilisée. Les corrections peuvent être introduites dans différentes étapes de la génération d'images par IRM: de façon prospective, avant/pendant l'acquisition des données, ou retrospective, dans la reconstruction d'images, ou le post-traitement.

Ce doctorat s'est déroulé au sein du Laboratoire IADI (Imagerie Adaptative, Diagnostique et Interventionnelle), Nancy, France, hormis un séjour de 6 mois au Département des sciences d'imagerie, King's College London, à Londres.

L'activité principale du laboratoire IADI traite de la gestion du mouvement en IRM. Elle couvre différents domaines, depuis le matériel pour mesurer le mouvement et controller la machine d'IRM, jusqu'aux algorithmes de compensation de mouvement. Etant situé au Centre Hospitalier Universitaire (CHU) de Nancy-Brabois, le laboratoire a accès à deux machines d'IRM, une 1.5T and une 3T (Signa HDxt, General Electric). Elles sont partagées entre la clinique et la recherche. Ce doctorat était accueilli dans un environnement propice, car un support important avait déjà été mis en place au laboratoire, en matière de matériel/logiciels et de connaissances accumulées. Les travaux précédents traitaient de capteurs pour mesurer le mouvement physiologique (développement de matériel, correction des artéfacts causés par l'IRM), de l'imagerie parallèle, de la synchronisation adaptative

avec l'ECG et la respiration, etc.

Notamment, un nouvel algorithme de reconstruction d'image, GRICS, a été développé afin de compenser le mouvement à partir de signaux physiologiques acquis en parallèle avec les données d'IRM. Cependant, il n'était pas directement applicable à toute technique d'IRM ayant besoin de compensation de mouvement, comme par exemple l'IRM dynamique avec rehaussement de contraste thoraco-abdominale. Cette technique est fortement perturbée par le mouvement, en terme de qualité d'image et d'analyse quantitative. Ces problèmes non résolus ont créé le sujet de cette thèse: développer et généraliser GRICS afin de l'appliquer à l'IRM dynamique avec rehaussement de contraste.

Le Département des sciences d'imagerie, King's College London, est un groupe multi-disciplinaire qui travaille sur les différentes modalités d'imagerie en médecine. Les sujets de recherche varient du développement chimique de nouveaux agents de contraste, à travers l'acquisition d'images jusqu'au post-traitement. Une des thématiques est très proche du laboratoire IADI: elle concerne la reconstruction d'image et la compensation de mouvement en IRM. Notamment, des ressources importantes sont dédiées à la recherche basée sur une nouvelle méthode de reconstruction d'images à partir de données sous-échantillonées, appliquée à l'examen de la perfusion myocardique par l'IRM dynamique avec rehaussement de contraste. Par conséquent, une collaboration a été mise en place afin de combiner la reconstruction d'image avec compensation de mouvement, développée au laboratoire IADI, avec la reconstruction à partir de données sous-échantillonnées implémentée au Département des sciences d'imagerie.

La première partie de cette thèse est dédiée à l'état de l'art dans les différents domaines de science et de recherche englobés par le sujet de ce doctorat:

1. Description générale du processus d'imagerie, outils pour la génération d'images à partir des données acquises par les appareils d'imagerie, et le cas spécifique de la reconstruction d'images en IRM;

2. La nature du mouvement qui survient dans l'imagerie de l'humain, ses différents effets sur les images d'IRM, et les solutions proposées à ce jour pour la compensation de mouvement;

3. La théorie de la cinétique des agents de contraste, et l'évaluation de la perfusion d'organes par l'IRM dynamique avec rehaussement de contraste.

La deuxième partie traite des thématiques explorées au laboratoire IADI, et des contributions et résultats de ces études doctorales:

1. Capteurs du mouvement physiologique, explorés ou dévelopés au IADI, et l'analyse des signaux issus de nouveaux capteurs, effectuée dans le cadre de cette thèse;

2. La reconstruction d'image avec compensation de mouvement (GRICS), et la contribution principale de cette thèse: une nouvelle méthode de reconstruction d'image, DCE-GRICS, pour la compensation de mouvement de l'IRM dynamique avec rehaussement de contraste;

3. Combinaison de la méthode développée (DCE-GRICS) avec l'acquisition accélérée et la reconstruction à partir des données sous-échantillonées implementées au Département des sciences d'imagerie, ce qui a résulté en une nouvelle méthode de reconstruction d'image pour la compensation de mouvement de l'IRM dynamique accélérée avec rehaussement de contraste.

Finalement, les perspectives de ce travail sont explorées en terme de futures applications et développements.

Part I

Background and State-of-the-art

-

Chapter 1

Image Reconstruction in MRI

Imaging in general consists of three stages:

1. preparation of an object to be imaged
2. data acquisition by the imaging device (extraction of some relevant information about the object)
3. image reconstruction/deconvolution (processing of the acquired data into a 1-, 2-, or N-dimensional representation)

In short, some relevant characteristics of the imaged object are highlighted and adapted for human comprehension. Different imaging techniques aim at representing different characteristics of imaged objects, from outer-space matter to the anatomy and function of the human body. Magnetic resonance imaging (MRI) is a powerful imaging technique used in various scientific fields, and most importantly in medicine. Data acquisition and image reconstruction in MRI present a very interesting subject for research and optimisation.

1.1 Image reconstruction problem

Image/signal reconstruction/deconvolution is a widespread problem, posed in many different domains and applications. This entire section is inspired by Bertero and Boccacci [7].

1.1.1 Definition of ill-posed inverse problems

From a signal-processing point of view, imaging process is simply a filter: an input function of time or space, describing characteristics of interest of the imaged object, is convolved with the impulse response of the imaging device, in order to generate an output function, which is an approximation of the input. Calculating

the output of an imaging process is a *direct* problem, in the sense that it is oriented in the cause-effect direction: the input(cause) is known, a filter is applied to it, and the output(effect) is calculated. Designing an imaging device and physically acquiring data of interest from an imaged object is an entire subject which depends on different applications, and it won't be discussed here. The subject of this thesis focuses on the step of image reconstruction.

From a mathematical point of view, image reconstruction amounts to finding an image function $I(x)$ consistent with the measured/acquired data, according to a known imaging equation which describes the imaging device. Thus, it is an *inverse* problem, in the sense that it is oriented along the effect-cause direction: it consists in finding the unknown causes of known consequences. As such, it suffers from several difficulties, compared to direct problems. The filter transfer function, which represents the imaging device, is never bijective in practice: during the acquisition stage some amount of information is inevitably lost. The whole point of image reconstruction is to find an approximation of the input which is as physically realistic as possible, as consistent with the acquired data as possible, and try to recover as much lost information as possible.

Inverse problems are *ill-posed*, contrary to direct problems which are well-posed. These properties stem from the loss of information occurring in the cause-effect direction. *Ill-posedness* is a mathematical property of a problem which occurs when one or more of the following conditions are met:

1. the solution is not unique
2. the solution does not exist for arbitrary data
3. the solution is not continuously dependent on the data

In order to illustrate this, see Fig.1.1, let's define a metric space of objects to be imaged, called *object space* and denoted X. The imaging process is described with an operator A (standing for a transfer function/impulse response), and a certain influence of noise. Let's define a second metric space, called *image space* and denoted Y. The direct problem being well-posed, we can apply the operator A to each object from X and so calculate its corresponding *noise-free* image. Y contains both noise-free and noisy images.

The inverse problem consists in posing the equation $Ax = y$ and solving it for x with known A and y. The three possible sources of ill-posedness are translated by:

1. an image from Y may correspond to several objects from X (y_1)
2. not all images from Y have a corresponding object from X (y_2)
3. close images in Y may correspond to distant objects in X : when solving the inverse problem, a small shift in the image (caused by noise for instance) can correspond to a large shift in the solution (object) ($x_1 - y_1$ vs $x_3 - y_3$)

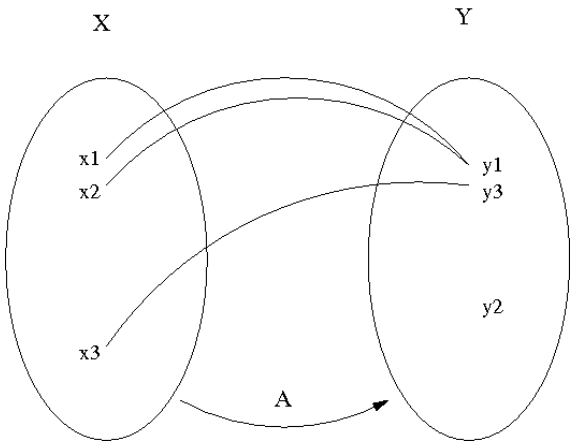

***Figure 1.1**: Illustration of an imaging problem*

All the objects whose image is zero are called *invisible objects*. The solution of the equation $Ax = y$ is unique if and only if the equation $Ax = 0$ has only the solution $x = 0$, which means that there is only one trivial invisible object.

An important detail to keep in mind when dealing with inverse problems is that, in practice, they are translated and solved in the discrete domain. The translation of properties from continuous to discrete domain is not straight-forward and continuous ill-posed problems might become even more ill-posed when translated to discrete domain. An inverse problem is usually formulated as a linear discrete problem. In the discrete case, error propagation from the data to the solution, or numerical stability of the problem, is translated by the condition number of the problem. When discretising an ill-posed problem, the condition number of the corresponding discrete problem can be very large, and the problem is called *ill-conditioned*. A problem with a condition number close to one is called *well-conditioned*. Continuous dependence of the solution on the data is necessary but not sufficient to guarantee numerical stability.

Most imaging devices, including MRI, are *band-limited* systems: the loss of information during data acquisition occurs in the spectral domain. The usually infinite spectral content of the imaged object is truncated and its image is band-limited in a band B. Therefore non-trivial invisible object exist and the solution is not unique.

1.1.2 Solution of ill-posed inverse problems

In the context of inverse problems in imaging, it is important to discard the notion of looking for the *right* solution, and start looking for the best approximation of the right solution. Various methods have been developed with this aim, and can be classified according to their point of view on the problem. The problem can

be posed as a deterministic or statistical imaging process. Deterministic approach neglects the random nature of noise. Statistical approach falls into two categories: either only noise, or both the imaged object and the noise are considered as realisations of a random process. The more random and non-linear the model is, the best is describes reality, and the more complicated for solving and dealing with it is.

When posing a problem with the aim of looking for an approximate solution, it is crucial to have a measure of how close, or far, the approximate solution is to the truth. The residual represents the difference between the approximate solution and the truth, and discrepancy is the norm of the residual, or in the discrete case simply the root mean-square error. Actually, inverse problems are often posed as a minimisation of this discrepancy.

Ill-posedness of an inverse problem is usually reduced by introducing some additional information, which is not present in the imaging equation itself. Such information is usually called *the prior*, because it represents some knowledge we have about the imaged object, which is not fully transmitted during the imaging process, and which can help directing the solution. For instance, it might be known from the physics of the imaged object that the function which describes it cannot be negative. Or another example, if the imaged object is reckoned a random variable, its probability distribution might be known roughly in advance. If the noise is taken into account, its probability distribution might also be known. Prior information is usually introduced in the equation of an inverse problem by means of *constraints*.

Usually the inverse problem is formulated as a functional (a mapping which associates a value to an object) to be minimised. Norms are used to prescribe the type of minimisation. Methods described here will focus mainly on the norm l_2 (least-squares norm) of functionals. This norm is convenient because it results in a linear Euler equation, and linear algebraic systems are rather easy to solve. However, it should be noted that other norms can be used, with different properties and different solving methods. L_p vector norm is defined as

$$\| x \|_p = \left(\sum_i |x_i|^p \right)^{\frac{1}{p}} \tag{1.1}$$

L_0 or L_∞ norm is the optimum norm for compression and imaging, because it translates sparsity: the sparser the vector the smaller its L_{inf} norm. Unfortunately it is almost never used because it is extremely difficult to minimise. However, it has been demonstrated that L_1 norm, which minimises the sum of absolute values of x, promotes sparsity, Donoho [22]. This norm is also more difficult to deal with, because it is non-linear.

1.1.2.1 Solution of deterministic problems

Least-squares solution , as its name suggests, is any solution that minimises the sum of squares or the l_2 normof an expression, here the data consistency term $Ax - y$:

$$min \parallel Ax - y \parallel_2 \tag{1.2}$$

If noise n is taken into account, $y = Ax + n$, and if it has a larger band than the band B of the operator A (which describes the imaging device), than the solution might not exist. The cure for this problem is to band-limit the image y to the band B, which is equivalent to solving the least-squares of equation $Ax = y$:

$$min \parallel Ax - y \parallel_2 \tag{1.3}$$

by transforming it into its Euler equation:

$$A^*Ax = A^*y \tag{1.4}$$

equivalent to $Ax = P_By$, where P_B is a band-limiting operator for out-of-band noise suppression, A^* is the adjoint of A, which is a generalisation of the Hermitian (conjugate transpose). Taking the Euler equation is a very straightforward standard method for minimising functionals. It consists in detecting the minimum by taking the derivative of the functional $\parallel Ax - y \parallel_2$, setting it to zero, and then solving that equation instead of the first one. Obviously this method will detect all the local minima, so that in general the solution won't be unique. In the context of band-limited systems, multiple minima derive from the fact that any addition of out-of-band signal to a solution results in another solution. If we're looking for the best possible, unique solution, and if no information is available about the out-of-band part of the object, it would be convenient to take the least-squares solution with the minimal norm, i.e. the solution with no out-of-band component. This solution is called the *generalised*, or *minimum-norm least-squares* solution. It is obtained by

$$x = A^\dagger y \tag{1.5}$$

where $A^\dagger$ is the Moore-Penrose inverse, or generalised inverse of A. It can be shown that $A^\dagger y = P_B x$, and that if $(A^H A)^{-1}$ exists,

$$A^\dagger = (A^H A)^{-1} A^H \tag{1.6}$$

Regularisation The term *Regularisation* was introduced by Tikhonov, and refers to a large group of methods for aiding the solution of ill-posed problems. The basic idea is to consider a family of approximate solutions depending on a positive parameter called *regularisation parameter*. In the case of least-squares solution, as mentioned previously, the functional to be minimised is (1.3). In order to restrain the solution to a family of approximate solutions, additional functionals are

formulated, and combined with the main one (data consistency term). For instance, a constraint functional can consist in minimising the energy of the solution : $\| x \|_2$.

Added constraint functionals determine the set of functions to which the approximate solution should belong, and usually they are chosen to form convex sets, because it is easier to minimise. They are usually combined with the method of *Lagrange multipliers*. Each functional is weighted with a regularisation parameter and summed in order to form one final functional, which is minimised by solving its Euler equation. The weighting of a functional with a regularisation parameters translates the importance given to that constraint, or the veracity of that assumption. The solution is therefore more or less forced to be compliant with those assumptions: it might be just slightly driven in their direction, which alleviates their incorrectness (constraints are always incorrect to some extent).

The regularisation method usually referred to as the *Tikhonov regularisation method*, is a least-squares solution with a constraint on the norm L_2 of the solution (minimisation of solution energy), yielding the following functional:

$$min\{\| Ax - y \|_2 + \mu \| x \|_2\} \tag{1.7}$$

with its Euler equation

$$(A^*A + \mu I)x = A^*y \tag{1.8}$$

In the case of noise-free images, this solution approximates the Moore-Penrose solution when μ tends to 0. It is however more useful to consider the case of noisy images. When noise is included in the equation, it can be shown that the norm of the residual, with respect to the Moore-Penrose solution, has two terms: the first one is a continuous and increasing function of the regularisation parameter μ, and the second one is the noise-propagation error, depending on both noise and μ, and is a continuous and decreasing function of μ. Therefore, the norm of the residual as a function of the regularisation parameter μ has a *semi-convergent* property, i.e. it decreases until some $\mu_{optimum}$, then increases. Therefore, there exists an optimal value of the regularisation parameter for which the approximation error is minimal. This parameter $\mu_{optimum}$ always exists, and yield the optimal solution offered by Tikhonov regularisation. It should be noted that in general, adding constraints to an inverse problem corresponds to filtering the solution in some manner. For instance, Tikhonov regularisation corresponds to applying a certain smoothing filter to the solution. It is important to keep this filtering property in mind when designing inverse problems, so as not to distance the solution from physical reality.

1.1.2.2 Solution of probabilistic problems

Maximum likelihood methods In this group of methods, noise is taken into account as a realisation of a random process, and the imaged object is considered deterministic. Hence, the image is also a realisation of a random process, and

its probability distribution is determined by a set of deterministic parameters characterising the imaged object, and by the probability distribution of noise. The problem is posed as

$$Ax + \nu = \rho \tag{1.9}$$

where ν is a random variable with a known probability density function. If the conditional probability density of the image ρ, given a value x, is formulated as a function of the unknown imaged object:

$$L(x) = p_\rho(y/x) \tag{1.10}$$

then the maximum likelihood estimate is the imaged object x which maximises this function. In the case of Gaussian noise with covariance matrix S_ν, this maximisation corresponds to the following minimisation:

$$min \parallel S_\nu^{-1}(Ax - y) \parallel_2 \tag{1.11}$$

which Euler equation becomes

$$A^* S_\nu^{-1} Ax = A^* S_\nu^{-1} y \tag{1.12}$$

It is obvious that in the case of white Gaussian noise, the ML estimate coincides with the least-squares solution of the problem. Noise information is included in the process, prior information can be added as deterministic constraints previously described, but there is no statistical prior information about the imaged object.

Bayesian approach In this approach both noise and the imaged object are considered as realisations of random processes. Therefore, prior statistical information about the noise and the imaged object can be exploited and included in the solution of the inverse problem. Thus, ill-posedness of the inverse problem can be reduced. The difference compared to deterministic regularisation methods is that prior information has a probabilistic nature here: if the general behaviour, i.e. the probability distribution, of the imaged object is known or just roughly estimated, it can be used to drive the solution in the right direction. In that manner, some previous experience, or some assumptions, can be easily integrated in the equation. These methods are rather efficient, and used in many different applications. The basic problem is usually posed as:

$$A\xi + \nu = \rho \tag{1.13}$$

Such a problem is fully described with the joint probability distribution of any two of the three random variables, for instance $p_{\xi\rho}$. Different configurations of the problem can be formulated according to the Bayes formula

$$p_\xi(x/y) = \frac{p_\rho(y/x)p_\xi(x)}{p_\rho(y)} \tag{1.14}$$

depending on which probabilities are known. If the distribution function of the imaged object, $p_\xi(x)$, is estimated or assumed, which is usually the case in practice, then the conditional probability $p_\rho(y/x)$ is needed for a full description of the problem. Usually the solution is estimated by finding x, the realisation of ξ, which:

- corresponds to the posterior expectation value of ξ, $E(x/y)$, or;
- maximises the posterior probability density function $p_\xi(x/y)$

.

Let's consider a simple case where all processes are Gaussian:

- the noise ν is a Gaussian random process with zero expectation value and covariance matrix S_ν;
- the imaged object ξ is a Gaussian random process with zero expectation value and covariance matrix S_ξ;
- the noise and the imaged object are independent random vectors, so that their cross-covariance matrix is 0.

In this case, the same estimate is obtained with the two usual methods, the posterior expectation or maximisation of the posterior density function. Without getting into details, it can be shown that this problem can be converted to the minimisation of the following functional:

$$min\{\| S_\nu^{-1}(Ax - y) \|_2 + \| S_\xi^{-1}x \|_2\} \tag{1.15}$$

which results in the following Euler equation:

$$\left(A^* S_\nu^{-1} A + S_\xi^{-1}\right)x = A^* S_\nu^{-1} y \tag{1.16}$$

The solution estimate x is given by $x = Ry$, where

$$R = \left(A^* S_\nu^{-1} A + S_\xi^{-1}\right)^{-1} A^* S_\nu^{-1} \tag{1.17}$$

equivalent to

$$S_\xi A^* \left(A S_\xi A^* + S_\nu\right)^{-1} \tag{1.18}$$

The operator R is known as the *Wiener filter*. The operator R can be expressed differently by transforming image and object spaces into Euclidean spaces equipped with weighted scalar products, the weighting matrices being $B = S_\xi^{-1}$ and $C = S_\nu^{-1}$:

$$R = \left(A^*_{weighted} A + I\right)^{-1} A^*_{weighted} \quad , \qquad A^*_{weighted} = B^{-1} A^* C \tag{1.19}$$

which is precisely the equation for Tikhonov regularisation, when image and object spaces are modified into weighted spaces as mentioned.

More complex random processes are a vast subject in signal processing, with many methods for their modelling, filtering and prediction, like (extended) Kalman filter and others.

1.1.2.3 Numerical algorithms

Numerical algorithms for solving algebraic systems of equations can be direct or iterative, linear or non-linear, depending on the complexity and linearity of the problem. For instance, calculating the Moore-Penrose inverse is a linear direct method, and Levenberg-Marquardt is an iterative linear least-squares method. Notions of numerical solution and analytical regularisation are rather entwined, because many numerical algorithms contain some kind of intrinsic regularisation. In most cases, iterative numerical algorithms have also the property of semi-convergence: when the number of iterations increases, the solution approaches the optimum one, and then moves away. Both numerical algorithms and analytical regularisation methods can usually be represented in a similar manner, by a filter and its impulse response.

Linear iterative methods fall into several categories, with different regularisation and convergence properties. Some main categories are gradient, steepest-descent, conjugate gradient methods, and generalised minimum residual (GMRES), Saad [80]. Conjugate gradient methods have convergence and regularisation properties similar to Tikhonov regularisation, where the number of iterations plays the role of the regularisation parameter. GMRES converges toward the Drazin inverse instead of the Moore-Penrose inverse, Ipsen and Meyer [38].

The choice of the appropriate numerical method for solving a given system of equations depends on the conditioning of the system, algorithm's convergence and regularisation characteristics, but also on the dimension of the problem and the resources. If the system of equations is very ill-conditioned, even with added regularisation constraints, iterative numerical algorithms may be preferred, because of the additional regularisation they provide. Also, when the problem size becomes large, direct solution may demand too much computing resources. In that case, iterative solution is preferred, because large operators aren't calculated explicitly at once.

There are also non-linear methods, intended for non-linear equations: in general they are more complex than linear methods, and require more calculation time and resources.

1.1.2.4 Singular value decomposition (SVD)

Singular value decomposition (SVD) is an extremely useful mathematical tool. It has found applications in many different settings, and provides interesting generalised points of view and explanations. Here it is presented in the context of inverse problems, and the Principal Component Analysis, which is used for signal processing.

Definition 1.1 *Let A be a rectangular matrix $M \times N$, with rank p; then, there exists a $p \times p$ diagonal matrix Σ, with positive diagonal elements, and two isometric*

matrices U and V, respectively $M \times p$ and $N \times p$, such that

$$A = U\Sigma V^* \tag{1.20}$$

The diagonal elements of the matrix Σ represent *singular values* of A, and they are monotonously non-increasing, $\sigma_1 \geq \sigma_2 \geq \ldots \geq \sigma_p$. The columns of V represent the eigenvectors of the covariance matrix $A^T A$. If A is an operator, which is the case here, then its properties can be illustrated with its singular value decomposition. For instance, the generalised or Moore-Penrose solution can be expressed as :

$$x^\dagger = \sum_{i=1}^{p} \frac{1}{\sigma_i}(y, u_i)v_i \tag{1.21}$$

This shows rather clearly that if A has many singular values very close to 0, instabilities will occur in the solution. The indicator of numerical stability, i.e. the condition number of A, is in this case $\frac{\sigma_1}{\sigma_p}$, and it will become very large if A has singular values very close to 0.

1.1.2.5 Principal Component Analysis (PCA)

Decomposition of A into its principal components is done by projecting A on the eigenvectors V of its covariance matrix:

$$P_c = AV = US \tag{1.22}$$

A can be thus expressed in terms of the coefficients P_c corresponding to each principal component (V columns):

$$A = P_c V^T \tag{1.23}$$

P_c is a dense matrix, but its largest dimension corresponds to the number of eigenvectors vectors in V. Since eigenvectors perform compaction of the information contained in A, A can be approximated with only the first $m < M$ eigenvectors in V. If so, A can be represented in a concise manner with only its m principal components coefficients in P_c. The principal components and their weights are mutually independent (orthogonal) in a deterministic sense.

1.2 Data acquisition and image reconstruction in MRI

In a nutshell, MRI is based on exciting magnetically the protons in the human body, and collecting the electro-magnetic signal subsequently emitted by the excited protons. Different types of excitation aim at causing responses reflecting

different characteristics of the human body. Image reconstruction is the process of transforming the acquired data into a 2 or 3 dimensional image of these characteristics of interest. This term is used in MRI, though in other imaging techniques it might be referred to as image deconvolution or restoration.

Once the response signal is collected by receiver coils, it is necessary to be able to distinguish which part of the signal comes from which part of the body. Hence, spatial information is encoded into the measured response during the data acquisition step. Without broaching the subject of physical details, the basic generation of an MR image consists in the following: the acquired proton response, i.e. the raw data, represents the Fourier transform of the final image intended for human appreciation. The raw data is defined in a complex, so-called k-space, which is linked by inverse Fourier Transform to the complex Euclidian image space. An example of k-space data (magnitude and phase) and the corresponding complex image (magnitude and phase) is given in Fig.1.2.

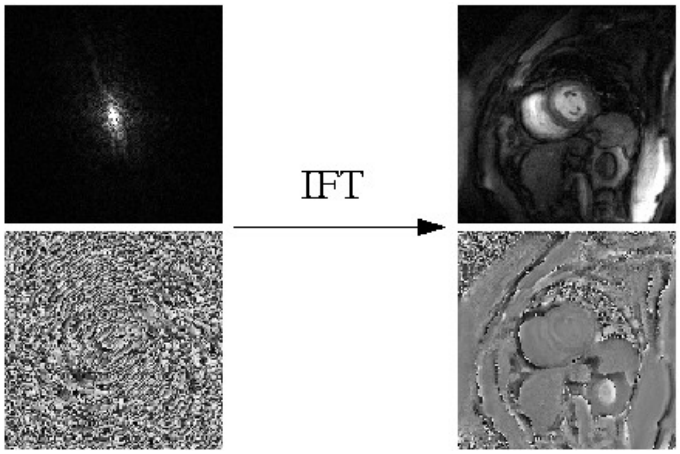

***Figure 1.2**: Magnitude(top) and phase(bottom) of k-space data acquired with MRI (left), and the corresponding image obtained by Inverse Fourier Transform (right)*

The basis vectors of the k-space are the spatial frequencies which correspond to the spatial dimensions in the image domain. Data points around the centre of k-space represent low spatial frequencies, i.e. image areas with small intensity change, whereas the border data points represent high spatial frequencies, i.e. image areas with high local changes in intensity.

From the point of view of MRI physics, the spatial frequency vectors in k-space correspond actually to proton precession frequency or proton precession phase vector: encoding of samples in k-space is done by changing the frequency and the phase of protons precession. In practice, a k-space line (one phase encoded and all frequency encoded samples) is acquired with a basic pulse sequence, during the so-called Repetition Time TR, ranging from 1ms to 10 seconds. A simplified diagram of a 2D basic pulse sequence is shown in Fig.1.3: the slice is selected by a gradient

in z direction and excited by an RF pulse, then phase encoding gradient is applied in y, and readout gradient is applied in x during the acquisition of the generated echo. This sequence is repeated every TR (repetition time) ms, as many times as there is phase encodes in the prescribed data matrix.

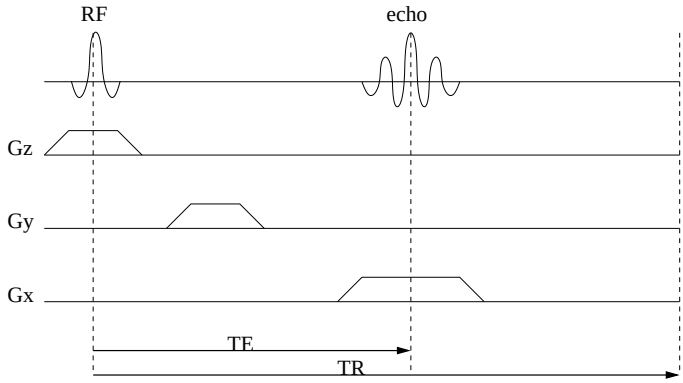

***Figure 1.3**: Simplified diagram of a 2D basic pulse sequence, repeated every TR (repetition time) ms (generation and acquisition of one echo, usually representing one phase encoded line): slice selection gradient in z, phase encoding gradient in y, and readout gradient during echo acquisition in x direction*

For a 2D image, one k-space dimension corresponds to the frequency encoding direction, and the other to phase encoding direction. For a 3D image, the third dimension corresponds to another phase encoding direction. There is an important difference between frequency and phase encoding. The echo, containing a full line in the frequency encoding direction, is sampled in a few milliseconds. Meanwhile, phase encoding is performed by applying an additional gradient in the spatial y direction, for a certain amount of time before the echo, so that only one phase encoded sample can be acquired in one TR interval by sampling one echo.

This is a rough description of a simple acquisition method, widely used in practice, though it is usually optimised and sometimes coupled with different, swifter methods, but that subject belongs to MR pulse sequence design. The basis vectors of k-space are often called frequency encoding or phase encoding directions, which is not to be confused with image frequency and phase obtained by Fourier Transform. The following descriptions of acquisition patterns for k-space data and corresponding reconstructions are inspired by Bernstein et al. [6].

It should be noted that a complex image is not directly comprehensible by humans. Therefore, it is usually the image magnitude which is presented to radiologists for visual appreciation, though quantitative image analysis strives to use both magnitude and phase. There is a multitude of variants of this basic principle for generating images with MRI, and even techniques based on different principles, but that is out of scope of this thesis.

1.2.1 Acquisition pattern for k-space data and corresponding reconstruction

The simplest and most common type of MR images is obtained by sampling the k-space data on a regular discrete Cartesian grid, Fig.1.4, and then applying Fast Fourier Transform (FFT) to obtain the image. A drawback of this data acquisition process is that it is entirely sequential, as described above: although frequency encoded samples are swiftly acquired, phase encoding takes a much longer time. Thus, acquisition time is usually roughly proportional to the number of necessary phase encoded samples in k-space. All the process being discrete, the number of samples in k-space equals the number of samples in image space. Hence it is obvious that the higher the requirements in image resolution, the larger the number of k-space samples, and the longer the acquisition time. It should be noted that swifter methods exist, but they have other issues, and their use depends on the application.

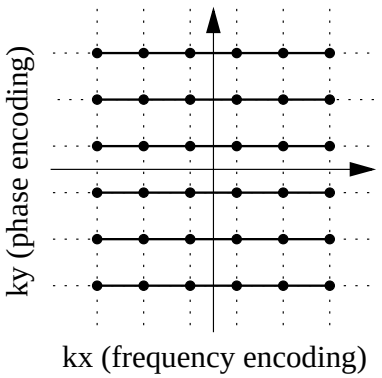

***Figure 1.4**: Cartesian acquisition of full k-space data matrix*

The acquisition time should be as short as possible, in order to shorten the duration of an MRI examination for the patient, reduce the cost and minimise the artefacts caused by the non-stationary nature of the imaged object (motion, physiological changes, etc.). In order to tackle this issue, both hardware and software are being optimised and developed: namely, considerable research is being done in the field of acquisition pattern design for k-space data and the corresponding image reconstruction techniques. The acquisition pattern and the reconstruction method are entirely coupled and cannot be treated separately.

Reducing the amount of acquired samples in k-space while maintaining image quality is an issue very closely linked to the field of image compression. The main question is: how to acquire the least amount of k-space data possible, and still obtain an image with satisfactory qualities (spatial and temporal resolution, signal to noise ratio (SNR), etc.)? Several techniques have been developed, some of them

being in daily use in clinical MRI examinations. Due to different acquisition times, acceleration in terms of frequency encoding is not much of an interest, so that the following methods will focus on acceleration in the phase encoding direction.

1.2.1.1 Acquisition pattern, its repercussions in image space and adapted reconstruction

There is one important image characteristic to keep in mind when designing acquisition patterns for MRI: the Fourier Transform of most realistic images one may come across is rather sparse. Most of the information in the spectral domain (k-space in MRI) is concentrated in the centre: the power of low spatial frequencies is much greater than the power of high spatial frequencies. However, diagnostic and medical information are more often than not contained in small details, so that regarding high spatial frequencies as less important may induce errors.

Not acquiring all the required samples in k-space can be described as a point-by-point multiplication of the full k-space data matrix with a binary mask matrix (ones for acquired samples and zeros for non-acquired ones). In image domain, this is equivalent to convolving the image obtained from a fully sampled k-space data with the Fourier Transform of the mask, which is usually referred to as the point spread function (PSF). The PSF is a very useful tool, because it describes how the image will be distorted after modifying the acquisition pattern.

The notion of aliasing emerges when the sampling frequency is below the Nyquist condition, i.e. below 2× the maximum frequency in the signal spectrum. In MRI, aliasing occurs when 1 out of N phase encoded lines is skipped or when the spacing between lines is increased. An example of 2× undersampling of a MR image is shown in Fig.1.6.

Partial Fourier is a widely used technique which consists of acquiring only a portion of k-space data in the phase encoding direction, as illustrated in Fig.1.7. In k-space, this corresponds to multiplying the full data matrix with a box function, and in the image domain it corresponds to convolving the full image with a sort of sinc function, causing some smoothing and Gibbs ringing in the image.

Homodyne is the standard reconstruction method for Partial Fourier acquisitions. A straightforward idea for recovering the full image is to assume that the image is real, hence that its Fourier transform (i.e. k-space data) is Hermitian conjugate symmetric, and replace the missing data with the conjugate of its (acquired) symmetric part. A development of this idea lead to the so-called Homodyne reconstruction technique, which is widely used for reconstructing Partial Fourier k-space data. The image is obtained by applying the following equation:

$$I(x) \approx Re\left[I_H(x)\frac{I_L(x)}{|I_L(x)|}\right] \tag{1.24}$$

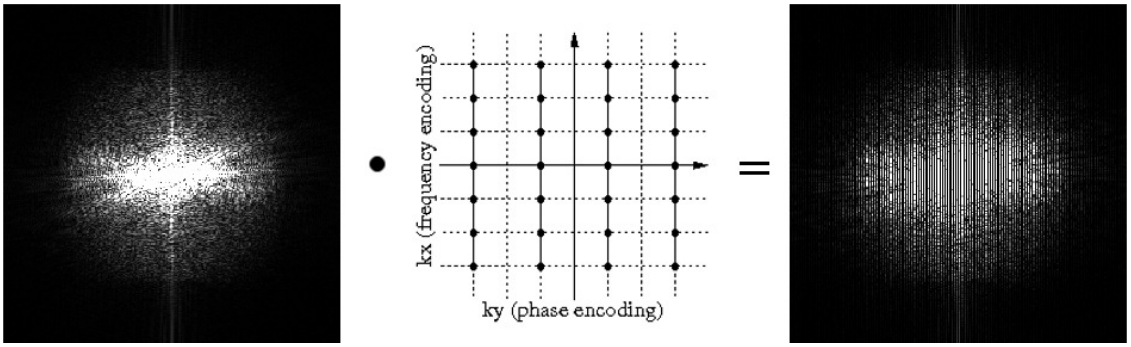

***Figure 1.5**: Undersampling (2×) in k-space: fully sampled k-space data, multiplied with the undersampling mask, result in 2x undersampled k-space data*

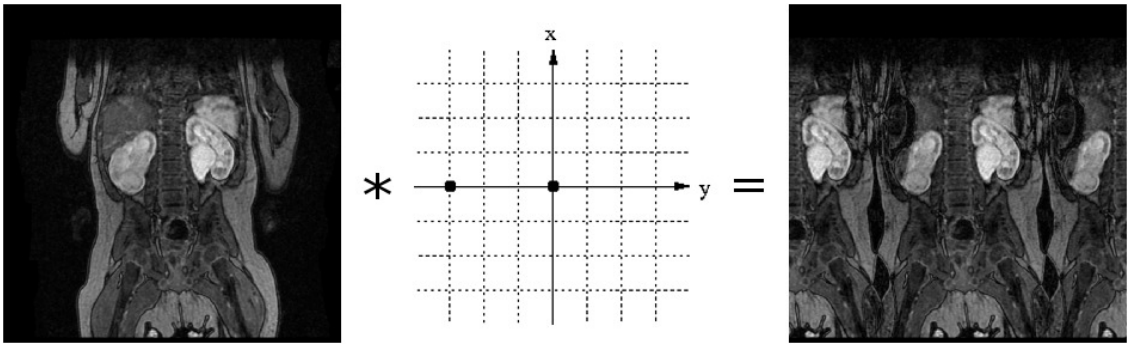

***Figure 1.6**: Effect of k-space undersampling (2×) in image domain: image obtained from fully sampled k-space data, convolved with the undersampling PSF, results in aliased image*

Partial Field Of View (FOV) is a technique for reducing the field of view in the phase encoding direction. When the FOV encompasses a much wider area than useful, it would be convenient to reduce the number of phase encodings, thus reducing the acquisition time, while keeping the initial resolution. This is achieved by increasing the spacing between phase encoded lines while keeping the same FOV dimension. In image space, this will result in aliasing, so that this method is useful only if aliased areas don't contain structures of interest, or if aliased areas are in the background of the imaged object.

Zero filling is a simple method for artificially increasing spatial or temporal resolution. The dimensions of k-space data are increased by adding zero samples. Padding k-space data with zeros corresponds to the ideal band-limited interpolation with a sinc function in the image space. This method is almost always used on commercial MRI scanners, in order to apparently increase the spatial resolution and render visual appreciation by radiologists easier. However, one should always be very careful when analysing interpolated images, because this increase in resolution

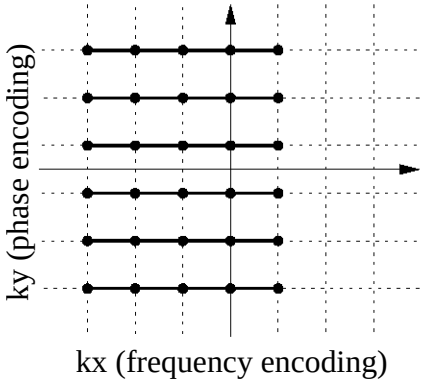

***Figure 1.7**: Partial Fourier acquisition*

is purely artificial. There is absolutely no additional information compared to the original image, and all the artefacts like Gibbs ringing, aliasing etc. are preserved. In addition, visual impression of better resolution might create false conclusions and make the observer trust more the information provided by the image. In lower (real) resolution images, unreliable MRI effects, like partial volume, noise, etc., are often more obvious.

Non Cartesian acquisition patterns are rather popular in research. Patterns with varying density are based on the idea of acquiring more samples in the central part, than in the borderline part of k-space. Since most of the spectral power is located near the centre, undersampling high spatial frequencies degrades the image much less than undersampling low spatial frequencies. Radial and spiral acquisition patterns are also used, although more in research than in clinical practice. Reconstruction of radial and spiral acquisitions includes also density compensation and gridding operation before applying FFT. Each sample is interpolated onto a Cartesian grid, because the final image is usually formed of square pixels and FFT is the quickest way of calculating Discrete Fourier Transform. However, they won't be investigated in this thesis since they weren't used in these studies and they present a subject of their own, in terms of acquisition patterns and reconstruction.

1.2.2 Parallel Imaging

The slow sequential nature of MRI data acquisition triggered the so-called parallel imaging methods. If the number of samples in k-space is reduced, then the number of spatial encodings is reduced. In order to obtain a proper image, this undersampling in k-space has to be compensated by an additional source of spatial

encoding. It is achieved by introducing a phased array of surface coils for signal reception, instead of one, usually body coil, Roemer et al. [76]. These phased-array coils are designed to have different spatial sensitivities. In that manner, each coil receives data for the same image synchronously, but with different spatial weightings, as illustrated in Fig.1.8. This provides a method for parallel spatial encoding. In the end, data acquisition is partially parallel, because a smaller part of spatial encoding is done by the receiver coils, and the rest is still done by the MR pulse sequence, in the manner described in 1.2.

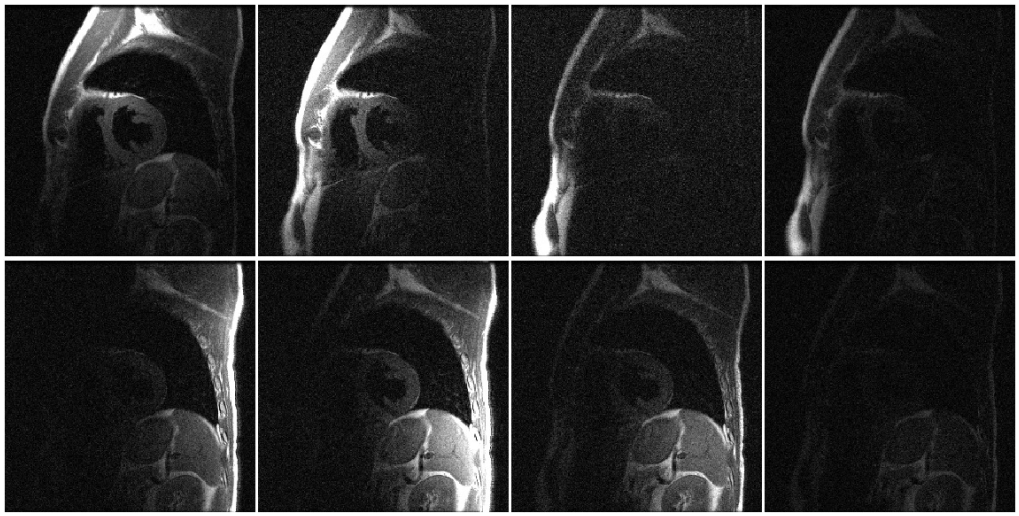

***Figure 1.8**: Image received synchronously by each phased-array coil, weighted with different spatial sensitivities*

Although this idea was implemented in the hardware quite early, a long time elapsed until image reconstruction methods, which take full advantage of it, emerged. At the beginning, the purpose of multiple coils was to improve the SNR: the k-space was fully sampled and the images obtained by each coil were combined with the square root of the sum of squares, Roemer et al. [76]. This resulted in an improved SNR of the final image. Later, other methods were developed with the aim of accelerating the acquisition. Their evolution was quite interesting: at first emerged several different methods, based on apparently different theoretical concepts. Two main reconstruction algorithms, SENSE, Pruessmann et al. [71] and GRAPPA, Griswold et al. [32], have been implemented on commercial MRI scanners. However, a few articles pointed out that all the methods based on SENSE and GRAPPA actually share the same theoretical concept, Wang [96], Yeh et al. [101]. Let's define a general framework for multi-coil acquisition.

In view of a general approach, regardless of image dimension(1-,2- or N-D), the spatial variable will be denoted by a position vector r and the corresponding k-space vector will be denoted k. If $c_c(r)$ represents the spatial sensitivity of coil c,

and $f(r)$ represents the complex MR image, K-space signal $S_c(k)$ obtained by the phased-array coil c can be expressed by:

$$S_c(k) = \int c_c(r)\rho(r)e^{-j2\pi rk}dr \tag{1.25}$$

The discretisation of parallel MR imaging process is not a trivial issue from a theoretical point of view, see Pruessmann et al. [71], and details won't be exposed here. Instead, from now on, the usual discrete formulation will be used.

Let upper-case variables represent the Fourier transform of the lower-case variables. Let N_c be the number of coils, N_k be the number of samples in the complete k-space data matrix, N_A the number of acquired samples, and ξ a binary matrix describing acquired samples in the Cartesian k-space (zeros for skipped and ones for acquired samples). Operator G is the gridding operator used in the case of non-Cartesian sampling, in order to make the use of FFT possible. The case when $N_A < N_k$ represents obviously k-space matrix undersampling: the matrix is not completely acquired, some arbitrary samples are missing. As mentioned previously, this results in an aliased image when simple standard reconstruction is used. The acquired k-space signal can be expressed in terms of matrix operators as:

$$S_{c,k} = G \cdot \xi \cdot FFT \cdot c \cdot f = Ef \tag{1.26}$$

E is usually referred to as the encoding matrix. This system of equations has $N_A N_c$ equations and N_k unknowns, so that it is over-determined when $N_k \leq N_c N_A$. It can be solved with the maximum likelihood method with Gaussian noise:

$$min \parallel S_\nu^{-1}(Ef - S) \parallel_2 \tag{1.27}$$

and its Euler equation (S_ν being often denoted by Ψ):

$$f = (E^H \Psi^{-1} E)^{-1} E^H \Psi^{-1} S \tag{1.28}$$

This is the solution provided by the generalised version of **SENSE** (Sensitivity Encoding) algorithm, Pruessmann et al. [72]. It is derived from the following assumptions about voxel shape functions: the ideal voxel shape is the Dirac impulse, and each actual voxel shape function is equal to 1 in the centre of that voxel, and 0 at other voxels' centres. In the case of simple Cartesian regular undersampling, where 1 line out of N is acquired and the PSF is easy to calculate, the previous system of equations can be simplified into an image domain formulation, Pruessmann et al. [71] as:

$$f = ((PSFc)^H \Psi^{-1} PSFc)^{-1} (PSFc)^H \Psi^{-1} s \tag{1.29}$$

The PSF operator is actually a mapping operator, selecting all the "true" pixels which participate in forming one aliased pixel. This system of equations can be split into many small problems, each problem representing the equation written for

one aliased pixel. Either as a whole or divided in blocks, this system of equations is usually rather small and well-conditioned, so that it can be solved in a direct manner: the inverse of $(PSFc)^H \Psi^{-1} (PSFc)$ is calculated directly as the Moore-Penrose inverse $(PSFc)^H \Psi^{-1} (PSFc)^\dagger$. This is the most frequent implementation of SENSE in the clinical setting, because of both the simplicity of the acquisition pattern, and the efficiency of the reconstruction.

In view of subsequent unification of different methods, Wang [96], it should be noted that the acquired k-space signal in (1.26) can be expressed also in terms of Fourier domain variables, with $FFT(cf)$ becoming $C * F$:

$$S = G \cdot \xi \cdot C_c * F_k \tag{1.30}$$

For simplicity, the following Cartesian case of this equation will be used for subsequent method comparison:

$$S_{c,k} = \xi \cdot \sum_{k'} C_{c,k-k'} F_{k'} \quad , \quad k \in A \quad , \quad c \in [1, \ldots, N_c] \tag{1.31}$$

This system has has $N_A N_c$ equations and N_k unknowns, so that it is over-determined when $N_k \leq N_c N_A$.

SMASH (SiMultaneous Acquisition of Spatial Harmonics), Sodickson and Manning [86] is a predecessor of **GRAPPA** (GeneRalised Autocalibrating Partially Parallel Acquisition), Griswold et al. [32], and consists in solving the equation (1.31) with an additional constraint on the positions and sensitivities of phased-array coils: there exist such weights $w_{h,c}$ which satisfy:

$$\sum_c w_{h,c} C_{c,k} \sim \delta_{h,k} \quad , or \quad \sum_c w_{h,c} c_{c,k} \sim e^{i2\pi hk} \quad , \quad \forall k \quad , \quad \forall h \in [1, \ldots, N_h] \tag{1.32}$$

This condition is a limiting factor in coil design, and means that there should exist certain linear combinations of the coil sensitivities which form the missing spatial coding harmonic $e^{i2\pi hk}$ in (1.25). In that manner, the coil sensitivities partially replace standard MR gradient encoding. Once the weights of a coil configuration satisfying the condition (1.32) are known, they can be integrated in (1.31), forming the following equation system:

$$F = wS \tag{1.33}$$

F is the Fourier transform of the final image, and w is a matrix operator with pre-determined weights as its elements. This equation actually shows that missing k-space lines are obtained by linear combinations of acquired k-space lines from different coils.

GRAPPA is an improved, generalised and auto-calibrated algorithm based on the SMASH principle. The SMASH constraint on the coil configuration is not explicitly required anymore, but the same idea persists: missing lines can be obtained by a linear combination of the acquired lines from different coils, owing to different coil sensitivities.

The acquisition pattern is designed so as to contain the so-called ACS (auto-calibration signal) lines in addition to the under-sampling pattern. These calibrating lines are used to determine the weights w by fitting. This results in an equation of the same type as for SMASH, $F = wS$, with the difference that F consists of Fourier domain images for each coil, instead of only the final image in Fourier domain, w are determined using the ACS lines, and S contains the acquired data for each coil.

The solution of this system of equations consists of full k-space data for each coil, which are subsequently Fourier transformed and combined using a sum of squares to generate the final image. The systems of equations for both the weights and the image are split into smaller problems, because only a certain neighbourhood of the ACS line or the missing line is considered. Indeed, relevant information about a missing line is contained mainly in a certain immediate neighbourhood of that line. The reconstruction is thus performed block-wise, and the size and shape of the blocks can be modified and optimised. If the problem is formulated by taking only one block containing the whole image, the system of equations can be transformed into generalised SENSE without noise.

The differences between GRAPPA and SENSE are:

- GRAPPA solves for the image in the Fourier domain, and SENSE solves for the image in the spatial domain
- SENSE requires explicit sensitivity coil functions, whereas GRAPPA requires additional auto-calibrating lines
- the noise propagation is different

However, they are both based on the same idea, further developed in what follows.

Coil configuration and k-space sampling must be such that (1.31) is solvable. The spatial sensitivity functions of phased-array coils are spatially limited functions, i.e. have a certain spatial aperture. Therefore, their spectrum is band-limited with a band $\sim 1/$spatial aperture. Consequently, the scan time reduction factor, i.e. the number of k-space samples that can be skipped, is limited by the number of adjacent samples encompassed by the band of coil sensitivity spectra, Wang [96], Yeh et al. [101]. This is a rather simplified description of the problem, without details about discretisation or other mathematical issues, but it illustrates rather well the general idea behind parallel imaging reconstruction. Trade-offs in coil configuration and

sensitivity functions have to allow for an acceptable solution of (1.31). From the GRAPPA point of view, the reconstruction neighbourhood and the conditioning of the problem posed for each missing line depend essentially on the band-widths of coil sensitivity spectra and their mutual independence. From the SENSE point of view, coil sensitivities have to cover distinct but complementary parts of the field of view for the system of equations to be well-conditioned.

The optimal number of coils, their geometry and positioning, is a common question, Larkman and Nunes [50]. It depends on the spatial encoding efficiency of a set of coils for a given imaged object, field-of-view and imaging plane. For instance, in cardiac imaging, phased-array coils are positioned around the patient, with the same number of coils beneath and above patient's thorax. Hence, the spatial encoding of phased-array coils will be differently efficient for short-axes, long-axes, or sagittal and axial images. Ideally, the undersampled (phase encoding) direction should be parallel to notable changes in coil sensitivities. In practice, it is not possible to adapt coil configuration to each subject and each imaging application, so that a compromise solution is chosen and used for several applications.

If the number of coils increases, the spatial encoding capacity should increase also, although not proportionally, because more coils might be correlated and provide similar information. However, the amount of data for reconstruction does increase proportionally, and requires more computing resources. Some work has been done on compacting information from a large number of coils (32 for instance), in order to extract only independent relevant information, and decrease the amount of data for the reconstruction, Doneva and Börnert [21], Huang et al. [36], Buehrer et al. [14]. A higher number of coils and subsequent information compaction is interesting also for improving the performance of parallel imaging for unsuitable imaging planes, since different subsets of coils might be efficient for different planes, Larkman and Nunes [50].

Noise propagation is a very important issue in parallel imaging. In the standard simple case of full k-space sampling, the noise in real and imaginary parts of the complex image reconstructed with a Fourier Transform, is also a Gaussian noise, as in receiver coils. In the case of under-sampling and parallel imaging reconstruction, noise propagation during reconstruction becomes much more complex, and the final SNR usually drops.

Noise propagation, or error-propagation as called in the context of inverse problems, is characterised here with the use of the *geometry(g)-factor*, Robson et al. [75]. This factor incorporates all the different influences on error propagation during reconstruction. As its name suggests, it depends strongly on the geometry of the phased-array coils, but also on the under-sampling factor, pattern design etc. The g-factor is defined as the ratio between the SNR of a fully sampled, optimal image, and the SNR of the accelerated image, and it is further divided by the square root of the acceleration factor R because less samples are available and less averaging occurs

in reconstruction (the optimal image refers to an image for which noise correlations in different coils are taken into account) :

$$g = \frac{SNR_{\ opt,unacc}}{SNR_{\ acc} \cdot \sqrt{R}} \tag{1.34}$$

This can be expressed in terms of noise standard deviations in the images:

$$g = \frac{\sqrt{N_{acc}}}{\sqrt{N_{opt,unacc}\ R}} \tag{1.35}$$

Calculating the g-factor, and SNR in general, is a rather problematic issue: they are spatially variant, their analytical calculation tends to be too complicated, and there is no consensus on a global standard method, Robson et al. [75].

1.2.3 Temporally optimised reconstruction methods

Another approach to acquiring less data, without compromising image quality, focuses on exploiting spatio-temporal correlations in dynamic MRI applications. Dynamic techniques aims at observing certain changes (induced by physiological motion, contrast agent injection, etc.), occurring in the field-of-view. When observing any MR dynamic image series, it can be noticed that temporal changes are rather localised, governed by some determined phenomena, and not very strong: the largest part of the information contained in each image frame is the same. This is very simply demonstrated by subtracting all the images in the series with the first image: the signal remaining in each image is very sparsified. Temporal correlation and redundancy of dynamically acquired data can be used in order to reduce the amount of necessary data. Many methods have been developed with this approach: the most used and implemented are described here, and a method of interest for these PhD studies, used during the visit to The Division of Imaging Sciences, KCL, London, is described in detail in 6.

1.2.3.1 TRICKS

Time-Resolved Imaging of Contrast KineticS (TRICKS), Korosec et al. [49], is based on the assumption that the greatest temporal changes occur in the central part of k-space. Therefore, the centre is sampled with a high temporal frequency, whereas peripheral parts (higher spatial frequencies) are sampled less frequently. A 3D k-space is divided into several concentric regions, with the central part acquired with the maximum temporal frequency, and the outer parts less and less frequently, as illustrated in a simple example in Fig.1.9.

Different sampling patterns based on this principle have been tested, Cartesian, Korosec et al. [49], radial, Du et al. [24], and spiral, Du and Bydder [23], combined

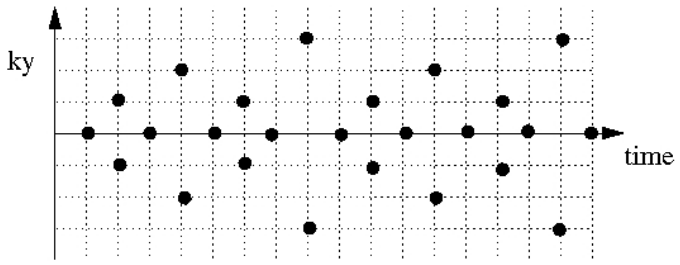

***Figure 1.9**: Illustration of the idea behind TRICKS (each point represents a full line in frequency encoding direction): temporal pattern for sampling in phase encoding direction, with central lines acquired most often, and the higher the spatial frequency, the rarer the sampling)*

with Cartesian. The reconstruction is performed with a sliding window technique: one temporal image is reconstructed from surrounding acquired data. In other words, interpolation is performed, either zero-filling, linear, cubic interpolation etc. Different interpolations, with different temporal filtering properties have been tested. The main application for algorithms based on TRICKS is the contrast-enhanced MR angiography of lower limbs, Du et al. [24] and abdominal (renal) and pulmonary vasculature, Du and Bydder [23]. Temporal and spatial resolutions depend on the implementation of TRICKS (sampling pattern, Cartesian or radial/spiral) and application. Reported temporal resolution range from 1/1s, Du and Bydder [23], to 1/5s, Du et al. [24].

1.2.3.2 UNFOLD

UNaliasing by Fourier-encoding the OverLaps using the temporal Dimension (UNFOLD), Madore et al. [54], was an important step for the development of optimised spatio-temporal sampling patterns. Although not stated explicitly at first, UNFOLD uses a sheared-grid sampling pattern in $k-t$ domain, Tsao [90]: for a given signal support in $x-f$ domain, the sampling pattern in $k-t$ domain is optimised so that temporal aliasing does not cause signal overlapping in $x-f$ space, as illustrated in Fig.1.10.

Since there is no signal overlapping, original data can be easily extracted by adapted filtering. In this manner, the same images are obtained with 2x less data. Obviously, this strategy depends completely on the shape of the signal support in $x-f$ domain, and has to be adapted, if possible, to different MRI applications. UNFOLD was applied to ECG-triggered dynamic cardiac imaging, where all temporal frequency bandwidth comes from the respiratory motion of the heart and surrounding organs, Madore et al. [54]: the signal support in $x-f$ space looks roughly like in Fig.1.10, with large bandwidth in f in the centre, in the region of the heart, and lower bandwidth elsewhere. This method was also

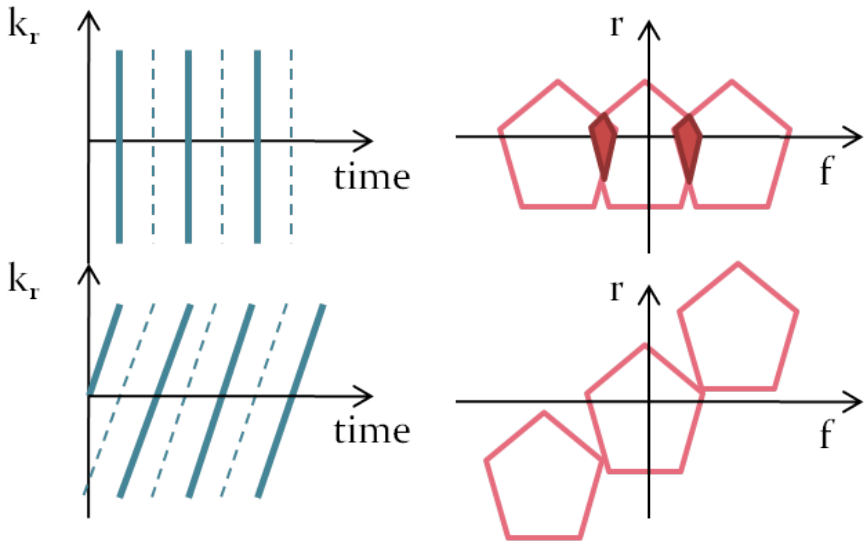

***Figure 1.10**: Undersampling in time results in aliasing in the temporal frequency direction (up). UNFOLD uses the sheared-grid sampling pattern, which PSF avoids signal overlap, allowing for signal recovery by simple filtering (bottom).*

applied to functional MRI, where changes induced by the paradigm have specific pre-determined temporal spectre. UNFOLD was combined with parallel imaging in Madore [53] and Kellman et al. [47].

1.2.3.3 Other methods

Other methods have been developed, many of them with the tendency of coupling temporally optimised imaging with parallel imaging. For instance, GRAPPA has been upgraded from a temporal point of view into TGRAPPA, Breuer et al. [12], and *k-t*GRAPPA, Huang et al. [35]. *k-t* BLAST was developed and coupled with SENSE into *k-t*SENSE, Tsao et al. [92], and generated numerous optimisations and applications. This method is implemented on several sites cooperating with the Division of Imaging Sciences, King's College London, and will be described in detail in 6, together with the work done during the stay in London. Another research direction in minimising the quantity of data that need to be acquired is based on compressed sensing, Donoho [22], and has been introduced in MRI in Lustig et al. [52]. In short, the idea is to acquire data in a random manner, find a sparsifying transform for the image, and minimise the L_1 norm of a functional containing data and the sparsifying transform.

1.3 Synopsis

Image reconstruction in MRI is an inverse problem, usually ill-posed. Theory and tools for solving such problems are widespread and deal with equation solving, minimisations, random processes etc. MRI is a rather particular case, in the sense that data are acquired in the so-called k-space, or Fourier Transform domain of the final (spatial) image. Optimisation and research in MR image reconstruction follow several directions: acceleration of data acquisition by reducing the quantity of required data (parallel imaging, temporally optimised imaging, methods based on image compression, etc), and compensation of various imperfections and artefacts in the image. These doctoral studies focused on introducing motion compensation in the process of image reconstruction, in order to correct for motion-induced problems in Dynamic Contrast-Enhanced MRI. The nature and influence of motion in MRI is described in the following chapter, as well as existing strategies for motion management.

Chapter 2

Motion in MRI

The generation of MR images relies on various theoretical approximations and assumptions, Haacke [33]. For instance, the imaged voxel is deemed homogeneous, in terms of proton density as well as T1 and T2 relaxation times, and its intrinsic properties are reckoned stationary. This implies, among other things, that the voxel is static, that it does not move. Obviously, a live organism is in perpetual motion, from the microscopic biochemical to the macroscopic body level.

When making approximations, it is crucial to observe phenomena with respect to a scale: motion causing considerable changes every 2s can be neglected if signal generation and acquisition takes 2ms, or on the contrary very rapid motion must be taken into account in each step of signal generation and acquisition. Since MR signal equations (for static imaged objects) are complex even when simplified, integrating the influence of (unknown) motion in these equations was theoretically explored only for some simple cases, such as rigid, constant velocity, or periodic motion.

Theoretical and practical estimates of motion influence have been investigated, and their application has two rather opposite aspects: they can be used in order to compensate for motion effects and obtain motion-free imaging, or they can be used with the aim of actually analysing the motion itself. Both aspects are useful for medical interpretation.

2.1 Motion types

On the molecular level, motion of protons is mostly due to Brownian motion, diffusion of water, exchange of chemicals etc. Whereas some applications actually exploit these phenomena, such as diffusion MRI, they can be neglected in most usual (macroscopic proton, T1 or T2 weighted) MRI applications. Since these PhD studies deal with these most used techniques, only macroscopic motion will be of interest.

2.1.1 Voluntary and involuntary body motion

During an MRI examination, patients usually spend a rather long time (30-45 min) in the MRI bore. They have to lie still in the MRI tunnel, usually in a supine position: sometimes they have to hold their hands above the head, sometimes a prone position on hands and knees is required etc. Therefore, an MRI examination can be more or less uncomfortable, especially for (usually) ill patients: voluntary movements, aimed at a more comfortable position, can occur. Patients are advised not to move, especially during pulse sequence play-outs, and although in most cases patients cooperation is satisfactory, movements can happen and compromise the examination to some extent. This is mostly the issue with children, who are less cooperative. In some cases, where lying still is crucial for the quality of MR images, small children, and mostly babies, are anaesthetised, which is efficient but not highly desirable: anaesthesia implies risks and constant monitoring of the patient throughout the examination. Involuntary body motion occurs mostly in patients with neurological diseases, where uncontrollable movements of the head or the extremities compromise the outcome of the examination.

2.1.2 Physiological motion

Macroscopic motion inside the human body is due to physiological processes, such as supply in oxygen (breathing), supply in blood (cardiac activity and blood circulation), nutrients processing (stomach and bowels movement), etc. They are treated separately in what follows, with respect to their temporal profile and influence on imaging. Some global characteristics of physiological motion, which are of interest in MRI, are:

- pseudo-periodicity: approximately the same movement is repeated in time, which makes measurement, modelling and prediction easier;
- strong variability among subjects: even though the function and anatomy are extremely similar in the majority of healthy subjects, there are slight differences in movements that are difficult to model and predict;
- influence of pathology: by introducing changes in function or morphology, pathologies usually have a direct or indirect impact on the movement of organs; the variability of this change in motion is even greater than in healthy subjects, but information about this pathological motion can also be used for medical decisions.

2.1.2.1 Breathing

Breathing is the process of lung filling/emptying with air. It is coupled with the motion of a number of surrounding organs: the chest expands and deflates,

the diaphragm moves in the superior-inferior direction, the liver follows partially, kidneys move mostly in the superior-inferior and slightly in the anterior-posterior direction, heart motion has a component caused by breathing etc. It is maybe the physiological motion with the simplest temporal shape and the largest amplitudes.

The motion of the diaphragm is often used to represent breathing motion. In the case of regular normal breathing, the movement of a point on the diaphragm plotted against time, as in Fig.2.1, resembles slightly a sinusoid, with a period ranging from 3 to 5s, and a spectral bandwidth of around 1Hz or less. The end of expiration tends to present a short pause before next inspiration, making expiratory peaks slightly larger than inspiratory peaks. Period and amplitude of the signal vary slightly in time. The breathing pattern can be very different from this regular form, because it depends on many factors: stress, pathology, load of devices positioned on and around the patient etc.

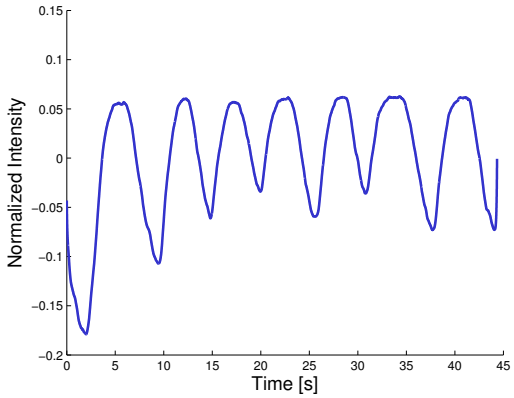

***Figure 2.1**: Motion of the diaphragm in normal free breathing*

Studies have been conducted with the aim of describing and assessing respiratory motion in thoracic and abdominal organs (lungs, diaphragm, liver, kidneys), von Siebenthal et al. [95], Blackall et al. [8]: peak displacement values in different directions have been reported.

Special attention has been paid to the respiratory component of the motion of the heart. The following characteristics have been highlighted:

- inspiratory or expiratory breath hold positions don't correspond in the general case to inspiratory or expiratory physiological positions during free-breathing, Scott et al. [84];
- a continuous drift in the diaphragm position sometimes occurs during breath hold Jahnke et al. [39];
- respiration has an influence on heart position and shape and affects cardiac activity, Thompson and McVeigh [88], Raper et al. [74];

- the relationship between breathing (represented by the displacement of the diaphragm), and the respiratory component of cardiac motion is hysteretic, subject specific, and can be sometimes approximated as linear, Nehrke et al. [58].

Breathing motion is rather slow when compared to the duration of signal(echo) generation and acquisition (the basic pulse sequence or TR interval), so that its effects can be neglected during the application of gradients, between encoding and echo collection etc. It can be an issue when considering motion between two phase encoding steps, especially in slow spin-echo based pulse sequences where TR is rather long. It is almost always an issue when considering motion between successive images.

2.1.2.2 Cardiac activity

Cardiac activity comprises an electrical, mechanical and blood circulation aspect. An electrical wave propagates through the heart, causing a contraction of the heart muscle (myocardium), and blood pumping. The electrical signal is usually measured by ElectroCardioGraphy (ECG). Depending on the placement of the electrodes, the signal is slightly different, though its general form resembles Fig.2.2: the R wave corresponds to the beginning of the systole (contraction of the heart, ejection of blood into arteries), and the flatter interval corresponds to diastole (relaxation of the myocardium).

In healthy subjects, ECG (ElectroCardioGramm) has a period ranging from 0.6 to 1s (60-100 heart beats/min). Changes in shape and duration of different cycles (RR intervals) can be large, between subjects and even for one same subject. In pathological subjects, numerous additional distortions can occur. In addition, the heart beat can be much higher than standard values, for instance in children, who usually have a quicker heart beat than adults, and in MRI examinations under effort or stress.

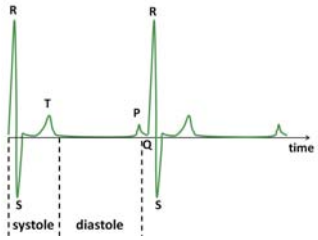

Figure 2.2: *Schematic illustration of an electrocardiogramm: systole (RST) corresponds to the contraction of the myocardium and ejection of blood into the aorta, and diastole (TP) corresponds to the relaxation of the myocardium*

As reviewed in Scott et al. [84], motion of the left ventricle (LV), induced by cardiac activity during systole, can be roughly divided into three major components:

longitudinal shortening (basal to apex, with apex being rather stationary), radial contraction, and opposite hand rotation of the apex relative to the base. The structure and motion of the right ventricle (RV) has been studied to a lesser extent, but movement of the free wall is primarily longitudinal with an element of radial contraction toward the apex and anterior section.

Both systole and diastole present a certain interval of time where the heart is almost static: these quiescent intervals are usually longer in diastole (150-200ms) than in systole (60-80ms), though there is a very high variability between subjects. When the heart beat rises, systolic plateau is affected less than the diastolic one: the shortening of RR period is absorbed mostly by diastole, so that imaging in systole might become more interesting in some cases, Fernandez et al. [28].

Being more rapid than breathing, motion induced by cardiac activity has a more problematic impact on MRI: although it can also be mostly neglected during echo generation and acquisition, it must be taken into account between phase encoding steps and beyond.

2.1.2.3 Peristaltic motion

Peristaltic motion concerns bowels and some other abdominal organs: it is a radially symmetrical contraction and relaxation of muscles, which propagates in a wave down the muscular tube. It is not as explored and exploited as breathing or cardiac activity. MRI has difficulties imaging air/tissue and air/water interfaces because of large differences in magnetic susceptibilities. Bowels are made of a multitude of such small interfaces. However, this field of application is in development, with an interest in the quantification and analysis of bowel motion, or compensation of motion artefacts, Zimmermann and Al-Hawary [104].

2.2 Effect of motion on MRI

Motion of imaged objects is independent of MRI data acquisition, so that it can occur during any part of pulse sequence play-out. The corruption of acquired data will be different depending on the part of the pulse sequence that has been affected. The theoretical approach for estimating motion effects consists in first describing the motion with an equation, then integrating it in the equation of MR signal generation, and finally trying to solve for the desired image. Obviously, the first step implies that the motion is known, which is never really the case: in practice, motion can sometimes be measured more or less accurately, it can be predicted with a certain error, but it can never be known exactly. Even if it was known, an accurate image corresponding to the imaged object could be recovered only in some simple cases. The most obvious case where it would be impossible to recover an image is when the imaged tissue moves out of the field of view and become invisible

to the pulse sequence. Besides, signal equations for currently used sequences are extremely complicated due to many small optimisations, such as gradient forms, phase compensations, optimised RF pulses, RF or gradient spoiling, steady-state signal etc., Bernstein et al. [6].

The effect of motion has been theoretically investigated for some simple cases: constant velocity or sinusoidal motion in standard proton density MRI, with a simple Cartesian acquisition, Ehman and Felmlee [25], Wood and Henkelman [100]. Though simplified, this provides an intuitive insight into more complex motion effects for more complex acquisitions, under a certain limit. As described in 1.2.1, a basic pulse sequence is designed for the generation and acquisition of one echo, which corresponds (in Cartesian sampling) to one line in the frequency-encoding direction in k-space. Motion can occur and corrupt data in the following parts of the imaging process:

1. during a basic pulse sequence (acquisition of one line in the frequency encoding direction)

2. between successive repetitions of basic pulse sequences (successive phase encodings)

3. between successive repetitions of the entire pulse sequence (acquisitions of entire images)

2.2.1 Motion during a basic pulse sequence (intra TR interval)

Motion can cause issues in different parts of a basic pulse sequence: during the application of the read-out gradient, slice selecting gradient, or between the application of phase encoding gradient and echo sampling, Haacke [33]. All frequency encoded samples for one phase encode are acquired during the sampling of an echo, while the read-out gradient is being applied.

Constant velocity motion between individual frequency encoded samples (during the read-out gradient) results in image phase changes. Motion with a velocity constant during the read-out, but differing for each phase encoding step, results in the aliasing of the moving structure in the phase encoding direction. In the human body, the only motion rapid enough to cause problems during gradient application of a few milliseconds is blood. Therefore, as soon as vessels are being imaged, these effects should be taken into account. Constant velocity motion is usually compensated for by designing read-out and slice selecting gradients with a null first moment.

In MRI applications explored during these doctoral studies, the influence of motion during the play-out of a basic pulse sequence was negligible, and wasn't taken into account.

2.2.2 Motion between successive phase encoding steps (inter TR interval)

Let's assume that each phase encoded sample is acquired instantaneously: then, only the impact of motion occurring between those instantaneous acquisitions is of interest. This is a reasonable assumption in most applications, because phase encoding and sample acquisition are performed in a rather small part of a basic pulse sequence, other parts being needed for the recovery of initial magnetisation. Therefore, one can reckon that two phase encoded samples are acquired instantaneously with a temporal spacing of TR. Hence, the impact of motion will be determined by the rapidity of different motion-induced changes with respect to TR.

Obviously, the effect of random motion of each voxel cannot be investigated in its entirety, because of too many possibilities, and because of the lack of accurate motion measuring. Therefore, only some simplified cases, to which current applications can often be reduced, have been investigated. Firstly, rigid motion will be investigated through cases of translational and rotational motion. Secondly, pseudo-periodic motion will be investigated, through cases of ideal sinusoidal motion in phase or frequency encoding direction.

It should be noted that any type of motion, in any direction, can be decomposed in the Fourier series, i.e. in the sum of periodic sinusoidal displacements. Therefore, calculating the impact of sinusoidal displacement, in frequency or phase-encode dimension, gives an approximate insight into motion-related corruption of MRI, especially in the case of pseudo-periodic physiological motion (it is less useful for non-periodic random motion because the latter has infinite number of Fourier components).

2.2.2.1 Rigid motion

Rigid motion denotes a combination of translational and rotational motion of the whole imaged object: all the structures contained in the field-of-view move in the same translational/rotational manner. This situation can occur in some applications, for instance in brain imaging, where head movements can be approximated as rigid. However, it is rather far from reality in the case of cardiac and abdominal imaging.

If the imaged object performs a translation of Δr, r being any image domain spatial direction, between acquisitions of two phase encoded lines, it can be deduced from basic properties of the Fourier Transform that the second k-space line will be multiplied by the phase factor $\exp(j\frac{2\pi\Delta r k_r}{N_r})$, compared to the first line, Ehman and Felmlee [25]. Different translations between each phase encoded line will cause different phase changes for each line, so that the phase of the final k-space data will be corrupted.

If the imaged object performs a rotation by an angle θ, with respect to a point (for instance the centre of the image), between acquisitions of two phase encoded lines, the second line will belong to a different k-space, rotated with respect to the original k-space in the same way the imaged object was rotated with respect to its original position, Korin et al. [48].

2.2.2.2 Periodic motion

Effects of sinusoidal motion of the whole field-of-view, in both frequency and phase encoding directions, was explored in Wood and Henkelman [100]. Theoretical motion point spread functions were determined. They represent a simplified case of the effect of breathing motion, and explain the origin of breathing artefacts seen in clinical practice. These results can be generalised to the more realistic case where several structures are present in the field-of-view and move in a different periodic manner (or don't move at all). Each structure will exhibit its own motion point spread function, because the Fourier transform is a linear operation, and an MR image can be represented as the sum of differently moving structures.

Frequency encoding direction: periodic motion of the whole field-of-view in the x direction, with a frequency F, amplitude A and starting phase ϕ_x, can be described with:

$$x = x_0 + A\sin(2\pi FT + \phi_x) \tag{2.1}$$

Integrating this motion into a standard MR image equation results in an image with two components: the image without motion effects, and the following additional artefactual term (C_{0-2} contain parameters for motion and acquisition):

$$\begin{aligned} P(x,y) =& C_0\{\delta(x-x_0)\delta(y-y_0)\} *_x *_y \\ & \sum_{m=-\inf}^{\inf} \exp(im\phi_x)\big\{\delta(x - C_1 m) *_x F_{x,m}\big\}\delta(y + C_2 m) \end{aligned} \tag{2.2}$$

$$F_{x,m} = \begin{cases} \frac{2(-i)^m T_m(x/A)}{\gamma G_x (A^2 - x^2)^{1/2}} & |x| < A \\ 0 & |x| > A \end{cases} \tag{2.3}$$

This equation shows that the original image convolved with $F_{x,m}$ will appear at positions in x direction $C_1 m$ and y direction $C_2 m$. If parameters are tuned for a simple acquisition and breathing periodic motion, the shifts in x direction are almost negligible, $\sim \mu m$, whereas shifts in y direction are bigger than mm and are clearly visible. The convolution with $F_{x,m}$ causes blurring in the x direction of the shifted images. In the final image, blurring is visible in the x (frequency encoding) direction and ghosts (shifted original images) are observed in the y (phase encoding) direction.

Phase encoding direction: the same periodic motion occurs in the y direction, and the additional artefactual terms are:

$$P(x,y) = C_0\{\delta(x-x_0)\delta(y-y_0)\} *_y \Big\{ \sum_{m=-\inf}^{\inf} \exp(im\phi_y)\delta(y-C_1 m) *_y (-1)^m F_{y,m}\Big\} \tag{2.4}$$

Motion effects are similar to the previous case, except that everything happens in y direction. The original image is convolved with $F_{y,m}$, which results in blurring in y direction, and shifted at positions $C_2 m$ in the y direction. Thus both blurring and ghosting occurs in the y (phase encoding) direction. An example of artefacts caused by respiratory motion in the phase encoding direction is illustrated in Fig.2.4(right).

These effects of periodic motion can be illustrated with a simple experience, Fig.2.3. The field-of-view contains a static cylindrical phantom and a small ball filled with Gd (the left-most static image). The ball undergoes periodic translation in the phase encoding direction (lower row) or frequency encoding direction (upper row). Images with different TR values are acquired during motion, resulting in different spacings between ghosts. The cylindrical phantom undergoes slight vibrations, creating similar artefacts.

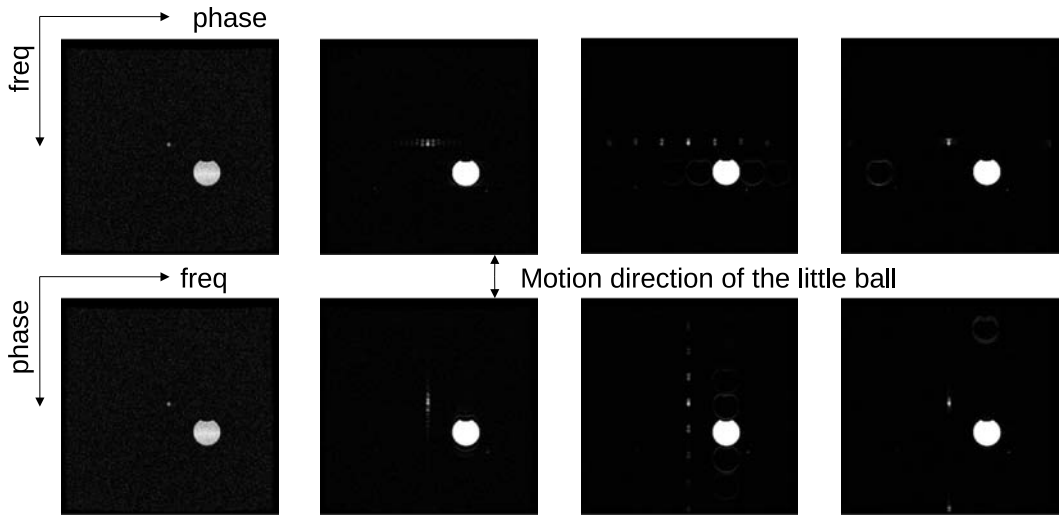

***Figure 2.3**: Point spread function induced by periodic motion: static image (left) and images obtained during the motion of the small ball in the phase encoding direction (lower row) and in the frequency encoding direction (upper row), acquired with different TRs, causing different ghost spacings*

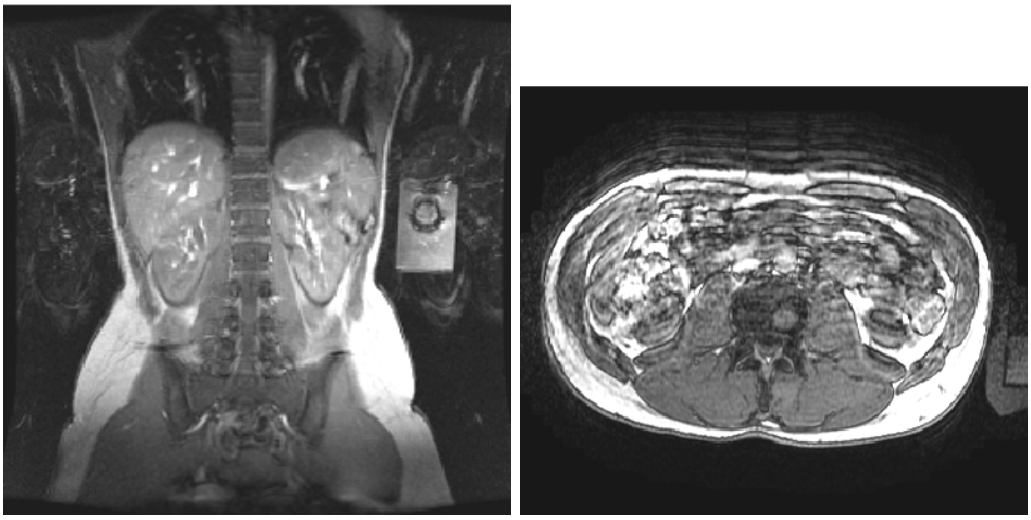

***Figure 2.4**: Real examples of artefacts caused by periodic motion between phase-encoding steps: respiratory motion of kidneys (left) and several abdominal organs (right)*

2.2.3 Motion between successive entire images (inter-image)

Many MRI applications require repeated acquisition of an entire image/field-of-view, and any motion occurring between these successive acquisitions might compromise, if not the image quality itself, then any post-processing taking into account all the dynamic images. In order to explore only the effects of this type of motion, the acquisition of an entire image is reckoned instantaneous, and motion occurring between subsequent images (inter-image motion) is of interest.

The simplest example is the averaging: the same field-of-view is imaged several times and then averaged, in order to diminish the influence of noise. Obviously, if motion occurs, different structures will be averaged instead of the same ones, and the resulting image may present slightly shifted superimposed initial images. Averaging is not always efficient, and most of all it requires longer acquisition time which is actually one of the main issues in MRI.

An important application of repeated acquisition is the before-after scheme: the first image is acquired when the imaged object is in its "normal" state, and the second after some modification is introduced. Usually this modification consists in injecting a contrast agent: the second image is acquired after the contrast agent has produced desired effects. For instance, delayed contrast-enhanced cardiac MRI consists in acquiring the second image approximately 10-15min after the injection, when the contrast has been mostly cleared from the myocardium. At that moment, only pathological ischemic myocardial tissue will still contain some amount of contrast agent and appear different (brighter) on the image. The purpose is to detect and eventually quantify ischemic tissue. If the analysis of these images

is only visual, motion between the first and the second image might not cause problems. However, as soon as a quantitative comparison of the images is to be performed, by subtraction for instance, issues arise. The two images have to be spatially transformed into the same position (registered) before undergoing any quantitative comparison.

Most affected by this type of motion are dynamic applications: the same field-of view is imaged repeatedly in order to track changes occurring in the FOV. These changes of interest are induced usually with a bolus injection of contrast agent (Dynamic contrast- or susceptibility- enhanced MRI). Contrast agents have different effects on tissue magnetisation, and they can be observed with different MR techniques (T_1 weighted, T_2^* weighted etc.). The ultimate purpose of these dynamic acquisitions is to provide contrast concentration vs. time curves, and extract quantitative diagnostic information from them. The interpretation of this technique is still mostly visual in the standard clinical practice, because of numerous difficulties and inaccuracies of the quantitative analysis. Motion is one of the main corrupting factors. If the intensity of magnitude images through time is to be processed, the same voxel has to represent the same structure in all time points. Motion introduces inaccuracies in these intensity-time curves, and thus in any parameter extracted from them. Therefore, the structures of interest have to be represented at each time point as being in the same physiological state. More on this in 3.3.5.

2.3 Methods for motion estimation and compensation

It is difficult to dissociate methods for motion estimation and compensation. Sometimes the same methods can be used for both motion estimation and compensation, such as image post-processing methods for image registration.

Methods for motion compensation have been developed for each stage in the process of MR imaging: data acquisition, image reconstruction and image post-processing. It is always better to correct errors as soon as possible in the processing pipeline: the more data are processed, the more errors propagate and add up. However, it is not possible to compensate for all motion-induced problems with one method, at least not in the current state of MRI.

Current methods belong to two different approaches, denoted as prospective (before and during data acquisition) and retrospective (after data acquisition). The issue of which approach is better, i.e. whether motion should be taken into account prior or after data acquisition, depends on specific applications, but the two approaches are rather complementary, and could be used simultaneously.

2.3.1 Imaging of physiological motion

Motion itself is not only a corrupting factor: it can also be of diagnostic interest. There are many techniques whose only aim is to observe motion, for it reflects physiological processes. Understanding and depicting the motion in the human body leads to better fundamental knowledge, and further to clinical applications: it is of great interest to be able to detect and analyse alterations of motion caused by pathologies; it is also very useful to be able to model and estimate the motion for compensating and interventional purposes.

Motion estimation has been studied with different imaging methods, ultrasound, fluoroscopy, CT, MRI etc. One of the advantages of MRI is the capacity to distinguish between different soft tissues, and so to study the motion of each one of them. Motion imaging with MRI is usually performed with acquisitions rapid enough to "freeze" the motion, followed by an image post-processing method for motion estimation between dynamic images (frames). Tagging can be added to this scheme: the organ (usually the heart) is "tagged" with a signal nulling grid, and then motion is estimated by post-processing grid deformations. Another important MRI technique for motion imaging is the (velocity-encoded) phase contrast MRI, which uses motion-induced changes of the image phase for extracting motion information, Jung et al. [44].

It is of great interest nowadays to be able to couple imaging with invasive procedures. Image-guided surgery and radiotherapy aim at achieving better precision during the invasive procedure, which implies also less negative effects for the patient. For instance, performing radiotherapy on abdominal tumours consists in radiating a wide area around the tumour, because it moves. If it were possible to estimate and predict tumour motion in a more accurate manner, the security area would be reduced, and healthy tissue around the tumour would be less irradiated, von Siebenthal et al. [95], Blackall et al. [8]. For doing this it is necessary to study thoroughly the motion of different organs, in healthy or pathological cases, in order to be able to measure, model and predict it more accurately.

2.3.2 Prospective motion compensation

Prospective methods aim at preventing motion-induced problems before and during data acquisition.

2.3.2.1 Breath holding

Unlike cardiac activity, breathing can be partially controlled: healthy subjects are capable of holding their breath for about 20s in average, while breath hold duration and quality are much lower and variable in patients. A simple and straightforward way of dealing with respiratory motion is to ask the patients to hold their breath during the acquisition of MR images. This method is rather

efficient when patients manage long and stable breath holds, but there are several issues:

- Acquisition duration is limited by the duration of the breath hold: compromises have to be made in terms of resolution, SNR etc.;
- Applications requiring several breath holds suffer from non-reproducibility and misregistration between images from different breath holds;
- The breath hold may not be perfect, or drifts can occur (illustrated in Fig.2.5);
- The breath hold has an influence on other organs: cardiac activity is not exactly the same in free-breathing and in breath hold: whether the heart should be imaged in free-breathing or breath hold remains an open question.

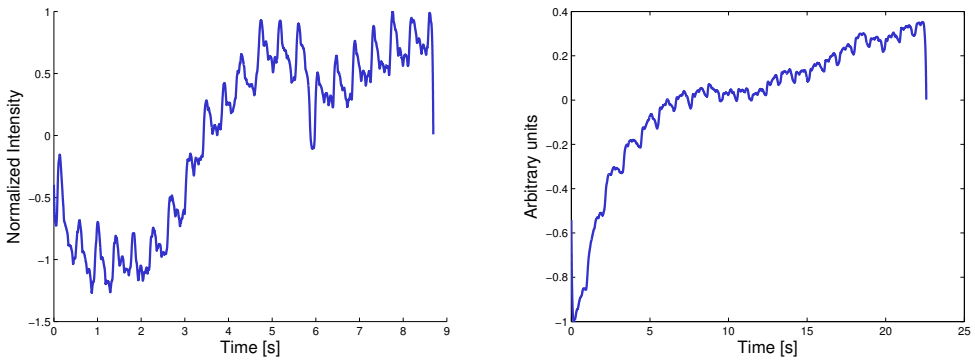

***Figure 2.5**: Examples of imperfect breath holds, as viewed by respiratory belts: badly sustained breath (left), drift behaviour (right)*

2.3.2.2 Prospective gating/triggering

Prospective gating consists in monitoring mainly physiological (respiratory and cardiac) motion in real-time, and choosing appropriate time intervals for data acquisition. Usually, the imaging is performed during the most quiescent interval in each period of pseudo-periodic physiological motion. Estimating the interval with least motion is not always obvious, because physiological motion is not a stationary random process in the general case.

Breathing A respiratory signal, see 4, is monitored in real-time and a threshold is set, in order to determine the breathing phase in which data should be acquired, as illustrated in Fig.2.6.

The preferred phase may be the interval around the expiratory or the inspiratory peak. The expiratory peak is often more stable and longer than the inspiratory

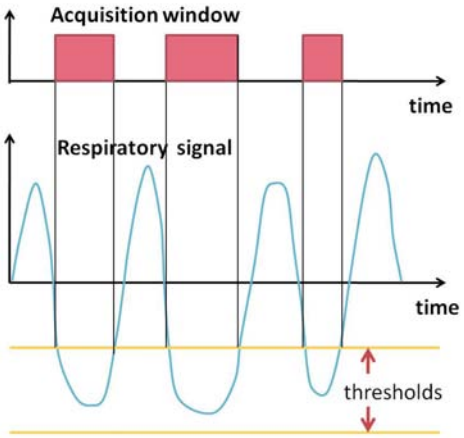

***Figure 2.6**: Thresholds are set for the respiratory signal, and data are acquired only in physiological positions between the thresholds (here intervals around expiratory peaks)*

peak, and also more reproducible. This method eludes the influence of respiratory motion on acquired images, but it lengthens the acquisition time considerably: a compromise has to be made between the elimination of motion and the acquisition time. On one hand, a narrow acquisition window during a precise respiratory phase in each breathing period provides thorough motion elimination, but very few data are acquired per period, so that many breathing cycles are needed for a complete image. On the other hand, large acquisition windows exploit time more efficiently, but allow for certain respiratory motion, which may generate artefacts.

Cardiac activity In order to synchronise MRI data acquisition with cardiac activity, the ECG signal, see Fig.4, is processed in real-time to detect R peaks. Since cardiac activity is rather swift, and the ECG is difficult to exploit in its entirety because of manifold corruption by MRI, a triggering approach is preferred to a gating approach. In each cardiac cycle, the acquisition is triggered a certain amount of time after each R peak, depending on whether the image should depict the heart in diastole or systole. Usually, the preferred cardiac phase is diastole, having a longer quiescent interval than systole in most standard healthy ECG signals. Depending on the pulse sequence and the heart rate, one, several phase encoded lines or the whole k-space matrix can be acquired between two R peaks.

2.3.2.3 Slice tracking

Slice tracking consists in modifying and adapting the pulse sequence in real-time with respect to the motion occurring in the field of view. Since MR pulse sequences contain many optimised details and depend on many parameters, they cannot be

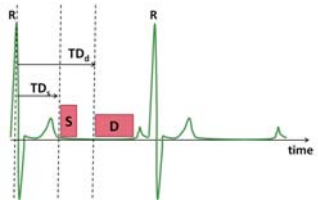

***Figure 2.7**: Each detection of the R peak in the ECG triggers data acquisition TD(delay time)ms after the peak, either in systole or diastole*

easily changed for motion compensating purposes without entailing other changes. Even though this approach cannot treat all motion-induced problems, it presents a unique way so far for dealing with out of field-of-view motion. It consists of two steps:

1. measuring motion in real time during data acquisition
2. deforming the field-of-view according to the measured motion, i.e. tracking the imaged object prior to acquiring each sample

The first step requires an accurate measurement of the motion of imaged organs, more on this in 4.

The second step is limited by MRI hardware properties. The gradient system is designed to be as linear as possible, so that the field-of-view can physically undergo only affine spatial transformations. It was shown that tracking the moving imaged object by applying affine transformations on the field-of-view is in accordance with the k-space formalism, Nehrke and Boernert [57]. Apart from certain subtle limitations, such as coupling with parallel imaging etc, this method has an important feature due to the affine model : the affine spatial transformation is applied to the whole field of view. This implies that movements of all the structures in the field-of view correspond to the same affine transformation.

Issues arise if motion is not really affine and if slice tracking is applied between different phase encoding lines: if some structures in the field-of-view move differently from the applied affine transformation or are static, the structures which move corresponding to the applied affine transformation will appear as static, whereas the others will appear as moving, and thus cause artefacts, as for inter-TR motion.

In brain imaging, a voluntary or involuntary movement of the head can be reasonably approximated as an affine transformation of the whole image, because the entire head moves in the same manner, on an empty background. On the contrary, in cardiac imaging, even when heart occupies the largest portion of the image, there is still some static non-empty background, as in the example Fig.2.8.

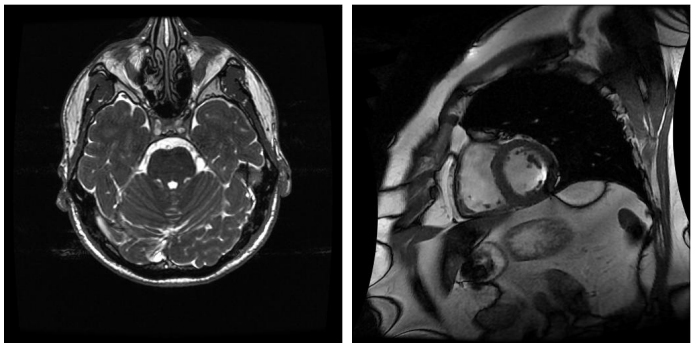

***Figure 2.8**: Affine motion modelling is more applicable to brain than to cardiac MRI*

2.3.3 Retrospective motion compensation

Retrospective motion compensation is very versatile: it consists in acquiring k-space data and motion information, and integrating motion compensation in the process of image reconstruction or image post-processing. Even though it is more flexible than prospective methods, it cannot really deal with severe out-of-FOV motion: if k-space data are acquired from the wrong part of the body, no retrospective method will be able to recover the structures of interest.

Image reconstruction occurs after data acquisition and before image post-processing, so it would be better to correct as many errors as possible in the reconstruction stage, instead of in image post-processing. Moreover, image post-processing deals most often with magnitude images and discards the phase. General (non-MRI) image processing methods usually deal with real images, generated with simpler underlying physical principles. Besides, MR image phase reflects mostly physical phenomena occurring during pulse sequence applications, and its use and exploitation is often not straightforward.

Both image reconstruction and post-processing tools are very powerful, but they have to be used very carefully, because they have a direct impact on medical interpretation: crucial features for clinicians' reading should never be jeopardised.

2.3.3.1 Image reconstruction

There are three different approaches for dealing with motion-induced problems via image reconstruction:

1. design of image reconstruction methods which require less samples than standard full k-space data, for the same image resolution and quality: data acquisition is faster and less motion sensitive

2. binning of acquired data into corresponding motion phases

3. integration of motion compensation into image reconstruction

The first group is very diverse and includes reconstruction methods in parallel imaging, 1.2.2, methods based on image compression (compressed sensing, Lustig et al. [52]), and reconstruction methods for radial acquisition patterns (less sensitive to motion because of more frequent sampling of k-space centre).

The second group is based on attributing each acquired data sample to a corresponding point in some motion-resolved domain. A theoretical approach to interpolation in a motion domain was exposed in Cindea et al. [19]. Binning data according to motion can be used for discarding data which were acquired during considerable motion, which is not very efficient, or for reconstructing separate images corresponding to different motion phases, Jhooti et al. [43]. For instance, the purpose of CINE cardiac MRI is to provide a dynamic high resolution depiction of a beating heart: data are acquired during as many cardiac cycles as the breath hold allows for, regardless of the cardiac phase. Then, in the reconstruction step, data samples are grouped according to their cardiac phase, and images corresponding to each cardiac phase of one cardiac cycle are reconstructed. This reconstruction reposes on the reproducibility of cardiac cycles.

The third group of methods is based on the idea of integrating motion compensation into image reconstruction. It started with first theoretical descriptions of motion effects, for simple cases of translational motion, Ehman and Felmlee [25], rotational motion Korin et al. [48], and periodic motion, Wood and Henkelman [100], Haacke and Patrick [34]. These first methods were based on measuring motion in some manner and subsequently applying corrections to the k-space data: phase correction for translational motion, and rotational regridding for rotational motion.

Methods with automatic extraction of motion information from image data are based on the optimisation of a criterion for image consistency. In Atkinson et al. [2], different rigid motion corrections are applied and the best one is chosen with an entropy-based image quality criterion. In Bydder et al. [16], parallel imaging is used not to accelerate the acquisition, but to provide additional information: inconsistent motion corrupted k-space data is detected, discarded, and regenerated with parallel imaging reconstruction methods.

In Batchelor et al. [5], a general framework for image reconstruction with integrated motion compensation was developed: a linear operator for any type of spatial transformation occurring in the field-of-view was integrated into generalised SENSE. This framework was augmented with motion estimation to yield pulsation-induced artefact correction for multi-shot diffusion brain images, Atkinson et al. [3], motion compensated reconstruction for liver in free-breathing (iDROPS), White et al. [97], and generalised motion compensated reconstruction with motion modelling (GRICS), Odille et al. [60], which was the starting point for these PhD studies.

2.3.3.2 Image post-processing: registration

Registration of each (source) image in an image series to a reference (target) image is a standard task for image post-processing. A variety of different methods exist: they are most often optimised for a certain application, i.e. a certain type of images. Images provided by different imaging techniques, such as photo or video cameras, CT, MRI, microscopy etc., have different inherent characteristics and thus often require slightly modified methods. Either the same method is applied and its parameters have to be optimised, or a completely different method has to be applied. Some of the most widespread approaches to registration are described in what follows.

The registration process consists either in trying out different spatial deformations and choosing the one which maximises some similarity criterion, or in directly minimising a cost function containing a similarity criterion and spatial deformation parameters. The spatial deformations can be rigid, affine, or non-rigid. They can also be modelled in different manners, using physiological motion models, or generic B-splines and free-form deformations. Similarity criteria differ according to their assumption on the relationship between the intensities of corresponding pixels in the target and source image.

Similarity criteria can be based on errors (difference between images, minimum least-square error, etc.), or on probabilistic quantities. Cross-correlation based criteria are often used in image registration. They assume that when the target and source images are registered, their intensities can be linked with a linear transformation. This is rarely the case with MR images, because the contrast depends on many parameters, even for the same MRI technique, and some techniques even imply contrast change in time, like dynamic contrast-enhanced MRI.

Information provided by a realisation of a random variable is higher if its value is more uncertain, i.e. if the probability density function of the variable is more uniform. Entropy is the expected value of the information quantity, so it provides a certain measure of average information and uncertainty of a random variable. Mutual information, or mutual entropy between two images to be registered represents information shared by both images. It should therefore be higher if the images are very similar, i.e. well registered. Many methods use different versions of mutual information maximisation in order to detect the best spatial transformation for image registration, either rigid or non rigid. Criteria based on mutual information have a different assumption regarding image intensities, compared to cross-correlation or error criteria. They assume a relationship between target and source image histograms: clusters in the source histogram correspond to clusters in the target histogram, even if their intensities are different. Consequently, these criteria are rather robust to contrast change, and are widely used in multi-

modality registration, Maes et al. [55], and MRI Rueckert et al. [79].

Optical flow represents the velocity or displacement vector of each image voxel as a function of time and space. Both quantities have components corresponding to each image dimension. It should be noted that, since images are available only at certain time points, regardless of the motion occurring in reality, observable displacements/velocities are apparent. Even if the imaged object has performed a complex movement between two images, only the sum of this movement will be observable. In order to determine a relationship between the optical flow and image intensity, it is assumed that image intensity does not change in time. The structures in the image move, but their characteristics (translated by image intensity) don't undergo any temporal changes. Hence, if the intensity of one fixed voxel in the image series is observed through time, any occurring changes are due only to motion. The total derivative of the image intensity I is given by the following equation:

$$\frac{dI}{dt} = \frac{\delta I}{\delta t} + \frac{\delta I}{\delta x}\frac{\delta x}{\delta t} + \frac{\delta I}{\delta y}\frac{\delta y}{\delta t} + \frac{\delta I}{\delta z}\frac{\delta z}{\delta t} \tag{2.5}$$

If the assumption described above, $\frac{dI}{dt} \approx 0$, is taken into account, and the notation shortened (image intensity x partial derivative $I_x = \frac{\delta I}{\delta x}$, and x velocity $u = \frac{\delta x}{\delta t} = u$), the equation becomes:

$$I_x u + I_y v + I_z w = -I_t \tag{2.6}$$

It should be noted that this equation alone is under-determined: the number of unknowns is equal to the number of image dimensions, hence always larger than 1. Therefore, additional constraints are needed to improve system conditioning. There is a variety of different methods which depart from this equation.

2.3.4 Standard methods used in clinical practice for motion compensation

Even though a large number of motion estimation or compensation methods have been developed until now, a very small portion of them is actually used in standard clinical practice: most of them still haven't achieved sufficient robustness, accuracy and implementation simplicity for widespread clinical use. It is useful to be aware of which methods are standard and implemented on most commercial machines.

Respiratory motion and its effects are reduced with breath holding, prospective gating (based on respiratory signals from respiratory pneumatic belts or a navigator echo placed on the diaphragm).

Cardiac activity is controlled with prospective triggering (based on ECG R peaks). CINE Cardiac MRI, based on ECG and breath hold, is used as a retrospective method.

2.4 Synopsis

While imaging a human subject, several types of motion can occur: voluntary or involuntary movements of the patient, and physiological motion (breathing, cardiac activity, peristalsis, etc.). The effect of motion on acquired MR data depends on the MR technique employed, acquisition time scale, and the characteristics (velocity, periodicity) of occurring motion. It can cause problems at several levels: during the preparation and acquisition of one echo (one basic pulse sequence-TR interval), between successive TR intervals (phase encoding steps), or between successive acquisitions of entire images. Methods for motion compensation have been developed with different purposes and effects for all stages of MR image generation : prospective methods applied before or during data acquisition (breath holding, prospective gating/triggering, slice tracking), and retrospective methods applied in image reconstruction (correction of k-space data, undersampled data, GRICS) or image post-processing (registration). In these studies, motion compensation was integrated into image reconstruction algorithms, and the application dealt mainly with respiratory motion between phase encoding steps and between subsequent dynamic images.

Chapter 3

Assessment of tissue perfusion with Dynamic Contrast-Enhanced MRI

3.1 DCE-MRI

MRI is an extremely versatile imaging modality: different imaging techniques have been developed for different medical applications. These methods can be assigned to numerous categories which differ strongly in their approach, and which can be further subdivided in numbers of slightly modified techniques. It is very difficult to provide a global view of all the methods because of their imposing quantity. Therefore, only the technique of interest for this research will be described: the *Dynamic Contrast-Enhanced Magnetic Resonance Imaging* or DCE-MRI.

Two main aspects of the human body can be observed with MRI: morphology, and function. Usually, morphological images are static, do not have a temporal aspect, and require high spatial resolution. Functional imaging techniques are designed to highlight some functional aspect of the body: physiological motion of an organ, blood circulation, perfusion by blood, tumour malignancy etc. Most of these characteristics are functions of time, and need to be observed during a certain period. Therefore, the imaging technique has to be dynamic: the same field of view is repeatedly imaged in time. Consequently, it implies a trade-off between spatial and temporal resolution, according to diagnostic priorities.

Often, functional aspects of the body are not directly visible by MRI, so that additional techniques are needed in order to highlight the characteristics of interest. A commonly used technique consists in injecting a *contrast agent* to the patient. Contrast agents are designed with the following main properties: their concentration has to be in a certain relationship with the observed functional characteristic and the MR signal. The most used contrast agents in MRI are Gadolinium (Gd) based. They are intra-vascular in the brain when the blood-brain barrier is intact, and they are intra-vascular extra-cellular in other organs and in tumours. Gd changes the magnetic properties of the surrounding tissue: the change is rather complex and

non-linear, for it depends on Gd concentration, the magnetic field, the tissue and its magnetic properties, pulse sequences, etc. Roughly, it tends to shorten the T_1, the T_2, and the T_2^*. Imaging is often optimised in order to use the contrast agent in its linear mode, i.e. when the effect on R_1 is proportional to the concentration of Gd in the tissue and the effect on T_2^* can be neglected, and vice versa. In that manner, image intensity is considered proportional to Gd concentration, and diagnostic information can be extracted directly from the image. Unfortunately, this is difficult to achieve, and the real concentration of Gd should be calculated based on image intensity and various other parameters.

3.2 Perfusion

One of the basic vital mechanisms of the human body consists in supplying the cells in nutrients via blood. Therefore, assessing different aspects of the perfusion of a tissue with blood is of great medical interest. There are many quantities that can be used to assess perfusion. The most usual one is the tissue blood flow, the volume of blood per unit of time and unit of tissue mass (or volume), the unit being usually ml/g/min.

The gold standard for perfusion assessment is nuclear medicine, mainly because of the variety, precision and high sensitivity of different existing tracers (called indicators, tracers or contrast agents, depending on the imaging technique). Its invasive nature, radiation and low spatial resolution are the main reasons for the considerable research being done with the aim of assessing perfusion with MRI.

3.2.1 Indicator-dilution theory

The general theory of tracer kinetics, called the *indicator-dilution theory*, was put into shape in Zierler [103]. This theory can be used for different physiological settings and different applications. There is a slight difference between applications to brain and other organs. The brain has a blood-brain barrier, which makes Gd-based contrast agents only intravascular. If this barrier is intact, indicator-dilution theory and Dynamic Susceptibility Contrast (DSC)-MRI is used for assessing brain perfusion. In the case of brain tumours, the barrier becomes permeable, and the target is to estimate permeability, with Dynamic Contrast Enhanced(DCE)-MRI. In the case of other organs (heart, kidneys, liver, breast, lungs), perfusion is usually assessed with DCE-MRI, though it depends entirely on the pathological physiology and approximations made towards prevalent permeability or blood flow.

Here, the general equation for a realistic bolus injection of contrast agent (non instantaneous, non constant arterial input function) will be described, and simplifications for separate permeability or blood flow estimation will be exposed.

Let's consider a piece of tissue, or a tissue voxel in the MR context. Let $C_t(t)$

be the concentration of the tracer in the tissue, and $C_a(t)$ the concentration of the tracer in the arteries supplying that tissue (usually called *Arterial Input Function-AIF*). Let $R(t)$ be the residue function, which represents the probability that the amount of the tracer arrived in the tissue at instant t_0 is still in the tissue at instant t, i.e. will remain in the tissue longer than t. Let F be a constant blood flow that characterises that tissue, in blood volume/time/tissue mass. Let E be the extraction fraction of the contrast agent from the capillaries to the tissue (the contrast agent contained in the blood does not flow into the tissue in its entirety). The general equation is the following:

$$C_t(t) = EF \int_0^\infty C_a(\tau)R(t-\tau)d\tau \tag{3.1}$$

The equation (3.1) suggests that the piece of tissue can be considered as a filter, with impulse response function $EFR(t)$:

$$C_t(t) = C_a(t) \otimes EFR(t) \tag{3.2}$$

Let's define the probability density function of tracer transit times through the tissue, $h(t)$. The residue function $R(t)$ being the probability that the tracer transit time is longer than t:

$$R(t) = \int_t^\infty h(\tau)d\tau = 1 - \int_0^t h(\tau)d\tau \tag{3.3}$$

Some characteristics of the residue function can be deduced intuitively: it has to be 1 at some starting time t_0, and decrease monotonously afterwards. The expectation of $h(t)$, called the Mean Transit Time (MTT), is defined as:

$$MTT = \int_0^\infty \tau h(\tau)d\tau = \int_0^\infty R(\tau)d\tau \tag{3.4}$$

These equations can be simplified by assumptions of constant/instantaneous arterial concentration, of only intravascular agents, etc., allowing for simple calculus of MTT and F with Central Volume Principle, but this corresponds to specific physiological settings, and is out of scope of this thesis, Zierler [103].

All the notions and tools described here are used for assessing directly or indirectly tissue perfusion, with the purpose of using it for medical decisions. It should be noted that the tissue probability density function $h(t)$ and the corresponding residue function $R(t)$ are unknown. The variables that are measured by imaging are the concentrations (in time) of the contrast agent in the tissue and the supplying arteries.

From the concentration vs time curves obtained with imaging, perfusion can be assessed to a certain extent in three different manners:

1. visually, by observing the behaviour of tracer concentration in time, in different parts of the tissue;

2. semi-quantitatively, by calculating some characteristics of concentration-time curves, which are only indirectly linked to perfusion, such as up-slope, time-to-peak, etc.;

3. quantitatively, by estimating tissue blood flow using the indicator-dilution theory;

Since the purpose of any quantitative measure in MRI is an eventual application of this measure for diagnosis and medical decisions, any measure that correlates with diagnosis and outcome is welcome. Therefore, some semi-quantitative measures or indices may be used, if they are significantly, although not directly, in relationship with some pathologies. Since the curve $C_t(t)$ is the most available measure, the peak of the curve, peak time, or the up-slope, can be used, Schwitter [82].

Quantitative methods use different versions of the indicator-dilution theory, with different simplifications and modelling. The perfusion can be assessed from these equations with two main groups of methods:

1. model-based methods, where the tissue is approximated by physiological pharmaco-kinetic models with a reduced number of physiological parameters;

2. deconvolution methods, where the general equation (3.1) is used, and deconvolution is performed in order to determine the impulse response of the tissue; modelling of the impulse response is used, but it does not relate directly to physiological parameters.

3.2.2 Methods with compartmental physiological modelling

Modelling of the tissue and its perfusion with blood can be performed on different levels, from the macroscopic point of view to the biochemical physiological processes. The aim of any model is to introduce some prior knowledge or some assumptions about the observed entity, and reduce the number of unknowns.

One of the most common pharmaco-kinetic models is the Tofts' model, Tofts et al. [89], called as such because Tofts performed a unification of numerous existing variants of 2-compartmental models and proposed a general nomenclature for the principal parameters involved. Compartmental analysis consists in dividing the vascularised tissue into different *lumped* compartments: each compartment is a homogeneous entity where any change happens instantaneously throughout the whole compartment. Obviously, adopting larger numbers of compartments leads to more realistic, but also more complex models, with more unknowns to solve for. Tofts' model consists of two compartments: arterial blood plasma, and the extra-vascular extra-cellular space of the tissue, as illustrated in Fig.3.1.

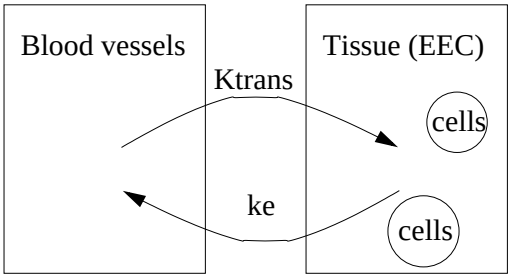

***Figure 3.1**: Illustration of a 2-compartment pharmaco-kinetic (Tofts) model: contrast agent exchange between arterial blood plasma compartment and the extra-vascular extra-cellular space in the tissue*

The parameters of the model are defined as follows:

1. K^{trans} is the transfer constant between the arterial blood plasma and the extra-vascular extra-cellular tissue space. It is defined as the product of the extraction fraction of the tracer from the blood pool E and the blood flow F, and further as a function of the arterial vessels permeability P and the exchange surface S:

$$K^{trans} = EF = F(1 - e^{-\frac{PS}{F}}) \tag{3.5}$$

   It can be seen that in the case when $F \ll PS$, when the vessel permeability is very high compared to the blood flow, $K^{trans} \approx PS$. On the contrary, when $F \gg PS$, the vessel permeability is low compared to the blood flow, and $K^{trans} \approx F$. Most of the pathological situations can be approximated with one of these two situations, which allows for simpler equations. In this setting, DCE-MRI can be used for estimating either permeability, or blood flow.

2. v_e is the volume of extra-vascular extra-cellular space per unit of tissue volume

3. k_e is the flux rate constant between the extra-vascular extra-cellular space and the arterial blood plasma

The general equation for the Tofts' model is obtained from (3.1) when the residue function $R(t)$ is modelled with

$$R(t) = e^{-t\frac{K^{trans}}{v_e}} \tag{3.6}$$

The general equation for Tofts' model becomes:

$$C_t(t) = K^{trans} \int_0^t C_a(t-\tau) e^{-\tau \frac{K^{trans}}{v_e}} d\tau \tag{3.7}$$

Only two parameters are unknown, K^{trans} and v_e, and they are usually solved for by fitting. It should be noted that the tissue blood flow is directly obtained only in the case of low vessel permeability, and the equation has to be adapted to the application, the organ of interest and its characteristic.

3.2.3 Deconvolution methods

Deconvolution methods remain at the level of the general indicator dilution theory, and use as prior knowledge only a rather loose general shape of the residue function, without introducing additional precise physiological modelling, as compartmental methods do.

The general equation (3.1) is solved for the product of extraction fraction and blood flow, using deconvolution methods. The tissue and the arterial concentrations are deconvolved in order to produce $EFR(t)$. The residue function $R(t)$ depicts the probability that all the contrast agent that entered the tissue is still in the tissue at time t. Since it represents tissue response to a Dirac impulse arterial input function, it should be a monotonically decreasing function, with the maximum at $t = 0$, equal to 1. This yields the estimate of EF for the impulse response $EFR(t)$ at $t = 0$, Jerosch-Herold [41]. Usually the extraction fraction is neglected and approximated by 1, which is reasonable for low vessel permeability. Again this depends on the application and the target organ.

Deconvolution is the same type of problem as image reconstruction: it is a one-dimensional ill-posed inverse problem, and is solved with the methods described in 1.1.2. The constraints consist in assumptions about the residue function: it is usually modelled with a one or more exponentials, or with B-splines, Pack et al. [66], Fermi functions, Jerosch-Herold et al. [42], etc., and different regularisations are used Sourbron et al. [87].

3.3 Assessment of perfusion using DCE-MRI

The previous description of methods for perfusion assessment is based on the assumption that blood and tissue concentrations of the contrast agent are directly measurable by an imaging method, here MRI. As described in what follows, there are many issues that have to be dealt with before concentration curves can be properly obtained from MR images.

3.3.1 Conversion of image intensity into contrast agent concentration

The usual approximation made in DCE-MRI consists in that the R_1 modified by the presence of the contrast agent is the sum of the initial R_1^0 and Gd concentration

weighted by a factor r_1:

$$R_1 = R_1^0 + r_1[Gd] \tag{3.8}$$

In that manner, subtraction of DCE-MRI image series with the pre-contrast image yields image magnitudes directly proportional to the concentration of Gd. This is true if r_1 is constant for the whole range of Gd concentrations in time, and if the regime is linear, which is never fully the case. Ideally, the signal equation should be used in order to calculate the exact concentration of Gd from the image. Unfortunately, the signal equation depends on many other parameters, which are not known and cannot be very easily and precisely measured. This can be approximately done by simplifying slightly the signal equation, measuring unknown equation parameters (usually the T_1 before contrast injection, and B_1 inhomogeneity), and then extracting the Gd concentration.

After the conversion of image intensity into Gd concentration, concentration-time curves can be extracted either pixel by pixel, or by averaging pixels in regions of interest, in order to minimise the influence of noise. In practice, it is very difficult to perform a proper conversion from image intensities to Gd concentration, and it is rather the intensity-time curves, subtracted by the baseline, which are considered.

3.3.2 Voxel issues

It is usually assumed that the intensity of one voxel, depicting the organ of interest, reflects only the extra-vascular tissue of the organ. Since the spatial resolution in clinical MRI is larger than 1 pixel/mm, the tissue is observed on a rather macroscopic level and there is certainly a vascular component in the voxel. Another standard problem related to large voxel size is the issue of partial volume: the voxel contains rarely completely homogeneous tissue. The correction for the actual volume of relevant tissue in the voxel can be introduced in the modelling.

3.3.3 Arterial input function

Measuring contrast agent concentration in the arterial blood which supplies the observed organ/tissue is not an easy task.

Firstly, it is assumed that the contrast agent is homogeneously distributed in the blood. However, the contrast agent is extra-cellular and so contained only in the blood plasma. In order to compensate for this phenomenon, K^{trans} for instance can be corrected by multiplying it with $\rho(1 - H_{ct})$, where ρ is the density of the tissue and H_{ct} is the blood hematocrit, i.e. the concentration of red blood cells in blood plasma.

Secondly, in the general case, the closer the arteries are to the tissue, the smaller they are: their size reduces gradually from aorta to capillaries. It is preferable and more accurate to measure arterial concentration of Gd as close to the tissue as possible, which usually implies very small vessels. Unfortunately, when imaging

arteries with MRI, especially if they are small, issues arise: MR signal may suffer from blood flow, vessel motion, partial volume, contrast agent saturation etc. Optimised techniques for vessel imaging do exist (MR angiography), but they are not easily coupled with DCE-MRI. The arterial input function can be sampled in larger arteries or the aorta, but then the delay between the measured AIF and the real one (close to the organ of interest) has to be taken into account in post-processing.

Usually, for perfusion studies, the contrast agent is injected with a bolus, for instance $0.05 - 0.1 mMol/kg$, at an injection rate of several ml/s. This produces a strong rapid uptake in arteries, followed by a slower decrease. In order to acquire this arterial input function properly, the pulse sequence has to allow for a large dynamic range of T_1 changes, and to be immune to the T_2^* effect. A common problem results from an apparition of T_2^* effect in the pulse sequence when T_1 is very short, i.e. at the peak of the bolus. This can cause saturation in the arterial input function: the peak is cut and smoothed. Obviously this causes considerable inaccuracies in post-processing and blood flow estimation. Therefore, attention has to be paid to the signal equation of the pulse sequence and the Gd concentration, quantity and injection rate. A trade-off is usually made between diminishing the saturation effect and increasing contrast-to-noise. An example of ideal arterial input function is illustrated in Fig.3.2.

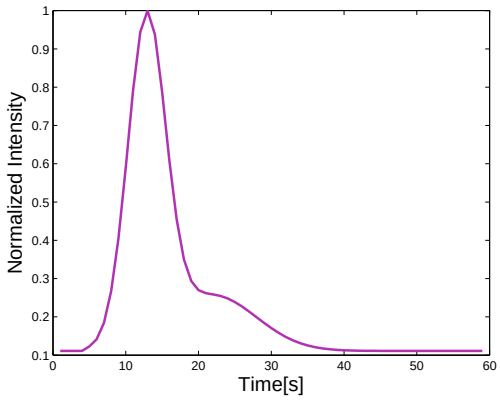

Figure 3.2: *Example of an ideal Arterial Input Function*

3.3.4 Pathological vs Healthy subjects

One of the omnipresent issues in MRI is the fact that usually, pulse sequences, reconstruction and post-processing methods, are first optimised in the context of healthy subjects. For instance, compartmental modelling often fails in severe pathological cases because it does not take into account all the pathological factors.

Therefore, when designing a method, it is extremely important to keep in mind the clinical application and to consider pathological influences.

3.3.5 Motion

Since intensity-time curves are extracted from a dynamic series of image magnitudes, it is obvious that at each time point the same voxel or object has to be observed. Ideally, voxel intensity-time curves would be of interest, thus exploiting maximally the spatial resolution. However, since MR images are always corrupted by a certain amount of noise, regions of interest are usually preferred to individual voxels, because averaging of voxel intensities in the region slightly lowers noise level. A compromise has to be made between the desired spatial resolution for intensity-time curves, and the signal-to-noise ratio (SNR).

In practice, a region of interest (ROI) is selected manually by a radiologist, on one image in the temporal series. Then, the mean intensity is calculated for this same region of interest in each image in the series. If the structures in the region of interest are static, i.e. exhibit no motion through the temporal image series, the resulting intensity-time curves are consistent. However, if the structures move, issues arise. Intra-image (inter-TR) motion will result in blurring and ghost artefacts, which will compromise spatial resolution and corrupt image intensity. Inter-image motion will cause the structures of interest to move in and out of the region of interest, so that intensity-time curves from that region will not reflect accurately the structures of interest. An example of motion corrupted intensity-time curves is given in Fig.3.3.

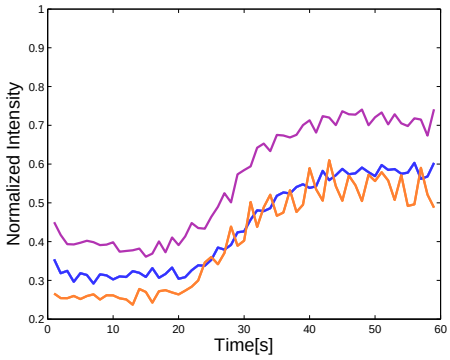

***Figure 3.3**: Noisy, motion-corrupted tissue intensity-time curves extracted from myocardial segments*

The solution to inter-image motion (misregistration) consists either in drawing the ROI including the structures of interest on each temporal image, or in registering all the images with respect to one image in the series.

If these solutions are implemented manually, they may suffer from several issues:

- very time-consuming, thus not easily applicable in clinical practice
- operator intra-variability: when an operator performs twice the same task, the second result is not exactly the same as the first one
- operator inter-variability: different operators perform the same task in a different manner, even if some guideline criteria are fixed

Automatic implementation is meant to solve these issues. However, MR images are a difficult task for image post-processing techniques, and automatic segmentation and registration are rather difficult to implement in an accurate, robust and computationally efficient manner. The performance of these automatic methods depends strongly on the application: DCE-MRI is a very challenging one, because of the contrast change in time. Most registration methods use constraints and similarity measures which assume that the temporal change in structures of interest is due only to motion and nothing else, so that the unknowns in equations represent only displacement, see 2.3.3.2. Contrast change adds a second unknown, which has to be either eliminated in some manner, or taken into account in the equations and solved for.

3.4 Applications

3.4.1 Myocardial perfusion

Coronary arteries supply the myocardium, or the heart muscle, with blood. A good function of the myocardium depends on its blood supply, so that any defect in the perfusion of the myocardial tissue points to a pathology. DCE-MRI is performed both in rest (normal conditions), and stress (injection of a product, or physical activity before or during the MR acquisition, in order to stimulate and accelerate cardiac activity and thus highlight perfusion defects). An example of myocardial perfusion in rest is presented in Fig.3.4.

The features of DCE-MRI designed for myocardial perfusion assessment, Jerosch-Herold [41], are the following:

- cardiac gating, either in systole or diastole
- breath holding as long as possible, at least during first pass, later free-breathing
- temporal sampling with a period of 1 or 2 RR intervals for rest, and 1 RR interval for stress
- several slices in short axes, preferably 3D

- appropriate T_1 weighting, with magnetisation preparation (saturation recovery) and short TE
- total duration of 1min or more
- spatial resolution of less than 1 pixel/2.5 mm

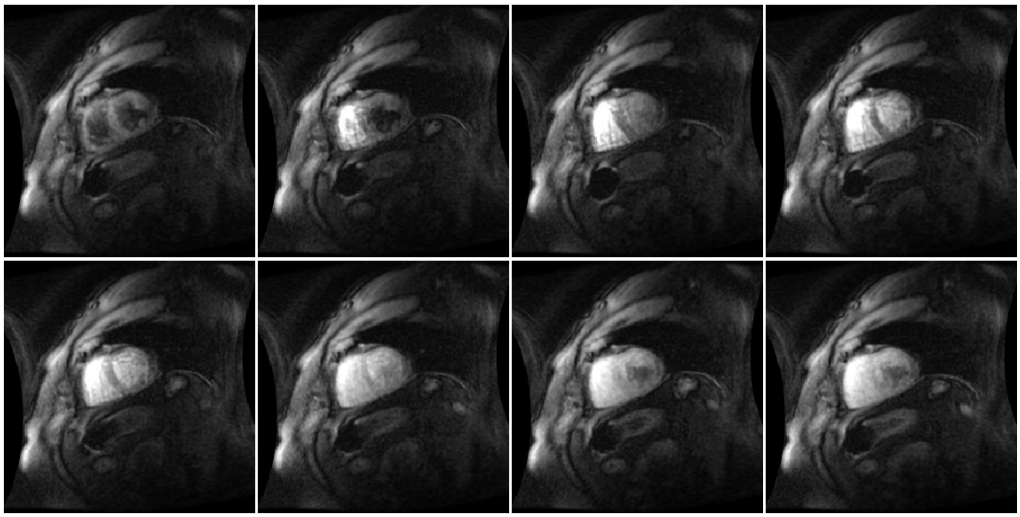

***Figure 3.4**: Myocardial perfusion DCE-MRI: several images from the dynamic series, at important moments of the passage of the Gd contrast agent: pre-contrast image, enhancement of the right ventricle blood pool, enhancement of the left ventricle blood pool, enhancement of the myocardium, and progressive washout.*

Different post-processing methods have been tested for assessing myocardial perfusion from DCE-MRI: visual analysis, Schwitter et al. [83], semi-quantitative methods, different multi-compartmental models, Ichihara et al. [37], deconvolution methods, Pack et al. [66], Jerosch-Herold et al. [42]. The arterial input function is often estimated from the left ventricle blood pool, but suffers from saturation effects. Therefore, a dual-bolus technique can be used, Christian et al. [18]: prior to the actual perfusion imaging, a lower dose of contrast agent is injected, and imaging is performed with the sole purpose of measuring the arterial input function free of the saturation effect.

Motion compensation has been investigated in terms of prospective slice tracking based on a diaphragm navigator, Pedersen et al. [68], and image registration in post-processing: translational rigid registration with a similarity criterion based on normalised mutual information, Wong et al. [99], translation correction using Independent Component Analysis for dealing with contrast change, Milles et al. [56], non rigid registration based on quasi-periodicity of respiratory motion, Wollny et al. [98].

3.4.2 Renal perfusion

Kidneys are a very particular organ from the vascular point of view, because their main function is to filter blood. Their physiology is complicated and difficult to model. Assessing perfusion in kidneys is linked with assessing the renal function, either in native or transplanted kidneys. The acquisition is preferably in 3D and breath hold is usually not feasible due to a long acquisition time. The arterial input function is usually extracted from the aorta, and renal intensity-time curves can be extracted either pixel by pixel, or from ROIs positioned in the parenchyma (cortex and medulla). An example of dynamic images at important moments of the passage of Gd contrast agent is presented in Fig.3.5.

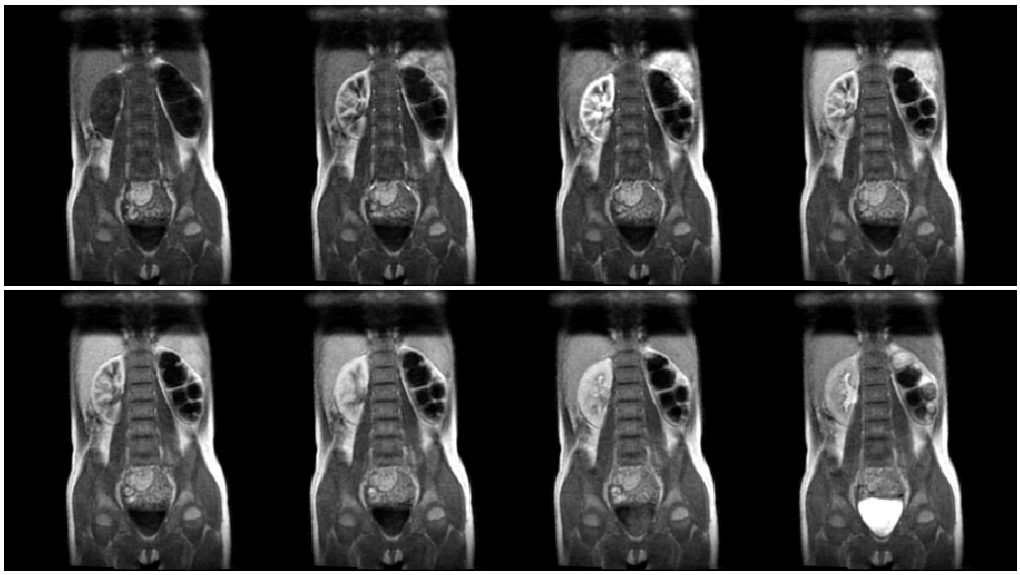

***Figure 3.5**: Renal perfusion DCE-MRI: several images from the dynamic image series, at important moments of the passage of Gd contrast agent: pre-contrast image, enhancement of the parenchyma, enhancement of the medulla, and progressive washout to the renal pelvis, and the bladder.*

Typical intensity-time curves extracted from renal perfusion MRI is shown in Fig.3.6. They suffer from respiratory motion: kidneys move mainly due to breathing, mostly in a slanted superior-inferior plane. 2-compartmental models have been used, Bokacheva et al. [10], but are rather limited because they do not take into account the interstitial space, which becomes important in pathology. Efforts are made to solve the issue of calculating [Gd] concentration from MR image magnitude, Bokacheva et al. [9].

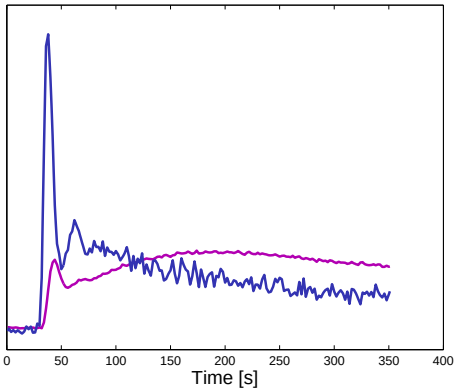

***Figure 3.6**: Example of intensity-time curves from renal perfusion DCE-MRI (MR renography): arterial input function from the aorta (pink) and tissue (renal parenchyma) intensity-time curve (blue)*

3.4.3 Other applications

Tumours in different organs, from brain to abdomen, can be assessed by DCE-MRI. Usually the temporal resolution is sacrificed in view of the spatial resolution. 2-compartmental models are widely used for this application.

Part II

Adaptive Image Reconstruction

Chapter 4

Physiological Signals

In order to develop a method for motion compensation, it is necessary to have an estimate of the motion occurring in the field-of-view during data acquisition. With a few exceptions, most methods rely on information provided by some sort of motion sensors. Therefore, it is of interest to develop sensors for different types of motion. It is also crucial to develop methods for extracting and using relevant information from motion sensors. This chapter deals with existing, standard and less standard motion sensors, with new sensors developed in the IADI lab, and with methods for processing sensor signals, which were explored during these studies.

Physiological motion occurs inside the human body. It is therefore preferable to measure the motion with internal sensors, in view of better accuracy and reliability. However, internal often implies invasive, and any sensor for human or animal subjects has to be the least invasive possible. Two strategies have been adopted for measuring physiological motion in the MRI environment: internal sensors based on MRI itself, since one of the main advantages of MRI is its non invasive nature, and external sensors, which in addition have to be designed so as to be MR compatible.

4.1 Internal sensors: Navigator echoes

Navigator echoes are sensors implemented with MRI techniques, Bernstein et al. [6]. Therefore, they are both internal and non-invasive. The only drawback of using MRI-based methods for motion sensing during MR imaging, is that interactions can occur between sensors and imaging itself. Hence, the development of internal MRI-based sensors strives at limiting these possible interactions and avoiding additional acquisition time.

Navigators can be positioned either in the imaged field-of-view, or outside of it. The first option requires careful pulse sequence programming, in order to minimise interactions between navigators and image data, but detects directly motion and changes occurring in the imaged field-of-view, which can be used for prospective or

retrospective motion correction. The second option doesn't suffer from interactions between the navigator and image acquisition, but it measures motion only indirectly.

4.1.1 Navigator types

1D navigator echoes can be implemented by imaging a 1D field-of-view, or by acquiring a specific, usually central, k-space line in some 2D or 3D field-of-view. In terms of motion, they can detect translational motion occurring in the direction of the acquired line, by observing the changes in the phase of the navigator image.

2D navigator echoes can detect both translation and rotation in the plane of the navigator field-of-view. Their acquisition pattern in k-space can be a spiral, a Cartesian EPI read-out, or a circle (orbital navigators). The radius of orbital navigators is a compromise between SNR and sensitivity to rotation.

3D navigators represent a sphere in k-space, and can detect translation and rotation in any direction.

4.1.2 Diaphragm monitoring

Navigators positioned outside of the imaging field-of-view are usually implemented for respiratory motion compensation. A 1D, or 2D rectangular navigator is placed in a small field-of-view on the diaphragm, in the superior-inferior direction: it depicts clearly the interface between the liver and lungs. Examples of field-of-views are shown in Fig.4.1. This allows for respiratory signal extraction, and estimation of the respiratory motion in the imaging field-of-view, for instance in the case of abdominal or ECG-gated cardiac imaging. Following this, respiratory motion can be compensated, either in real-time with prospective gating or slice tracking, or retrospectively during image reconstruction.

4.1.3 Central k-space line

Usually the central k-space line (line in frequency encoding direction, with zero phase encoding) is acquired only once per one k-space coverage, full or undersampled. By changing the pulse sequence, the central line can be acquired much more often, before or after each echo train or k-space line. The information contained in the central line is thus available at each acquisition time point of interest. If the image is static and doesn't change in any way during acquisition, the central line will always be the same. However, if some changes occur, the central line will reflect them to some extent.

The central point of k-space has the highest amplitude because it contains the mean value of an image with positive intensities. The whole central line has an additional interest: if reconstructed to image domain ($s(x)$ in (4.2)), it is equal to the initial image averaged in the phase encoding direction. In other words, it

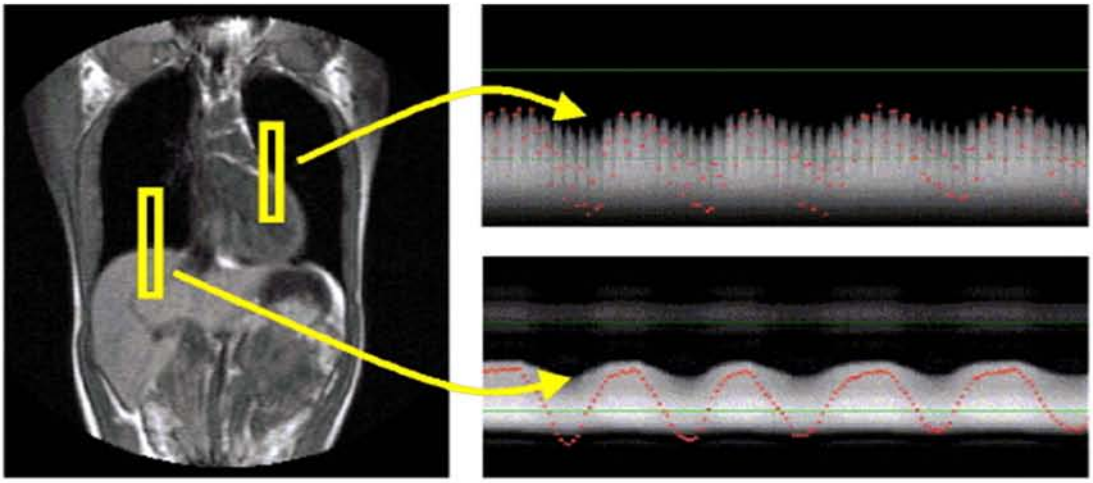

***Figure 4.1**: Examples of field-of-view placement for respiratory motion navigators, on the diaphragm and the heart, (left) and obtained physiological signals (right). Extracted from Nehrke et al. [58]*

represents the circular convolution of the whole image with a line perpendicular to the central line (x=0).

$$S(k_x, k_y = 0) = \int_{-\infty}^{\infty} \exp(-j2\pi x k_x)\Big(\int_{-\infty}^{\infty} \rho(x, y)dy\Big)dx \tag{4.1}$$

$$s(x) = \int_{-\infty}^{\infty} \rho(x, y)dy \tag{4.2}$$

For instance, if considerable contrast change appears in the image, the central point or the central line will also change. However, it is a very approximate sensor of contrast change, because contrast changes usually occur locally, in very precise regions, and the averaged values provided by central points are a global measure.

If the frequency direction is parallel to some notable translational motion, such as the respiratory motion of the heart or diaphragm, the reconstructed central line will depict well the interface between moving objects and thus their translational motion. If many central lines are acquired during motion, and represented in spatio-temporal domain, intensity changing patterns will depict the underlying motion, as illustrated in Fig.4.2 (example from Odille et al. [62]). In parallel imaging, the central k-space line is received by different coils: depending on the structures highlighted by the spatial sensitivities of the coils, different types of motion may be detected in the central line signal of each coil.

This central line phenomenon and its variants have been exploited for detection of respiratory and cardiac motion and subsequent prospective or retrospective gating. Prospectively self-gated imaging was developed for abdominal imaging

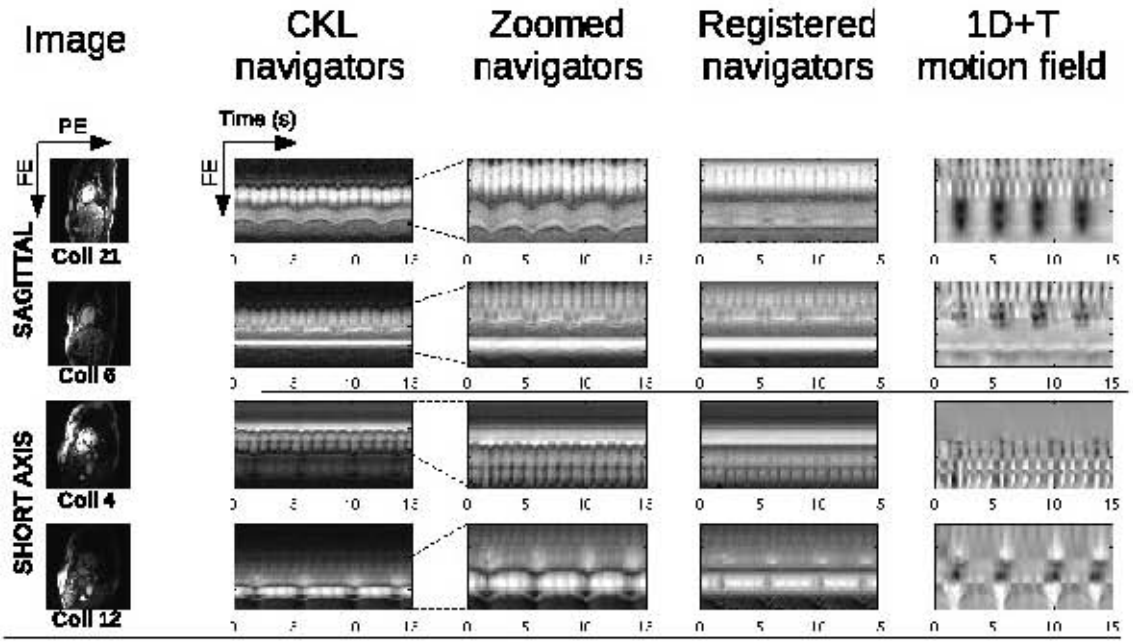

***Figure 4.2**: Source image (left), with x being the frequency encoding direction, and reconstructed central k-space line vs time (right), presenting oscillations caused by translational motion in the x direction. Extracted from Odille et al. [62]*

dealing with breathing and pulsating motion of arteries, Brau and Brittain [11], and for cardiac imaging with breathing and cardiac motion Buehrer et al. [15]. Retrospective self-gating has been developed mainly for cardiac cine imaging, either in breath hold with cardiac gating, Larson et al. [51], Crowe et al. [20], or in free-breathing with both cardiac and respiratory gating Odille et al. [62].

4.2 External sensors

External sensors have the advantage of being non invasive by default. Their main drawback is the distance between moving imaged objects and the point of measure. Developing new sensors is rather tricky: in order to define what should be measured with the new sensor, physiological motion and its effects have to be studied and well known. For instance, if motion is measured on the body surface, the relation between the external manifestation of motion and the internal motion itself should be well established. There is still place for research in this area. Most difficulties stem from the fact that physiological motion is extremely intra- and inter- subject dependent.

4.2.1 Pneumatic belt

Respiratory pneumatic belt, or respiratory bellows, is a standard device designed for measuring external respiratory motion in MRI. Depending on the manufacturer, the device consists of a long expendable pneumatic tube, or a smaller bellows pillow, secured around subject's abdomen or thorax. Respiratory expansion and compression of the abdomen/thorax causes extension and tightening of the bellows, which manifest as pressure changes. These pressure changes are registered and transferred via an optic signal to the MRI scanner or to the exterior of the MRI room. The very few electronic elements required make it highly adapted to the MRI environment.

Expansion of the abdomen/thorax reflects breathing quite well and can be easily detected. However, abdomen/thorax volume change is a very global measure of breathing: it presents a sum, or integration, of many different movements, because the motion of the abdominal surface is spatially variable. The most dominant is the anterior-posterior motion of the anterior abdominal wall, whereas the sides of the abdomen move less. Such externally detectable breathing is influenced by the corpulence of the subject: the internal motion can be slightly absorbed by the fat. As for pneumatic belts, they can slightly sink in the flesh in corpulent subjects, or adhere poorly to very slim subjects and change position easily. This introduces bias in the final signal.

An interesting feature is that, during breath hold, an ECG-like component can be seen in the signal from respiratory belts, Fig.4.3. However, it hasn't been explored much, because it is not always visible, and has to be extracted from breathing signals by filtering.

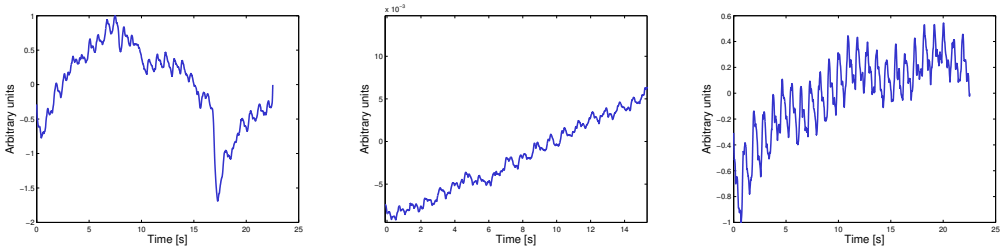

***Figure 4.3**: Motion from cardiac activity can be seen in signals from respiratory belts during breath hold*

The pneumatic belt is sensitive to different breathing patterns: ample, slow and deep breathing, normal breathing, unequal inspiration and expiration velocities, etc, Fig.4.4.

The purpose of signals obtained with respiratory belts on commercial scanners is either respiratory synchronisation, described in 2.3.2.2, or breath hold monitoring. Therefore, the shear raw signal from the respiratory belt is often inaccessible:

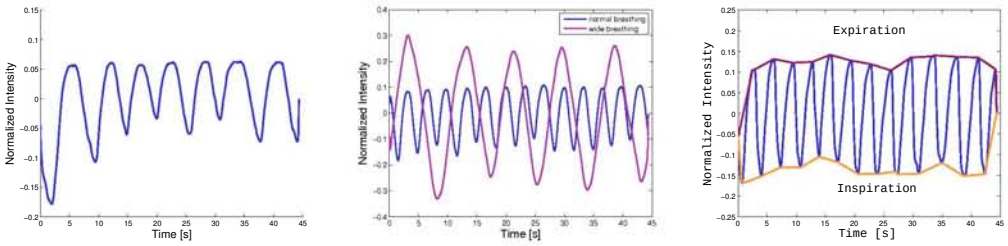

***Figure 4.4**: Breathing patterns (from left to right): free normal breathing, ample(pink) versus normal (blue), and breathing with swift inspiration and slower expiration*

it is always filtered and processed, in order to yield a smooth signal for robust synchronisation.

4.2.2 Accelerometer

There exist several devices for measuring acceleration, either electronic or optical. They are interesting for application in MRI because they measure a very localised movement and can be very small. However, their adaptation to the MRI environment is not straightforward: power supply is not an easy issue in MRI, and electronic parts may suffer from electromagnetic fields. The idea is to be able to measure the motion of a small fraction of the body surface, affected by some internal motion. Pulsating motion of important arteries can be partly visible on the surface, as well as swallowing movements, and respiratory motion can be sensed in different regions. It could also be used for sensing involuntary motion of the head.

Since respiratory motion affects many organs, its effect on the surface reflects a sum of different processes. The advantage of measuring respiratory motion on a small localised surface stems from the fact that different parts of the abdominal/thoracic surface move in a different manner, and might reflect different internal movements. The main disadvantage is that the skin is an elastic non flat surface, with a more or less thick subcutaneous layer of fat: therefore, small local movements, especially in more corpulent subjects, don't reflect only internal motion, but also some elastic characteristics of the surface layer. Accelerometer measures acceleration in one or more axes: since it moves in the same manner as the observed moving object, the skin surface on which the accelerometer is attached has to move so that the axes of the accelerometer remains the same, for the measure to be correct, which is not easy to implement on the surface of the human body. At the current state of development, the accelerometer device creates slight artifacts in images.

Accelerometer sensors are being developed in the Laboratory IADI: they have been presented at the ISMRM conferences, the initial analogue version Rousselet

et al. [77], and a digital version Rousselet et al. [78]. A few examples are presented in Fig.4.5.

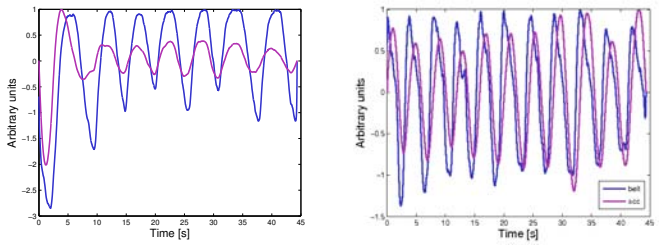

***Figure 4.5**: Signal obtained from the accelerometer-based sensor (pink) versus the signal from a respiratory belt (blue)*

4.2.3 Optical devices

Optical motion tracking is a well explored field, but its application in MRI is hampered by many issues. Cameras and motion detection algorithms for photographic images are well developed. However, a standard camera cannot be easily used inside the MRI tunnel, and encounters visibility and field-of-view problems when positioned outside of the tunnel. Besides, motion detection algorithms need certain motion markers: it is difficult to detect motion from uniformly coloured moving surface without any convenient background interfaces or marks. Several solutions have been proposed, both for optical imaging and motion markers, Zaitsev et al. [102], Ooi et al. [63], Qin et al. [73].

4.2.4 ECG

The ECG in MRI is slightly different from the standard ECG, because it had to be adapted to the MRI environment, Felblinger et al. [27]. For instance, wires have to be very short, so that all the electrodes are placed near the heart, the derivation is different, the output signal is converted to an optical signal, etc..

Since the main purpose of ECG in MRI is cardiac synchronisation, the feature of interest in the ECG signal is the R peak. Usually, the R peak is detected and the pulse sequence is triggered a certain amount of time afterwards, either for imaging the following cardiac cycle, or for preparing the imaging of the next cycle, as described in 2.3.2.2. Therefore, it is crucial to implement a robust and accurate R peak detection from the ECG signal, even by neglecting other features. Hence, shear ECG signal is often inaccessible on commercial scanners, because it is optimised and filtered for a robust R peak detection. The Vectocardiogramm is often used instead of the ECG for peak detection.

Beside R peak detection, the ECG signal can be used for more sophisticated purposes, such as RR interval prediction, adaptive gating, and detection of different cardiac phases for retrospective or prospective motion correction. These applications require filtering, for denoising and artifacts correction. The main artifacts are caused by the B_0 magnetic field (Hall effect on the flowing blood), which deforms the T wave in the ECG signal, Jehenson et al. [40], Chakeres et al. [17], and by B_0 gradient switching and radio-frequency pulses. Some examples of ECG signals, obtained during MRI pulse sequence play-out and thus corrupted by noise and artifacts, are illustrated in Fig.4.6. Denoising and correction of gradient-induced artifacts were proposed in Oster et al. [65], Oster et al. [64]. RR interval prediction was used in Fernandez et al. [28] for systolic black blood fast spin echo cardiac imaging.

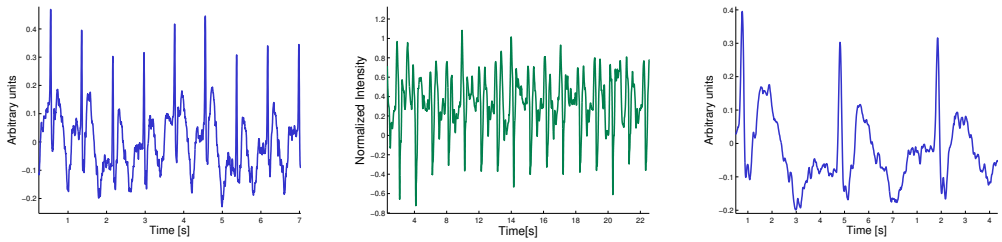

***Figure 4.6**: Examples of ECG corrupted by noise and artifacts in the MRI environment*

It has been noticed that the R peak amplitude is modulated by respiration, Felblinger and Boesch [26]. If a signal is formed from R peak amplitudes, it resembles strongly a respiratory signal, as illustrated in Fig.4.7. Its temporal resolution is equal to 1/(cardiac cycle), which is not sufficient for a respiratory signal, but it still yields physiological positions at certain moments. Interpolation can be used to increase the temporal resolution, but it can also lead to errors.

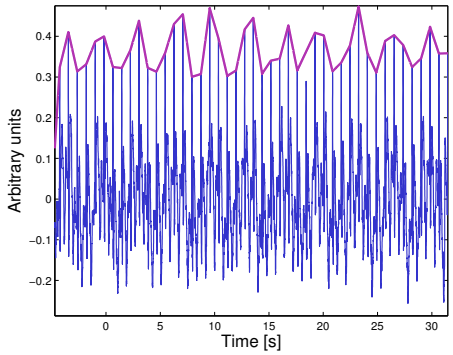

***Figure 4.7**: Modulation of R peak amplitudes with breathing, drawn in pink*

R peak detection, as implemented on commercial scanners, is an efficient method, and works well when the heartbeat is stable and the acquisition occurs during a quiescent period in cardiac activity. Obviously, this synchronisation lengthens the acquisition, though not only for eliminating cardiac motion: it can also be of medical interest to observe the heart only in a particular phase of its activity. Problems occur in subjects with a high variability of RR intervals, or with a pathological cardiac activity: the quiescent period (systolic or diastolic) doesn't occur at the precise time estimated by the pulse sequence.

4.3 Signal Analyser and Event controller (SAEC)

Since it is difficult to access and process external physiological signals on commercial scanners, it is not easy to use them for developing new methods for motion correction. Therefore, a customised device, SAEC (Signal Analyser and Event Controller), has been developed in the laboratory IADI, Odille et al. [59]. It is designed for receiving raw physiological signals from external sensors, as well as signals depicting pulse sequence timing (acquisition window, gradient switching, RF pulse play-out etc.). The system also provides a platform for signal post- or real-time processing, as well as a feedback to the MRI scanner for pulse sequence controlling. Each type of motion compensation techniques can be implemented with such a system. Raw physiological signals can be processed in real-time and sent as a feedback to the MRI scanner, by performing:

- ECG denoising/artifacts correction and subsequent ECG gating Oster et al. [65]
- RR interval prediction and adaptive ECG gating, Fernandez et al. [28]
- prospective motion correction based on filtered ECG and respiratory signals

Raw physiological signals can also be processed off line and fed into adapted reconstruction techniques with motion compensation, Odille et al. [61], which was used during these studies.

4.4 Comparison of different physiological signals

In the general case, physiological motion is spatially and temporally variable, elastic, and non rigid: hence, it is not simple to measure and describe. Therefore, and in view of advanced motion compensating methods, it is often not sufficient to have only one raw physiological signal. Firstly, it is preferable to have more than one physiological signal, and secondly, relevant information contained in these

signals has to be properly extracted. However, different signals are often strongly correlated, especially those available today, and provide similar information.

As mentioned in 4.2.2, accelerometer-based sensors have been developed in the Laboratory IADI by Laure Rousselet within her doctoral studies, after an initial work on this subject done by Cédric Pasquier for his doctoral thesis. The first analogue version was tested on phantoms with simple motion and then on volunteers, Rousselet et al. [77]. The first application for this sensor consisted in measuring respiratory motion. Therefore, tests on volunteers and comparison with reference methods were carried out within a research trial implemented by Laure Rousselet. The signal processing part of this research trial was assigned to the author of this thesis, and it is described in what follows. The purpose was to process different physiological signals, and to implement a method for their comparison. Analysing the differences between different signals, especially between internal and external motion, was also of interest. Another purpose kept in mind was the use of accelerometers for motion compensating image reconstruction methods explored during these studies (GRICS), namely for the GRICS motion model, see 5.1.1.

4.4.0.1 Research protocol

Signals from accelerometers were recorded synchronously with signals from two pneumatic respiratory belts (abdominal and thoracic) and an ECG. Volunteers were asked to breathe in different manners: normal breathing, deep breathing, rapid inspiration/slow expiration, and rapid expiration/slow inspiration. These instructions were followed in most cases, except for rapid inspiration/expiration scheme, which volunteers often didn't manage to perform correctly. Rapid balanced SSFP images were acquired at the same time, with a temporal resolution of around 1/200ms. A sagittal slice passing through the lungs and the right liver hemisphere (and diaphragm) was chosen as the field-of view in order to monitor the respiratory motion of the liver/diaphragm, see Fig.4.8. Only a part of the data acquired within this trial was used for the following study of physiological signals. It consisted of 7 examinations, each containing 4 dynamic image series with different breathing patterns, see details in Annexe, A.

4.4.0.2 Image-based respiratory signals

An automatic image post-processing registration method had to be chosen for liver/diaphragm motion estimation: several methods based of optical flow were available in the laboratory, and the most recently published method was used, Brox et al. [13]. As lungs appear very dark and liver presents more or less uniform intensities, motion detection with image post-processing should not be difficult. However, SSFP susceptibility artifacts around anterior and posterior body/air interfaces (left in Fig.4.9), fluctuating vascularisation in the liver and the lungs,

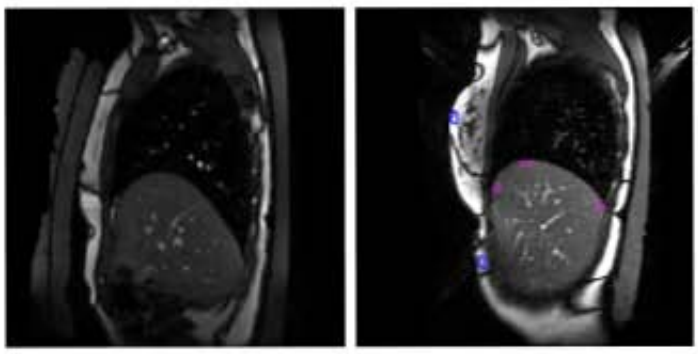

Figure 4.8*: Imaging performed during the acquisition of different respiratory signals: sagittal slice for monitoring respiratory motion of the diaphragm/liver(left), and regions of interest for motion extraction after automatic image registration in pink (right)*

occasional low-signal regions (right in Fig.4.9), and accelerometer-induced artefacts compromised the efficiency of motion detection.

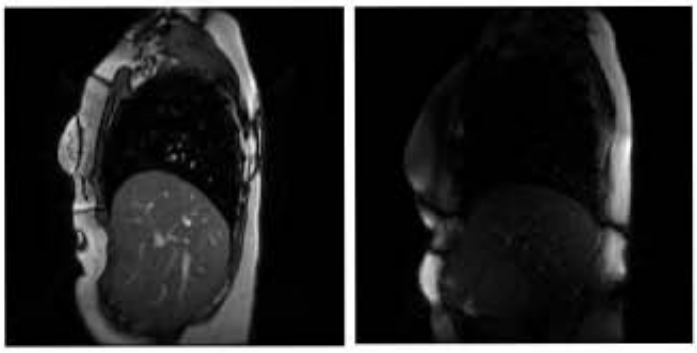

Figure 4.9*: Image artefacts and issues compromising image registration: SSFP susceptibility artefacts-dark circles around body/air interfaces (left) and loss of signal in the region of the liver (right)*

Five regions of interest were drawn manually: three on the right liver hemisphere(near the anterior wall, near the posterior wall, in the middle) and two in the abdominal and thoracic zone of the anterior abdominal wall, see 4.8. These regions were chosen because they all exhibit respiratory motion in a slightly different manner, especially in terms of direction and phase. For instance, the abdominal wall moves mostly in the anterior-posterior direction, whereas the liver moves mostly in the superior-inferior direction. Besides, they can be in phase, out-of-phase, or have a slight phase shift. The purpose of this study was to try to inspect these differences and provide a better insight into the relationship between internal and external respiratory motion. However, several issues prevented this purpose from being fulfilled.

The success of image registration and motion estimation was verified by visualising the registered image series. In most cases, the liver dome appeared almost stationary, though in about 15% of cases some residual motion was visible. Besides, even though the central part of the liver/diaphragm was registered rather correctly, the registration of border regions, near the anterior and posterior wall, and also the anterior wall itself, was not reliable enough. Finally only the signal obtained from the region of interest on the liver dome was exploited and used for comparison with external accelerometer-based and standard (pneumatic belt) respiratory sensors.

4.4.0.3 Accelerometer-based respiratory signal

The signal from the accelerometer-based sensor represents the acceleration of the surface on which the sensor is fastened. Since all the other physiological signals represent a sort of displacement (respiratory belt represents global inflation or shrinkage of the abdomen, and the image-based signals represent the displacement of the liver dome), the acceleration has to be transformed into displacement. Besides, the GRICS motion model relies mainly on displacement signals.

This transformation can be done by integrating the signal twice. However, several problems are encountered. First, the integration involves the addition of a constant, which corresponds to the initial state of the system (initial velocity when integrating acceleration for instance). Second, if the signal has a DC component in terms of slight shifts and imperfections of the baseline, the integration will amplify the error and an additive simile-quadratic component will appear in the result. Consequently, after the second integration, a simile-cubic component will appear and compromise the signal. Besides, the observed signals are actually an oscillatory system. Therefore, before each integration, the mean is subtracted, and after each integration, a high-pass filter is applied, in order to eliminate all the low frequency inaccuracies. The cut-off frequency of the filter was determined experimentally, and was set to 0.13Hz. The displacement signals obtained with this method were then used for comparison with other physiological signals.

4.4.0.4 Comparison

The correlation coefficient was calculated for each pair of signals. Although it is not a powerful tool in statistics, the correlation coefficient is useful in signal processing, when probabilistic correlation between signals is of interest. The signals from different sensors are not intended to be absolutely the same, but they have to convey approximately the same information about periodic respiratory variations. Besides, phase shifts were observed between them, which is rather expected because different sensors don't measure motion at the same place and in the same manner: respiratory belt measures a global averaged motion of the thoracic cage or abdomen,

accelerometer-based sensor measures local motion on the abdomen surface, and the image-based signal measures the internal motion of the upper liver dome.

Another reason for adopting the correlation approach, is the GRICS motion model used in these doctoral studies for motion compensation in image reconstruction, described in 5.1.1. This motion model states that the displacement of an image voxel during acquisition is equal to a linear combination of physiological signals. This implies that the displacement has to be correlated to physiological signals, for the model to be accurate. Therefore, any signal correlated with motion occurring in the field-of-view is of interest. Correlation implies that the amplitude of physiological signals has no importance, but that temporal amplitude modulations and phase shifts are crucial for ensuring model accuracy.

At first, attempts were made at estimating the observed phase differences between signals, in order to deduce a pattern. For this purpose, cross-correlation was calculated between two signals and the phase shift corresponding to a maximum of the absolute value of the cross-correlation function was chosen. The maximum in question had to be an appropriate local maximum, not necessarily the main maximum, because not all phase shifts correspond to reality. Constraints have to be imposed in order to detect only realistic phase shift: however, this requires making assumptions which are not really investigated. For instance, one could assume that externally detected signals would be rather late compared to internally measured motion. This implies searching for local maxima only in negative shifts of external signal with respect to internal signals. One could also assume that both positive and negative shifts are possible, because of different physiology, but that it is limited to one half or one quarter of the respiratory period. Out-of-phase signals (phase shift of π) are the same from the correlation point of view, because when out-of-phase, signals can be obtained from one another by multiplying them with -1. Any phase shift at the order or respiratory period or higher cannot correspond to reality. All these assumptions were tested, but there was no pattern observed: not only results couldn't lead to obtaining a systematic approximate value of phase shifts for certain cases, but they couldn't even lead to a conclusion that one sort of signal is systematically late with respect to another. This heterogeneity of results was attributed to differences in intra- and inter- subject breathing physiology.

Comparison was also performed between thoracic and abdominal respiratory belts, which are supposed to provide slightly different, dephased information about breathing. However, in the exploited data, the two belts tended to provide approximately the same signal in most subjects. The average correlation coefficient between them was 0.8, and no notable differences in phase were observed.

Finally it was concluded that a simple correlation coefficient, with no phase shift correction or estimation, is appropriate for the comparison between accelerometer-based sensors, respiratory belts and image-based motion estimation. This was subsequently used by Laure Rousselet at the end of the research trial to quantify the differences and similarities between different physiological signals, in order to

validate the use of the accelerometer for measuring respiratory motion.

4.5 Conclusion

There exist different sensors for measuring physiological motion, though there is much room for the development of new sensors and for the exploration of physiological motion. Respiratory motion, which was of most interest in these studies, can be measured with different methods: pneumatic respiratory belts, diaphragm navigator echoes, central k-space line, accelerometers etc. However, most of these sensors provide rather similar information. Sometimes, depending on the structures in the field-of-view, the overall information provided by these sensors might not account for all different movements caused by breathing, even with the help of motion modelling. Even if not all the aspects of motion are taken into account, it is still useful to compensate at least a part of motion-induced problems in the images. In this work, respiratory motion was measured with pneumatic respiratory belts and with a signal extracted from the ECG R peak amplitude.

Chapter 5

DCE-GRICS

The starting point for these PhD studies was **GRICS**, an image reconstruction method with integrated motion estimation and compensation, previously developed in the IADI Lab, Odille et al. [61]. The main purpose was to expand the idea of GRICS to a more general framework, in order to apply it to Dynamic Contrast-Enhanced (DCE) MRI. In this chapter, GRICS is first described in its original form. Then, contributions of this doctoral work are exposed. Firstly, GRICS was extended in order to perform motion compensation of a pair of pre- and post-contrast images. Secondly, a new method, named DCE-GRICS, was developed in order to compensate for inter-TR and inter-image motion in a dynamic contrast-enhanced image series. DCE-GRICS was validated on the example of myocardial perfusion DCE-MRI, and published as a full paper in the peer-review journal Magnetic Resonance in Medicine, Filipovic et al. [31].

5.1 GRICS

Parallel imaging notation is the same as in 1.2.2, except that the image will be denoted as ρ instead of f, so as to distinguish the temporal frequency f and the image. Let's define in addition a linear spatial transformation operator T, in other words an interpolation operator. The spatial transformation is arbitrary, non-rigid, and the displacement of each pixel can be different. When applied to an image, $T\rho$, it results in a spatially deformed image.

A framework for integrating motion compensation into the process of image reconstruction emerged first in Batchelor et al. [5]: the operator T was incorporated in the equation of generalised SENSE (1.26). If the motion of an imaged object ρ during the acquisition is known, then the spatial transformation operator is known at each moment of the acquisition. In that manner, a motion-compensated equation can be written for each k-space sample. Instead of regarding the imaged object as static and identical for all acquired k-space samples, the imaged object is spatially

transformed to its true position at each t_i instant of data acquisition. Then the equation for the k-space sample acquired at instant t_i is written. N_{Tacq} is the number of acquisition instants and thus the number of equations. Here only the case of Cartesian sampling will be considered, so that the gridding operator is suppressed.

$$s = E\rho = \xi \cdot FT \cdot c \cdot T \cdot \rho \tag{5.1}$$

Unfortunately, motion and T are usually unknown, so that the system gets too underdetermined, especially in the case of undersampling. Therefore, additional equations are needed in order to solve for ρ. **GRICS***(Generalised Reconstruction by Inversion of Coupled Systems)*, Odille et al. [61], solved this issue by introducing a motion model and an additional equation for motion estimation. It reconstructs one static image from k-space samples acquired during the motion of imaged objects.

5.1.1 Motion model

The motion model is linear and separable in the imaging coordinate system. It is based on the idea that physiological signals are correlated with the motion of the imaged object: the displacement $u_i(r,t)$ of the imaged object, in each spatial dimension i, is spatially and temporally variant, and can be modelled as a weighted linear combination of N_K physiological signals $M(t)$:

$$u_i(r,t) = \sum_{k=1}^{N_k} \alpha_{i,k}(r) M_k(t) \tag{5.2}$$

or in vector notation

$$u = \alpha M \tag{5.3}$$

The coefficients $\alpha_{i,k}(r)$ are spatially variant and represent the weights for each spatial dimension i and each physiological signal k. This model is a very good approximation of the reality if and only if there exists a very strong, if not total, correlation between physiological signals and all the different movements of all the organs in the field of view. Therefore, depending on the observed organs, the type of physiological signals has to be chosen with care. Unfortunately, as mentioned in 4.2, the number and diversity of physiological signals is rather limited, and sometimes insufficient, but new sensors are slowly emerging.

5.1.2 Motion detection equation

Motion detection in GRICS is build on two assumptions:

- the difference between the estimated spatially deformed images and the actual moving imaged object is small

- the motion model is applicable: the displacement of the imaged object is correlated with the available physiological signals

If the image estimate is considered accurate, and the motion operator estimate is $\hat{T}$, the deformed image $(\hat{T}\rho)(r)$ can be described as the first order Taylor expansion around the accurate deformed image $T\rho$ as:

$$\hat{T}\rho = T\rho + \frac{d(\hat{T}\rho)}{dx}\delta x + \frac{d(\hat{T}\rho)}{dy}\delta y \tag{5.4}$$

$$\hat{T}\rho - T\rho = \nabla(\hat{T}\rho) \cdot \delta u \tag{5.5}$$

δu contains displacements in each spatial dimension between the current motion estimate $\hat{T}$, and the real motion operator T. It is therefore the correction of the currently estimated displacement. Since $\hat{T}\rho - T\rho$ is the difference between the estimated moving image and the real moving imaged object, applying the generalised SENSE operator will result in the residue ϵ (the difference between the actual acquired raw data, and the raw data obtained by applying the generalised SENSE operator to the estimated moving image).

By modelling T with the previously described motion model (5.3), the residue can be furthermore expressed as a function of the correction of motion model coefficients. This yields the second GRICS equation, which solves for the correction of the motion estimation (motion model coefficients).

$$\epsilon = \xi \cdot FT \cdot c \cdot \nabla(\hat{T}\rho)M \cdot \delta\alpha \tag{5.6}$$

5.1.3 Solution of the coupled system

The coupling (5.1) and (5.6) leads to a system of two linear equations to be solved in a fixed point iteration:

$$\begin{cases} s = E(\alpha)\rho \\ \epsilon = R(\rho, \alpha)\delta\alpha \end{cases} \tag{5.7}$$

First, it is assumed that the motion is accurately known, and α are set to an assumed initial value. The first equation is then solved only for ρ with an iterative numerical method. Then, after assuming that the obtained solution $\hat{\rho}$ is accurate and that the discrepancy ϵ is due to an erroneously assumed $\hat{T}$, the second equation is solved for $\delta\alpha$, which represent δu and thus the correction for $\hat{T}$. A new estimation of $\alpha = \alpha_{old} + \delta\alpha$ is obtained, and fed into the first equation. The described process is then reiterated until the discrepancy ϵ is diminished to a certain level. Each equation is solved with L_2 norm minimisation:

$$\begin{cases} min \parallel s - E(\alpha)\rho \parallel_2 \\ min \parallel \epsilon - R(\rho, \alpha)\delta\alpha \parallel_2 \end{cases} \tag{5.8}$$

which leads to the following Euler equations:

$$\begin{cases} E^H E\rho = E^H s \\ R^H R\delta\alpha = R^H \epsilon \end{cases} \tag{5.9}$$

In practice, the initial value for T is assumed to be an identity operator, i.e. an interpolation operator with displacement $u = 0$, or $\alpha = 0$. The numerical solution of each equation is performed by GMRES, Saad [80].

A multiresolution framework is used, starting with a resolution of 32 voxels, with each next resolution being the double of the previous one.

For a better conditioning of the equations, regularisation is used. The first equation is regularised with a simple Tikhonov regularisation, by adding the minimisation term $min\{\lambda_1 \parallel f \parallel_2\}$. This term performs a certain spatial smoothing of the image, the impact of which is determined by the regularisation parameter λ_1. The second equation is regularised with a gradient Tikhonov regularisation, by adding the minimisation term $min\{\lambda_2 \parallel \nabla(\alpha + \delta\alpha) \parallel_2\}$. This term performs strong spatial smoothing on motion coefficients, in order to spread the motion information detected at the edges toward the interior of the objects, thus ensuring a consistent motion of each whole moving object. Its regularisation parameter λ_2 is a compromise between motion inconsistency and smoothing. The regularised system becomes:

$$\begin{cases} (E^H E + \lambda_1 I)\rho = E^H s \\ (R^H R - \lambda_2 \nabla^2)\delta\alpha = R^H \epsilon + \lambda_2 \nabla^2 \alpha \end{cases} \tag{5.10}$$

In the first application of GRICS, Odille et al. [61], this system of equations was shown to converge when:

1. the imaged object is over-sampled, usually fully sampled 2-3 times
2. λ_1 is set around 0.1
3. λ_2 is set around 0.01 $\parallel \epsilon \parallel_2$

As already mentioned, the equations are written for each acquisition instant t_i, during which one k-space sample is acquired. In the Cartesian setting, samples in the frequency-encoded dimension are acquired extremely swiftly with a basic pulse sequence. Therefore, as described in 2.1, any motion during the acquisition of all frequency-encoded samples for one phase-encoding step can be neglected for current applications of GRICS. Consequently, the equations can be written for each phase-encoded line. Still, the dimensions of such a system are very large, requiring considerable resources in terms of CPU and RAM. In order to palliate this issue, the system can be further reduced by discretising physiological signals more roughly. Different discretisation levels of normalised physiological signals were tested, and a choice of 8 levels was finally made. Because of this discretisation, of the pseudo-periodicity of physiological signals, and of some motion (mostly respiratory)

being relatively slow compared to data acquisition, it is highly likely that groups of phase-encoded lines will correspond to the same physiological position. Hence, according to the physiological position to which they are assigned, these groups of phase-encoded lines can then be mapped into one ξ and combined into one same equation. In this manner, the system of equations is considerably reduced. This is the usual implementation of GRICS.

The final reconstructed image represents the moving imaged object in its average physiological position, i.e. the position corresponding to the zero value of normalised physiological signals.

5.1.4 Coil sensitivity maps

Coil sensitivity maps are required for any equation based on SENSE. On clinical scanners, coil sensitivities are usually estimated before actual image acquisition, with a calibration pulse sequence. This method may be rather accurate, but it assumes that sensitivity maps do not change during image acquisition. Of course, sensitivity maps are influenced by many parameters, such as patient motion in the bore, coil motion, etc. For this reason, and also in order to suppress the calibration pulse sequence, auto-calibrating methods have been developed: sensitivity maps are extracted from acquired image data, without additional acquisitions. A simple and rather popular method is to reconstruct simply (with an FFT) the images from each coil, and divide them by the sum of squares of all coil images. Since coil sensitivity maps are designed to be smooth, only the central part from the acquired k-space data is used for sensitivity calculus, instead of full k-space data. Issues arise when k-space data are undersampled: the sensitivity maps will exhibit similar aliasing artefacts as the images, which might compromise unaliasing reconstruction methods. In GRICS, especially since there is no undersampling, this simple auto-calibrating method is used: the smoothness is ensured by taking into account only the central quarter of k-space data.

5.1.5 Applicability to dynamic MRI

GRICS has been designed for the reconstruction of one (2D or 3D) motion compensated image from over-sampled k-space data acquired in the same field of view. Standard, or generalised SENSE reconstruction, assumes that the imaged object is static and identical during the whole acquisition. GRICS alleviates this assumption by allowing the imaged object to move and by taking into account this motion. Since the system of equations is designed for the reconstruction of only one image, it can be applied in dynamic MRI only if each dynamic image is over-sampled and reconstructed more or less separately, as in cardiac CINE-MRI, shown in Odille et al. [62]. This solution is not convenient for the application to Dynamic Contrast-Enhanced MRI, because each temporal image is sampled either fully only

once, or even undersampled. This issue generated the subject for this PhD, i.e. designing a method for motion compensated reconstruction of Dynamic Contrast Enhanced-MRI, based on GRICS.

5.2 Introducing one step contrast change in GRICS

The simplest contrast-enhanced MRI technique, from the reconstruction point of view, consists in injecting the contrast agent, waiting for some pre-determined time, and then acquiring a contrast-enhanced image. Therefore, this technique was considered in the first place for the extension of GRICS to contrast-enhanced imaging.

In clinical practice, contrast-enhanced regions in the image are detected and evaluated visually, but it would be useful to do the same thing quantitatively, by performing a subtraction between the contrast-enhanced and the pre-contrast image. Before this, it must be ensured that the two images are registered, and also artefact free. This issue can be solved by GRICS in two manners:

1. the two images are reconstructed with GRICS separately, for the correction of inter-TR motion artefacts

2. the first GRICS equation((5.7)) is solved separately for the two images, while the second equation is common, i.e. the motion coefficient maps are the same for the two images: this includes both inter-TR motion artefacts correction and the registration of both images to the same (average) physiological position

These versions require several repeated acquisitions of full k-space data for each image, which lengthens the acquisition and is not very suitable for clinical application, especially when contrast agent injection is involved. When the contrast enhanced image is acquired, the contrast reaches a rather steady state and is deemed constant during the acquisition, which might be less true if the acquisition was considerably lengthened.

The first attempt at introducing the notion of contrast change in GRICS consisted in assuming a one step contrast change. The second (contrast-enhanced) image was described as the sum of the first (pre-contrast) image and a contrast change map. This can be viewed as if the unknown image ρ in (5.7) was replaced with

$$\rho(r,t) = \sum_{i=1}^{2} \beta_i(r) B_i(t) \tag{5.11}$$

where $B_1(t) = 1$ and $B_2(t) = \Theta(t - t_1)$ (a step or Heaviside function), and t_1 marks the beginning of the acquisition of the second (contrast-enhanced) image. The unknowns are the coefficients $\beta_i(r)$, which are spatially varying functions,

each having the same dimensions as the unknown images, with β_1 representing the complex intensity of the pre-contrast image, and β_2 the contrast change map (i.e. the subtraction of contrast-enhanced and pre-contrast image). The left side of the first equation in (5.7) contains k-space data for the two images, and the right side contains respectively the pre-contrast image, and the contrast change map.

This equation system is very similar to the second version of how GRICS can be applied to this contrast-enhanced MRI technique, mentioned above. The number of unknowns is the same, the second equation is the same (motion coefficient maps are common to the two images). The only difference lies in the unknowns in the first equation: they do not represent complex image intensities for the two images, but the pre-contrast image intensity and the difference between the two images. Since motion coefficient maps are common to the two images, the average physiological position will be identical for the two images, so that they will be automatically registered to each other.

In order to evaluate this method, the following test was performed on a volunteer, because there was no suitable standard clinical images to collect, and because contrast agent couldn't be injected to a volunteer. Since kidneys move considerably with respiration, full k-space data were acquired several times with a balanced SSFP sequence, in free-breathing, for a slanted frontal slice passing through both kidneys, in order to obtain the pre-contrast image (left image in Fig.5.1. Then, test tubes with different concentrations of Gd were attached to the abdomen in order to be in the field-of-view. The same slice was imaged in the same manner in order to obtain the contrast-enhanced image (right image in Fig.5.1). This was a rather simple test, with high contrast change appearing in the background of the image. Respiratory signals from pneumatic respiratory belts, as well as acquisition window timing, were acquired with the SAEC, see 4.3. Raw data, phase-encoding order and images reconstructed in the standard manner were collected from the MRI scanner.

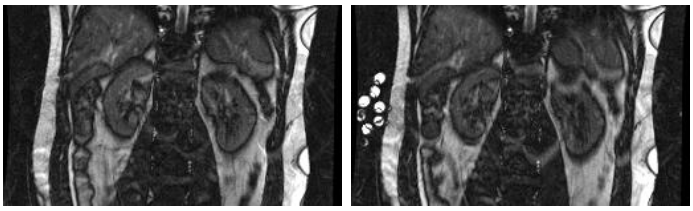

***Figure 5.1**: Test images for one step contrast change (standard reconstruction): pre-contrast image (left) and contrast-enhanced image with added Gd test tubes (right)*

These test images were then reconstructed with the previously described modified GRICS with one step contrast change. The method was tested with two repeated acquisitions of full k-space data for each image, but also with only one full k-space per image. The latter is obviously preferable, since usually only one k-space

data set is acquired in the clinical setting, but it failed: the reduced amount of data caused the system of equations to be too badly conditioned. The test with two repetitions per image was successful: inter-TR motion artefacts were corrected, the two images were registered, and the contrast change was well detected and depicted. The result is presented in Fig.5.2.

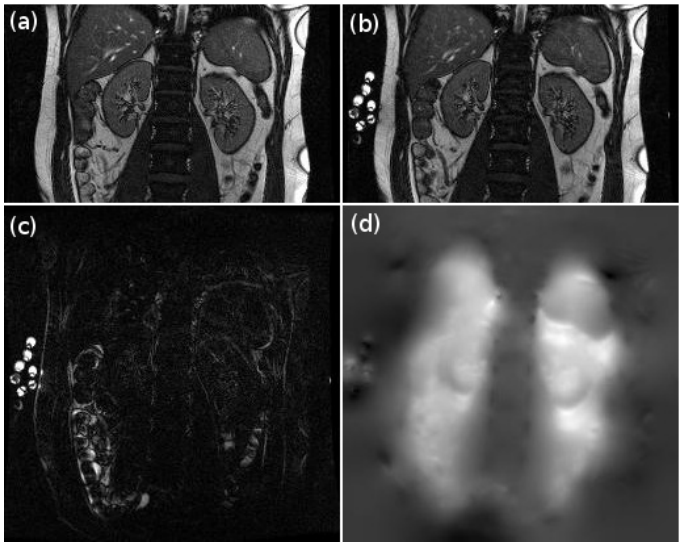

Figure 5.2*: Magnitude of the images and maps reconstructed with the modified GRICS with one step contrast change: (a) pre-contrast image, (b) contrast-enhanced image, (c) contrast change map, (d) motion coefficient map*

The contrast change map should have appropriate values in the region occupied by the test tubes, and be zero elsewhere. The obtained map presents slight values outside of the test tubes, because of noise and a slightly imperfect motion correction, especially in the intestinal region: kidneys move mostly due to breathing, which is detected by respiratory belts and thus corrected with GRICS, whereas intestines have their own peristaltic motion for which there is no available sensor. Motion coefficient maps present stronger coefficients in the region of kidneys, liver and spleen, which is consistent. They present also strong smoothness, with blurred boundaries between organs, due to the gradient constraint applied in the second GRICS equation. This method can be applied to subtraction contrast-enhanced imaging which suffers from respiratory motion, or any other motion as long as corresponding physiological signal is available. The major drawback is the requirement for more than one fully sampled of k-space data per image.

This method was presented at the ISMRM Conference 2009, Filipovic et al. [29]. It was the first step towards applying GRICS to dynamic contrast-enhanced imaging.

5.3 DCE-GRICS

This new method, Filipovic et al. [31], upgrades and modifies GRICS in order to perform non rigid motion compensated reconstruction of Dynamic Contrast-Enhanced MR image series, including both motion artefact correction (inter-TR motion) and registration (inter-image motion). Before thorough validation, the method was presented at the ISMRM Conference 2010, Filipovic et al. [30]. In order to transform the single image GRICS reconstruction into a reconstruction of dynamic contrast-enhanced image series, the unknown image ρ in (5.7) is replaced by a contrast change model compatible with the equations.

The proposed contrast-change model is based on two assumptions:

1. Intensity vs. time curves, corresponding to each voxel in the dynamic contrast-enhanced series, can be represented in the same vector space, i.e. approximated with a linear weighted combination of N_B intensity-time curves $B_i(t)$.

2. Contrast change does not cause notable temporal change in the phase of a non-moving voxel. Small residual changes can be represented in some generic vector space.

In view of the **first assumption**, it was opted for building the functions $B_i(t)$ with customised normalised B-splines with uniformly spaced knots. This choice was made because B-splines are very generic functions, they have strong modelling capacities, and their temporal resolution can be customised.

At first, attempts were made at building some basis functions specific to intensity-time curves occurring in DCE-MRI. Principal component analysis was tested on intensity-time curves extracted from myocardial and renal perfusion examinations. However, such an approach showed to be unreliable: firstly, a considerable amount of different intensity-time curves should be processed in order to cover all possible cases, and secondly, the variability in curves is very high, due to different injection quantities/concentrations/rates, especially in presence of pathology. Since diagnostic post-processing of intensity-time curves reposes strongly on the timing and shape of contrast change, the danger of loosing relevant pathological features with insufficient or inappropriate modelling was deemed too great for undertaking such an approach.

Normalised uniform B-splines, with temporal knots corresponding to frame acquisition times, allow for almost arbitrary intensity change between each image/frame, and thus offer too many degrees of freedom. Since intensity-time curves are rather smooth, prior information was introduced in terms of temporal smoothness: the number of basis functions was reduced, each function was widened, and thus the number of unknown coefficients β was also reduced.

The optimal contrast change model, with the least temporal smoothing possible, was chosen empirically by constructing a series of normalised uniform B-splines

with temporal knots two times sparser than temporal knots of the image series. To this was added a constant function, 2 additional B-splines at the beginning of the series and 2 at the end, for a better determination of the beginning and the end of intensity-time curves and for a symmetrical model. The number of B-splines, N_B, for a dynamic image series of N_t images, was finally equal to $(N_t-3)/2+1+4$. An example of this B-spline based contrast change model is illustrated in Fig.5.3 for a temporal series of $N_t = 11$ images.

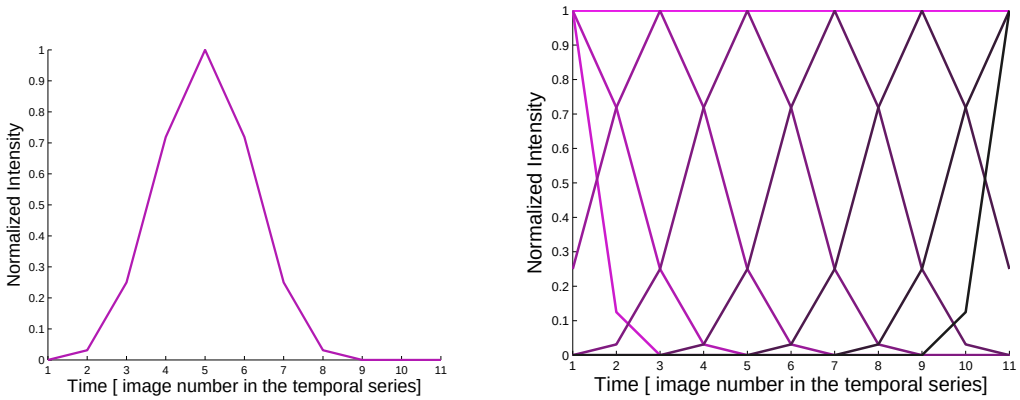

***Figure 5.3**: The customised discretised B-spline (left) and the whole set of intensity-time functions for the contrast change model designed for a temporal series of 11 images*

In view of the **second assumption**, a single phase map Φ was calculated by standard reconstruction of an image in the middle of the temporal series, and included in the contrast change model as the approximation of each image phase. It should be pointed out that motion-induced phase changes are taken into account by the motion compensating part of the algorithm. The image estimate ρ in (5.7) becomes

$$\rho(r,t) = e^{j\Phi} \sum_{i=1}^{N_B} \beta_i(r) B_i(t) \tag{5.12}$$

Weight coefficients β have complex values in the general case. Since intensity-time curves represent image magnitude and thus have real values, the imaginary part of β accounts for small changes in image phase, with respect to Φ. By choosing the generic contrast-change model described above, the assumption that those small phase changes can be represented with this same model is not aberrant.

Since all the notions introduced above are inherently linear, their integration into GRICS does not alter in any way the linearity of the equations. After combining (5.7) and (5.12), the equations for DCE-GRICS applied to a whole temporal image

series are:

$$\begin{cases} s = E_{contrast}(\alpha)\rho \quad , \quad E_{contrast} = \xi \cdot FT \cdot c \cdot T \cdot \Phi \cdot B \\ \epsilon = R(\rho, \alpha)\delta\alpha \end{cases} \tag{5.13}$$

It should be noted that the first equation of the novel method in (5.13) solves directly for the coefficients β of the contrast change model, and only indirectly for the images.

These modifications do not affect the second GRICS equation. It is written as in GRICS for each group of k-space samples acquired in the same physiological position, but the grouping is done only inside the same contrast change step, corresponding to one dynamic image frame. So as not to enlarge system dimensions too much, it is assumed that the contrast change is negligible during each physiological position and also during the acquisition of one whole dynamic image. The veracity of this assumption depends on the acquisition time: it is rather acceptable in most applications of DCE-MRI (myocardial, renal perfusion). However, it might not be true in some DCE-MRI applications with very low temporal resolution and high spatial resolution. Therefore, the temporal resolution of contrast change in the DCE-GRICS system of equations should be adapted by considering the acquisition time of one image with respect to the rapidity of contrast change.

5.3.1 Size reduction of the equation system

Convergence to the "right" solution implies the ability of DCE-GRICS to distinguish between contrast change and motion, which is a rather problematic issue in image processing. Since the equilibrium between contrast change and motion detection is quite fragile, the system of equations calls for very good conditioning. Therefore, instead of computing the intensity change coefficients for each voxel, only voxels with notable intensity changes in time are taken into account in the equations. The selection is performed automatically by analysing the characteristics of low resolution time series (about a quarter of central k-space lines per frame) in *r-f*, commonly known as *x-f*, space, where f is the temporal frequency. The importance of temporal intensity changes for each voxel is evaluated with the power of its non-DC temporal frequency spectral components:

$$SP(r) = \sum_{f \neq 0} |\rho(r, f)|^2 \tag{5.14}$$

where $\rho(r, f)$ is the Fourier transform of the image ρ from space-time domain to space-(temporal frequency) domain. The selection mask contains voxels with the value of $SP(r)$ greater than an empirically determined threshold. The obtained mask contains not only areas with intensity changes due to contrast agent injection,

but also areas with notable motion, though these two types of areas usually overlap more or less. The size of the matrix to be inverted when solving the first equation of the coupled system in (5.13) is thus reduced. For the voxels outside the mask, the coefficients β are calculated only for the first contrast change model function (a constant equal to one), and set to zero for all other functions.

GRICS requires the number of acquired full k-space data to be greater than 1 for the equation system to be over-determined. DCE-GRICS is over-determined by default with one full k-space data per image(frame). Let N_t be the number of images(frames) in the temporal series, N_r be the overall image spatial dimension ($N_x * N_y$ for 2D, $N_x * N_y * N_z$ for 3D), N_{mask} the number of voxels in the mask previously mentioned, N_B the number of basis functions for the contrast change model, N_c the number of coils, and N_M the number of physiological signals. In the case of full sampling, the size of acquired data is $N_r * N_t * N_c$: standard reconstruction solves for $N_r * N_t$ unknowns, whereas DCE-GRICS solves for $N_{mask} * (N_B - 1) + (2 * N_M + 1) * N_r$ unknowns, which is much less in general.

5.3.2 Validation of the method

DCE-GRICS could be applied to many different DCE-MRI techniques, involving contrast change and moving organs, as soon as some physiological signal correlated with that motion is available. In practice, physiological signals used by commercial scanners are the ECG, pneumatic respiratory belt and navigator echoes, though their availability depends on different manufacturers. However, the greatest limitation in the choice of application is the fact that it is not possible to inject contrast agent to volunteers. Only data from clinical patient examinations were available, without any possibility of making changes in pulse sequence options and details, so as not to compromise the outcome of the clinical examination.

After browsing through different possibilities, the most suitable one in the Laboratory IADI turned out to be the application to myocardial perfusion DCE-MRI for the correction of respiratory motion. Since DCE-GRICS performs inter-TR and inter-image motion compensation, the resulting dynamic image series should be registered and free of motion-induced artefacts. The main purpose of this motion compensation is to allow for more accurate post-processing, in this case myocardial blood flow estimation. In order to validate the method, motion compensation and improvement in intensity-time curves have to be validated, which is very difficult for clinical data, since there is no ground truth or gold-standard available. Therefore, in addition to applying the method to clinical data, a simulation was performed in order to test the method in a more thorough and accurate manner.

5.3.2.1 Implementation

The algorithm was implemented in Matlab (The Mathworks, NA, Massachusetts), for 2D image series of arbitrary length. Algorithm's entry consisted of one or two respiratory signals from pneumatic belts, a respiratory signal created from R wave amplitudes of the ECG, the order and the timing of acquisitions of k-space samples, and the raw data. As in GRICS, a multi-resolution iterative approach was implemented, with the starting resolution of 32, and the final resolution of 128 pixels. Physiological signal quantisation was set to 8 levels. The threshold for the selection of pixels with high temporal changes was determined empirically and set to 25% of the maximum. The binary mask was formed with the chosen pixels, and underwent closing and dilating operations for robustness.

5.3.2.2 Application on simulated data

Data In the perspective of creating the most realistic simulation possible, the clinical data, described a bit further in 5.3.2.3, were used as the starting point. Elastic motion was created from acquired physiological signals with the GRICS motion model, ensuring correlation between motion in images and physiological signals. Three different examples of non-rigid motion were used. Contrast change was given in terms of intensity-time curves, generated so as to model typical myocardial perfusion intensity changes. The arterial input function (AIF) was generated with the model derived experimentally in Parker et al. [67], corresponding to the following equation:

$$AIF(t) = \sum_{n=1}^{2} \frac{A_n}{\sigma_n \sqrt{2\pi}} e^{-\frac{(t-T_n)^2}{2\sigma_n}} + \alpha e^{-\frac{\beta t}{1+e^{-s(t-\tau)}}} \tag{5.15}$$

The equation parameters were chosen to be identical to those evaluated in Parker et al. [67]. The model used to generate tissue intensity-time curves is very similar to Awate et al. [4] and corresponds to the following equation:

$$AIF(t) * b_1 e^{-\frac{t}{b_2}} * \delta(t - b_3) * e^{\frac{t^2}{b_4}} \tag{5.16}$$

The second term simulates the residue function, the third term accounts for the time delay, and the forth term simulates signal dispersion. Two sets of three curves with different parameters and arterial input functions, given in Table5.1, were created.

Since there was no baseline T_1 measurement available, the absolute values of the curves could not be converted to signal values. Therefore, there was no interest in setting the absolute perfusion value, because all the intensity-time curves were scaled with respect to image intensities encountered in the clinical data. Described perfusion models are completely independent of the contrast change model used for DCE-GRICS. Examples of generated curves are illustrated in Fig.5.4.

Set	AIF	Curve	b_2	b_3	b_4
1	$AIF(t)$	1	30	10	1
1	$AIF(t)$	2	50	20	1
2	$AIF(1.3t)$	1	70	8	3
2	$AIF(1.3t)$	2	110	30	10

***Table 5.1**: Parameters for different sets of simulated intensity-time curves*

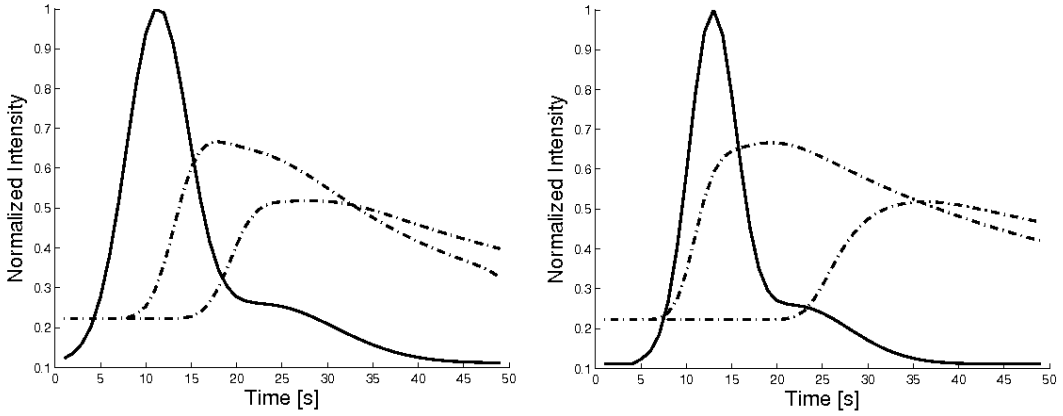

***Figure 5.4**: Example of simulated intensity-time curves: AIF (thick line) and regions in the myocardium (dotted line)*

Finally, the created motion and intensity change were applied to the first complex image from the clinical data. Three adjacent regions of interest were drawn in the heart on this first image, and a different generated intensity-time curve was applied to each region. Each set of curves was combined with each motion model, so that in total 6 simulated examples of dynamic contrast-enhanced image series were created (illustration of an example in Fig.5.5). The image series were then converted to multi-coil k-space raw data. Consequently, the input data for testing DCE-GRICS were of the same kind for both the clinical and the simulated data.

Results Simulated data are aimed at evaluating both the registration performance and the improvement in intensity-time curves. This evaluation is easier compared to clinical data because the ground truth exists: motion and contrast change are known.

In order to evaluate the **motion compensation performance**, the motion model parameters, calculated with the novel reconstruction, were compared to the generated (true) ones. Since physiological signals are mutually correlated in the general case, multiple solutions may exist for motion model parameters. Therefore, instead of calculating directly the error between the true and the novel parameters,

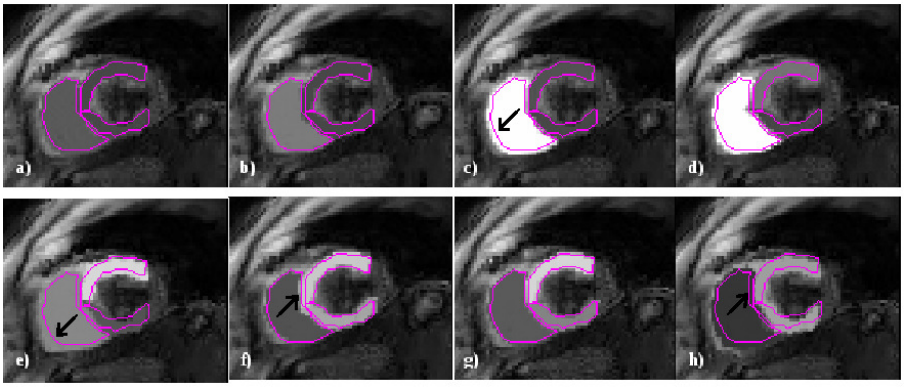

***Figure 5.5**: Temporal illustration of a simulated example: pink lines represent regions of interest drawn for the application of contrast change. Arrows point at the effects of applied motion: contrast-enhanced areas move out of the drawn region of interest*

we chose to estimate the error of the whole motion model in the following way. The regions of interest representing myocardial segments, Association [1], illustrated in Fig.5.6, were transformed into logical masks. The true and the novel motion model were then applied on these masks, generating a series of masks moving in time. Then, an error was calculated in terms of the percentage of pixels not shared between the true and the novel moving mask, with respect to the number of pixels in the true mask. The same error was calculated between the true masks and the static masks, which stand for the standard reconstruction (with no motion correction). These errors were calculated for each region of interest and each time point during motion for each simulated example, separately for inter-TR and inter-image motion.

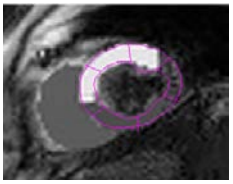

***Figure 5.6**: Segmentation of the myocardium for the simulated data*

Inter-image motion rms error, obtained with the standard reconstruction, was diminished with DCE-GRICS by 71%. Inter-TR motion was diminished by 70%. This demonstrates the accuracy of motion estimation and registration. An example of DCE-GRICS compensation of blurring caused by inter-TR motion is illustrated in Fig.5.7.

In order to demonstrate the **improvement in intensity-time curves** and their accuracy, curves were extracted from the same regions of interest drawn previously for the creation of intensity change. They were calculated in the same manner, i.e.

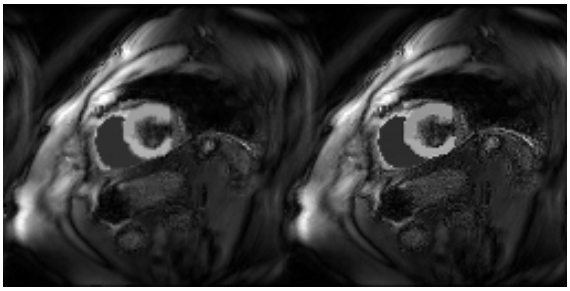

***Figure 5.7**: Inter-TR motion compensation of simulated data: standard reconstruction presents blurring (left) whereas the image is sharper after DCE-GRICS(right)*

by averaging pixel intensities in each region of interest for each time point, for the true simulated data set, the one reconstructed by the standard method and the one reconstructed by DCE-GRICS. Curves from both the standard and the novel reconstruction were compared to those from the true data set by calculating the root mean-square error.

The rms error for intensity-time curves, obtained with the standard reconstruction, is diminished with DCE-GRICS by 76%. An example of intensity-time curves is presented in Fig.5.8.

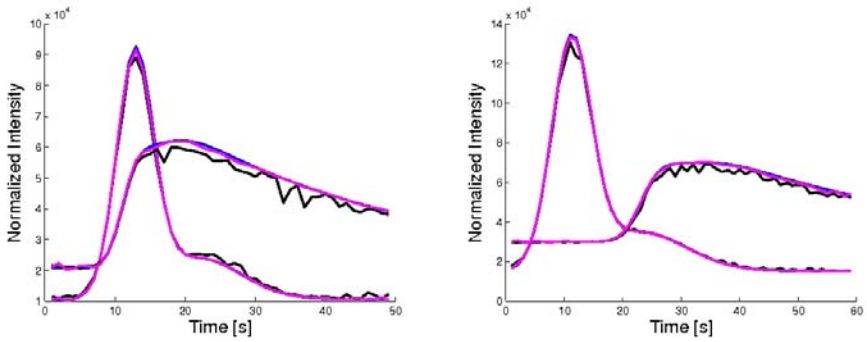

***Figure 5.8**: Intensity-time curves from myocardial segments, generated with the myocardial perfusion model (blue), extracted after standard reconstruction (black), and extracted after DCE-GRICS (pink)*

5.3.2.3 Clinical application

Data Myocardial perfusion is often included in clinical routine cardiac MRI exams. In order to collect data necessary for the validation of DCE-GRICS, standard clinical acquisitions on a 3T clinical scanner (General Electric, Milwaukee,

WI) were simply recorded without any change to the clinical protocol. Collected data comprised full (non undersampled) raw data from an 8-channel cardiac coil, physiological respiratory signals from one pneumatic respiratory belt or two when available, an ECG signal and the clinical images from the scanner, all corresponding to the myocardial perfusion DCE-MRI pulse sequence. Physiological signals were collected through an independent dedicated platform designed for acquiring and processing signals from the MRI scanner, see 4.3. Immediately after GD-DTPA (Dotarem, Guerbet, France) injection (0.05mmol/kg at 4 ml/s rate), the heart was imaged at rest, in free-breathing, for about 1min, with a combined gradient-echo/EPI pulse sequence with interleaved notched saturation, Slavin et al. [85], resolution 128x128 pixels, FOV 175mm, echo train length 4, temporal resolution 1/(RR interval). Other parameters were slightly different for each examination, because they depend strongly on the patient and especially on the heart rate: the number of images in the temporal series for one slice ranges from 50 to 85, and the number of slices from 2 to 4.

Results DCE-GRICS was compared to the standard reconstruction without motion compensation and to the standard reconstruction followed by a post-processing registration method, Rueckert et al. [79], Schnabel et al. [81]. The latter is a non rigid registration method based on normalised mutual information and thus rather suitable for applications with contrast change.

The efficiency of **inter-image motion compensation** was demonstrated in two manners. First, motion-time representations were built by positioning a line on one frame so as to cross the regions with notable contrast change and motion: myocardium, left ventricle, right ventricle, spleen, etc. The same one-pixel-width line was extracted from the dynamic image series reconstructed with DCE-GRICS, and with the standard reconstruction with and without post-processing registration, and presented versus time. Second, a measure of local variability, the total variation, was calculated for each intensity-time curve, and compared for the three different results.

Motion-time representations are illustrated in Fig.5.9. The registration efficiency of DCE-GRICS is clearly visible in the accomplished alignment of contrast-changing, moving lines. Five examples out of 6, reconstructed by DCE-GRICS, present very good motion compensation (Fig.5.9, the two upper examples), and one example, with only one respiratory belt available, presents some residual motion (Fig.5.9, lower example).

The improvement of **intensity-time curves** is demonstrated by comparing them to standard and registered standard curves. Myocardial segmentation, according to Association [1], was performed manually on DCE-GRICS results, on one image per slice, and afterwards applied to the standard and post-processed data. Then intensity-time curves were extracted from all the myocardial segments for DCE-GRICS, for standard reconstruction, and for standard reconstruction followed

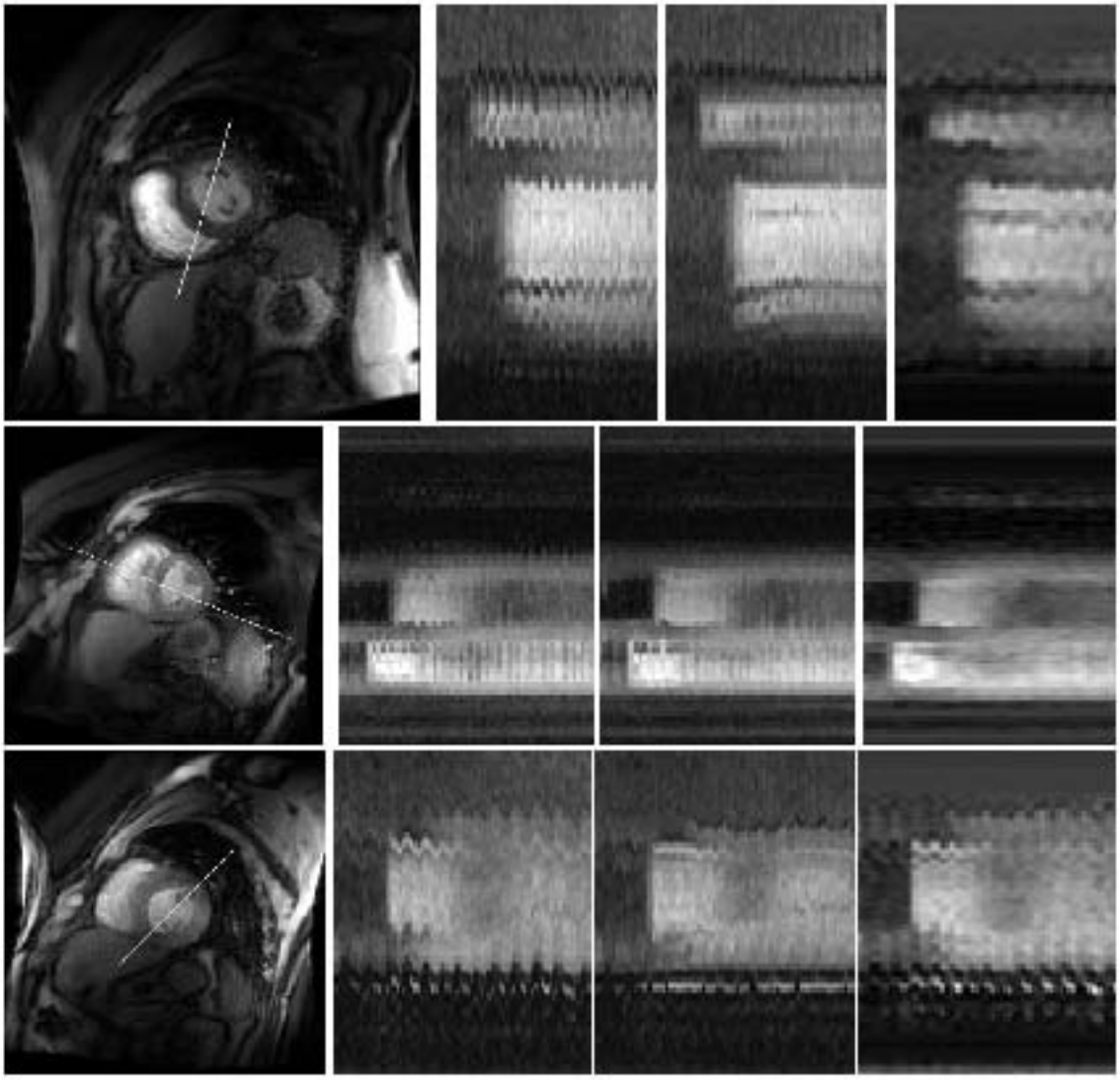

Figure 5.9*: Clinical data: Motion-time representation. From left to right : the first image shows the line used to extract motion-time profiles and the mask used for reducing the number of unknowns in the first equation. The following images represent motion-time profiles, respectively after standard reconstruction, after standard reconstruction followed by post-processing registration, and after DCE-GRICS. The two upper examples present better motion compensation with DCE-GRICS than with standard registration. In the bottom example, DCE-GRICS presents some residual motion.*

by post-processing registration, and then presented against each other.

Results in terms of intensity-time curves are illustrated in Fig.5.10 and Fig.5.11 . The novel curves present considerably lower local variability due to motion. The measures of total variation showed that the post-processing registration diminishes the total variation of the original intensity-time curves by 20% in average, with a standard deviation of 40%, whereas DCE-GRICS diminishes it by 36% in average, with a standard deviation of 22%. This shows that the variability of intensity-time curves, induced by breathing, is reduced by DCE-GRICS better than by standard registration, with a significant difference ($p < 0.01$).

As far as inter-TR motion artefacts are concerned, the used pulse sequence is very rapid, one image being acquired in about 170ms. In this case, inter-TR motion can cause only blurring, which is more difficult to evaluate than ghosting artefacts. In contrast to simulated data where the only source of blurring is motion, in the clinical data there are many sources of noise and blurring due to the acquisition and the pulse sequence, making it difficult to see and evaluate the small difference caused by DCE-GRICS compensation. Besides, during the acquisition of one dynamic image (frame), no more than 20% of the maximum respiratory motion has been observed.

5.3.2.4 Coefficients for the contrast change and motion model

Examples of obtained coefficient maps for the contrast change model are presented in Fig.5.12. Maps corresponding to B-splines describing important instants of contrast change are shown: high values are observed in structures enhancing at these instants, as expected.

Examples of obtained coefficient maps for the motion model are presented in Fig.5.13. High values are observed in the region of moving structures (heart, liver, etc.), as expected. It can be noticed that maps corresponding to respiratory belts present high values in the region of spleen, liver and heart, whereas maps corresponding to the ECG-based signal presents features mostly in the heart. The maps for the superior-inferior direction (in the slanted cardiac short axes plane) have higher values than in the anterior-posterior direction.

5.3.2.5 Parallel imaging

Since DCE-GRICS is based on generalised SENSE, tests with acceleration factors were performed in order to test the robustness of DCE-GRICS in the case of undersampling. Both clinical and simulated data were undersampled a posteriori with an acceleration factor of $R = 1.6$: the central quarter of the k-space was left fully sampled, whereas one line out of two was retained for the higher frequencies. The centre is necessary for determining the mask for the reduction of the number of unknowns for the first equation.

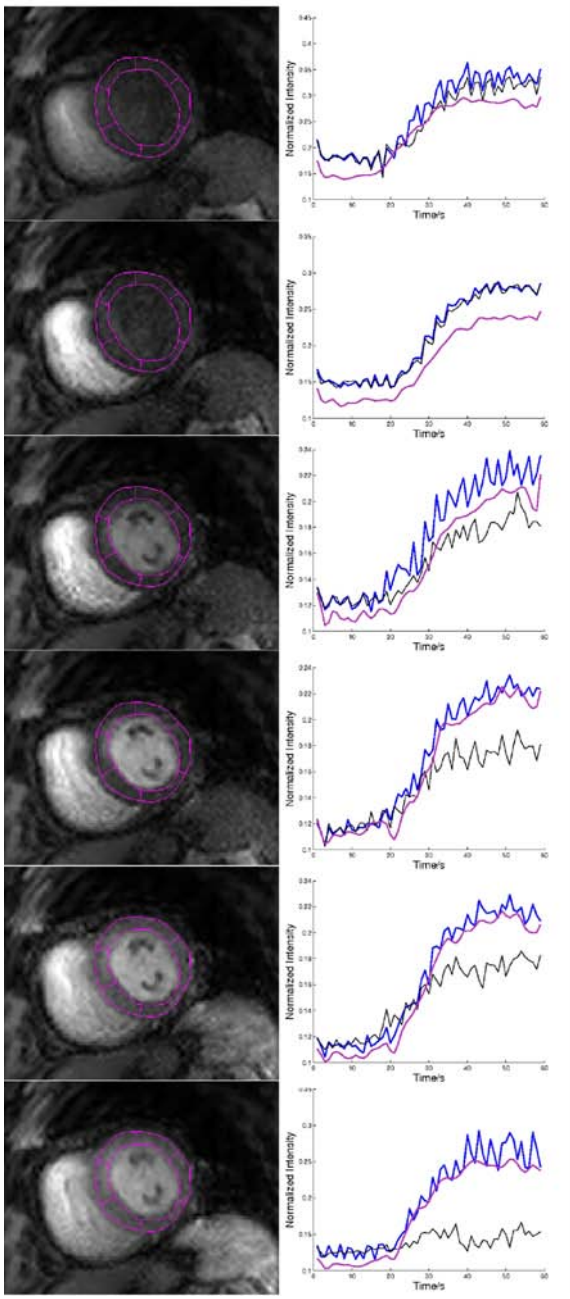

***Figure 5.10**: Clinical data: Intensity-time curves in free-breathing (right) extracted from myocardial segments (left), after standard reconstruction without motion correction (blue), after standard reconstruction with registration (black), and after reconstruction by DCE-GRICS (pink). Image numbers in right top corners represent the corresponding number of cardiac cycles from the beginning of the acquisition.*

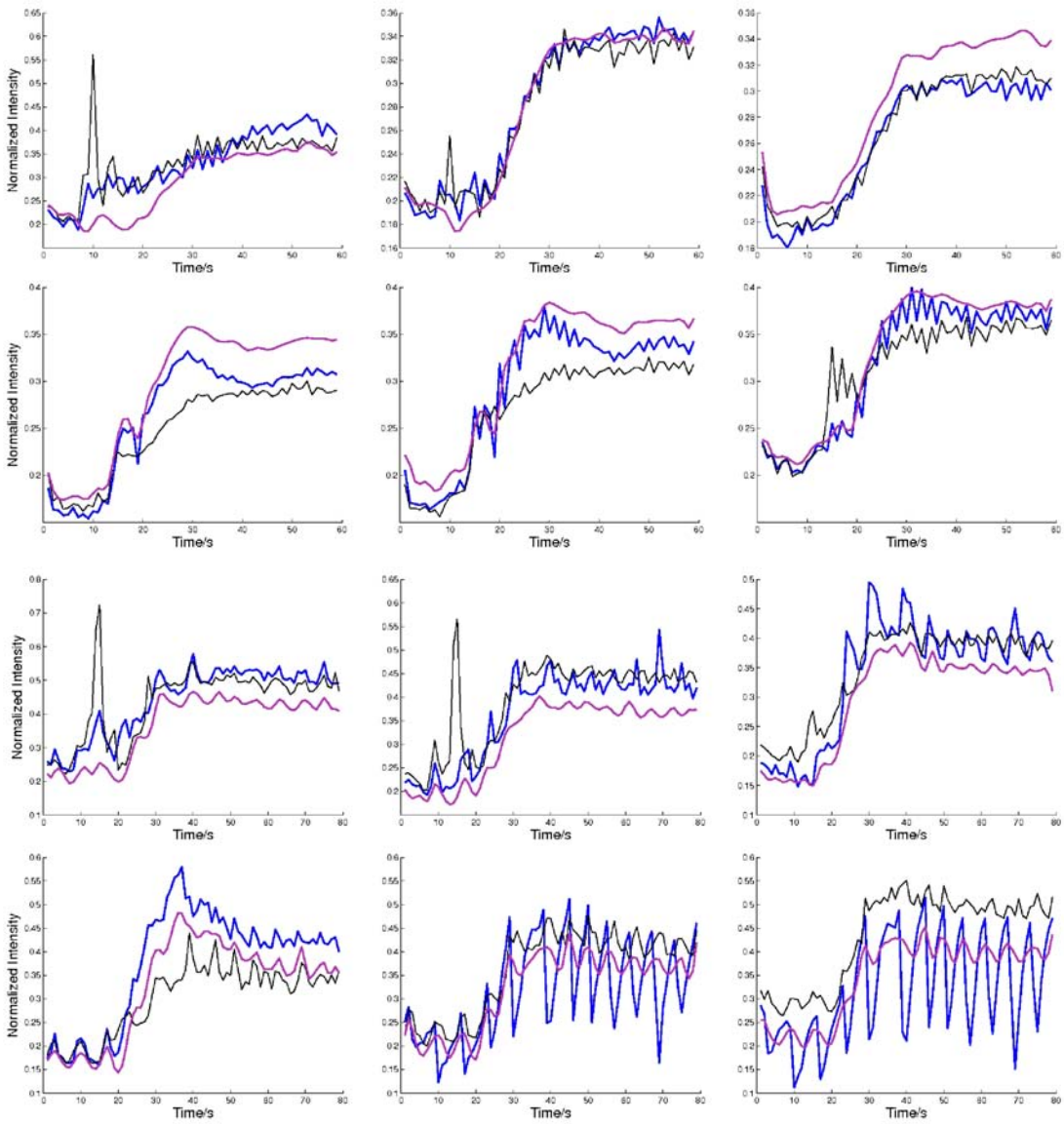

Figure 5.11: *Clinical data: Examples of intensity-time curves after standard reconstruction without motion correction (blue), after standard reconstruction with post-processing registration (black), and after reconstruction by DCE-GRICS (pink).*

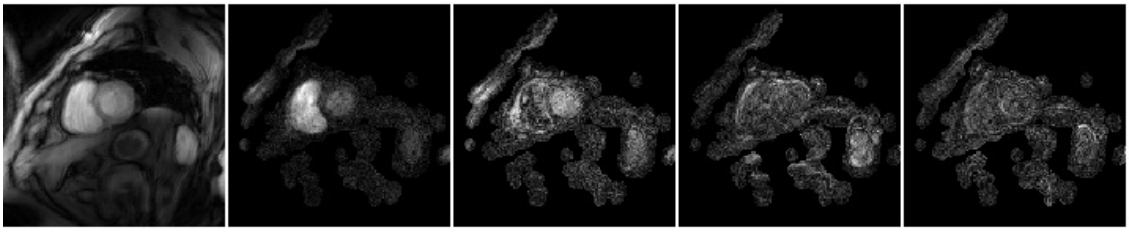

***Figure 5.12**: Contrast change model: coefficient maps for B-splines (from left to right): baseline(pre-contrast) image, enhancement of the right ventricle, enhancement of the left ventricle, myocardial enhancement, and contrast stability period*

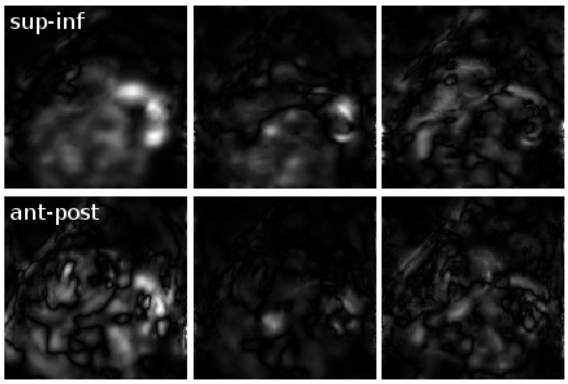

***Figure 5.13**: Motion model: coefficient maps for (from left to right): abdominal pneumatic belt, thoracic belt, and ECG-based respiratory signal (R peak amplitudes)*

For both clinical and simulated data, the robustness of DCE-GRICS with respect to undersampling was evaluated by calculating the rms of the relative error between intensity-time curves obtained with fully sampled data and data undersampled with $R = 1.6$.

This error was in average 2.2% for clinical and 0.03% for simulated data, which shows a certain robustness towards low undersampling. An increase in noise and slight undersampling artefacts appeared in several examples, causing small shifts of intensity-time curves.

5.3.2.6 Physiological signals

The available physiological signals were one or two pneumatic respiratory belts, and R wave amplitude from ECG. One could also use the derivatives of the respiratory belt signals, which account for the dependence of the respiratory component of cardiac motion on respiratory velocity (hysteretic behaviour), [58]. Tests were conducted in order to compare the performance of DCE-GRICS using different combinations of respiratory signals: only respiratory belts, or respiratory

belts with an ECG-based signal or the derivatives of respiratory belt signals. These tests pointed out the amount of correlation between the motion in the field-of-view and the available physiological signals.

The difference in intensity-time curves between DCE-GRICS with an ECG-based signal or without showed to be very small, 2% in average, with a standard deviation of 3%. A similar result was obtained between DCE-GRICS with and without belt signal derivative, the difference being 3.3% in average with a standard deviation of 2.7%. In both cases there was no notable difference in motion observed visually. Besides, the ECG-based signal and the belt signal derivative were not correlated with the respiratory belt signal, the absolute correlation coefficient being beneath 0.15, except for one examination where it amounted to 0.7 for the ECG-based and the respiratory signal. This suggests that the R-wave amplitude signal and belt derivatives do not contribute a lot and are not particularly correlated with the motion (mainly respiratory component of cardiac motion) occurring in the explored data.

5.3.2.7 Discussion

DCE-GRICS includes non-rigid respiratory motion compensation in the reconstruction process. It corrects for motion-induced artefacts, performs registration of dynamic image series, and estimates coefficients for a motion model and a contrast-change model. It performs better than a standard post-processing registration method and stands small undersampling factors.

Validation Evaluating the performance of this new method is difficult for clinical data, because contrast change and motion are not known. The registration gold standard so far is the rigid manual registration, which is limited in performance, operator-dependent and is not comparable to non-rigid registration. The registration method used for comparison was chosen because it belongs to methods less sensitive to contrast change, and its implementation is freely available. The registration methods mentioned in 3.4.1 are not readily available and implementing them based on publications would be prone to errors.

The total variation is a measure of local variability, and depends not only on motion-induced variability, but also on intensity change. However, as the contrast change was well reproduced by registered curves, in this case total variation depends mostly on respiratory motion. The curves might also be validated clinically with a gold-standard method for perfusion parameter extraction, but this calls for a large clinical study and perfusion assessment is still a topic under research.

Concerning inter-TR motion, the correction by DCE-GRICS would be more visible in the case of very irregular breathing and sudden movements, which may occur during stress examination, but unfortunately no such data were available for this study.

Other methods Rapid acquisition methods, such as k-t, or compressed sensing, may reduce motion artefacts by accelerated acquisition, but they do not deal with registration. Compared to post-processing, the advantage of motion compensation in reconstruction is that complete complex k-space data are available from multiple coils before the reconstruction, and the time of acquisition of each k-space line can be put in relation with the respiratory phase, whereas post-processing methods deal only with magnitude images and depend strongly on their quality. Besides, as soon as the respiration is quicker, or acquisition slower, inter-TR motion has to be compensated for, which is difficult and often impossible in post-processing. In addition, in k-t reconstructions for instance, inter-image motion can cause not only misregistration but also motion artefacts, which can be dealt only in reconstruction.

Nevertheless, in the case of rapid acquisitions with good image quality, high resolution, and low contrast change, post-processing techniques perform very well and there is no need to deal with motion compensation through reconstruction. Given the usual compromises in image quality, Kellman and Arai [46], myocardial perfusion is very difficult to deal with in post-processing, so that the reconstruction approach may be more adapted.

Through-plane motion Through-plane motion is an important problem in 2D imaging, and compromises both motion compensation and the examination itself, because any post-processing relies completely on the assumption that the same region is observed through time. Measures of respiratory induced cardiac motion in literature indicate a preponderant motion component in cranio-caudal direction, with a maximum of 25 mm observed in Nehrke and Boernert [57].

It is very difficult to distinguish visually between myocardial shape changes due to different respiratory states, and those due to through-plane motion. Therefore, in order to get a rough approximation of the worst through-plane motion that might occur in this study, two estimations were made and compared to the slice thickness used (9 mm). First, the projection of the worst case (25 mm) on the slice normals amounts to a maximum of 10 mm. Second, if all the motion of the diaphragm, visible in our slices, is considered to be completely due to cranio-caudal motion, then its component on the slice normal is much smaller then the slice thickness, with the exception of one value in one patient of 10mm. Therefore the through-plane motion in these data is not regarded as an important issue, especially compared to other MRI-related shortcomings.

Motion model For ideal motion compensation, the physiological entry signals should be mutually independent and highly correlated with different organ movements. This would enable the motion model to accurately take into account all different displacements of all moving structures in the slice. In practice, the availability of such physiological signals is restrained, due to a small amount of

external devices and to difficulties of using navigators. Physiological signals from respiratory belts may be imperfect because of air leaks, or because of compression by pads or antenna. Besides, inter-patient variability of respiratory characteristics is very high, and has an important influence on the information correlation between thoracic and abdominal belts, and between belts and internal motion. Advances in internal motion measurement in MRI should optimise the results.

Regarding the regularisation of motion model coefficients, the empirically chosen parameter λ_2 corresponds to a compromise between motion inconsistency and over-smoothing, which can cause problems in the case of sharp displacement gradients. Our data present mostly respiratory motion, with different organs moving in a similar manner, so that there was not manystrong regional differences in motion.

Contrast change model The contrast change model should be designed so as to be able to approximate all possible shapes of myocardial intensity-time curves. The model used in this method showed to have sufficient modelling capacities for myocardial perfusion, since the curves simulated by realistic myocardial perfusion models were very well reproduced, without any temporal smoothing. However, the presented algorithm has to be tested in a larger clinical context in order to assess its diagnostic pertinence.

Distinction between contrast change and motion The algorithm has an inherent ability to distinguish between intensity changes due to motion and intensity changes due to contrast agent evolution. This ability is provided by good conditioning and convergence. However, in the case of imperfect motion compensation, the method can converge toward a consistent solution only if the motion still present in the acquired data is accounted for. The only way to do this is to regard the change in intensity due to residual motion as contrast change. Therefore, if motion is not completely accounted for, slight residual motion may be rendered by the coefficients of the contrast change model, in addition to real contrast change.

System conditioning In practice, when dealing with numerical solvers, compromises must be made between system conditioning and the set of possible solutions. To allow more degrees of freedom to the solution, the number of unknowns has to be increased, and consequently, the system has to be better conditioned. As DCE-GRICS aims at being as generalised as possible, and thus implements a non-rigid motion model and a generalised contrast change model, the number of variables is large. In the case of clinical dynamic contrast-enhanced imaging, there is no straightforward possibility of reinforcing system conditioning, because of very high demands in both temporal and spatial resolution. One temporal image (frame) is always sampled either only once, or even less than once (undersampled).

Reducing the number of unknowns in the first equation introduces another limitation in DCE-GRICS: it is assumed that the mask, generated from the low resolution series, encloses all the pixels that present intensity change. The mask selection worked well for all the examples, but the threshold was chosen empirically, and may need to be adapted for other applications.

Other applications DCE-GRICS is extensible in 3D, the only concern being computation resources with greater matrix dimensions. It is potentially applicable to any DCE-MRI examination corrupted by respiration, such as MR renography or liver perfusion, or by some other type of motion, as long as signals correlated with that motion are available.

Pulse sequence Because of pulse sequence characteristics, the standard images reconstructed by the MRI scanner have a rather low SNR and the spatial resolution is mostly limited to around 1 pixel/1.3 mm. Besides, this pulse sequence often causes contrast instabilities, Kellman and Arai [46], thus compromising the pertinence of the quantitative analysis of myocardial perfusion, with or without DCE-GRICS reconstruction. The residual local variability intensity-time curves observed after DCE-GRICS might be partly occasioned by these sequence imperfections.

5.4 Conclusion and Prospects

The initial target of these PhD studies was achieved by developing a new motion compensated image reconstruction method for Dynamic Contrast-Enhanced MRI. It performs non rigid motion compensation, in terms of both intra- and inter- image motion (motion artefacts correction and registration). The intensity-time curves are improved, in order to allow for more accurate regional perfusion assessment and blood blow quantification. The method was applied and validated for myocardial perfusion Dynamic Contrast-Enhanced MRI.

Application to other DCE-MRI examinations belongs to future work. The protocol for a clinical research trial was approved by the local ethics committee. Its purpose is to validate DCE-GRICS on patients and pathologies in different DCE-MRI applications disturbed by respiratory and cardiac motion, such as myocardial perfusion, renal perfusion, liver perfusion, etc. The final aim would be to quantify tissue blood flow by analysing intensity-time curves, compare the results to a gold-standard, and thus evaluate whether DCE-GRICS allows for a more accurate quantitative analysis of DCE-MRI and subsequent diagnosis and medical decisions. Several practical limitations hamper the application of DCE-GRICS to all DCE-MRI examinations: impossibility of changing the pulse sequences for patient examinations, performing them deliberately in free-breathing, small number of independent and relevant motion sensors, etc.

Dynamic Contrast-Enhanced MRI would highly benefit from accelerated acquisition, because it requires both high temporal and spatial resolution. However, DCE-GRICS showed robustness to very low undersampling factors. Therefore, a natural continuation of this work was to introduce temporal optimisation into DCE-GRICS, by coupling it with temporally optimised image reconstruction methods such as k-t SENSE. This research direction was explored during the stay at the Division of Imaging Sciences, King's College London, and the results are exposed in the following chapter.

Chapter 6

k-t SENSE and GRICS

The work described in this chapter has been conducted in collaboration with researchers at the Division of Imaging Sciences, King's College London, during the stay in London and afterwards. The purpose was to combine DCE-GRICS or GRICS with *k-t* SENSE, Tsao et al. [92], an image reconstruction method for undersampled dynamic data acquisitions, implemented on Philips MRI scanners used for research and for clinical examinations in London. Two reasons pointed to this research direction. First, accelerated acquisition is very useful and almost necessary for DCE-MRI, while the method developed for this PhD, DCE-GRICS, does not stand high acceleration. Second, *k-t* SENSE suffers sometimes from motion induced artefacts, namely when applied to myocardial perfusion DCE-MRI, and thus requires motion compensation. In the following sections, *k-t* SENSE is described in its original form and in optimised versions for different applications. Then, the work in the context of these PhD studies is presented: *k-t* SENSE was coupled with GRICS and DCE-GRICS, in order to provide a method for motion compensated image reconstruction of accelerated Dynamic Contrast-Enhanced MRI.

6.1 *k-t* SENSE

Many variations of the idea of SENSE, either in its simplified or general form, have emerged since the initial implementation by Pruessmann (Pruessmann et al. [71], Pruessmann et al. [72]). Different acquisition patterns and frameworks have been investigated, and different constraints and regularisations have been tested for the initial equations, from simple Tikhonov regularisation to Bayesian methods. For instance, the prior information has been introduced in terms of an approximated solution, obtained from a low resolution estimation, or a simpler more approximated reconstruction. All of these versions operate in the spatial image domain.

With the development of dynamic MRI, several attempts were made at

transposing and optimising this reconstruction approach for dynamic MRI, see 1.2.3. They are nowadays often referred to as *k-t* methods because they tend to transpose the optimisation of both acquisition and reconstruction in the (k-space)-time, or dually the (image space)-(temporal frequency) domain. One of these emerging methods is the *k-t* SENSE, Tsao et al. [92]. As suggested by its name, it focuses on extending the unaliasing idea of SENSE from image space domain to (image space)-(temporal frequency) domain.

6.1.1 Definition

Let's adopt a different point of view: until now, spatial domain data have been referred to as the "image". From now on, the "image" refers to data in the space(r)-temporal frequency(f) domain. Its Fourier Transform counterpart becomes the k-space(k)-time(t) domain. The sampling pattern is designed in the *k-t* domain, so that its corresponding point spread function (PSF) is defined in the space(r)-temporal frequency(f) domain. Therefore, undersampled data in *k-t* will result in aliasing in *r-f*, as illustrated in 6.1. The k dimension refers to the k-space basis vector, and r refers to the spatial basis vector.

If the generalised SENSE equation is transposed to this framework, and the coil sensitivities c are allowed to change in time, the following formulation is obtained:

$$s_{kt} = E\rho_{rf} = \xi_{kt} \cdot FT_{r\to k} \cdot c_{rt} \cdot FT_{f\to t} \cdot \rho_{rf} \tag{6.1}$$

The coil sensitivities provide additional spatial information for the unaliasing in space dimension. However, they do not really contribute to the unaliasing in the temporal frequency direction. Therefore, prior information has to be introduced to corroborate the unaliasing in time. The initial regularising approach in Tsao et al. [92] consisted in introducing statistical prior knowledge about noise and the imaged object in terms of covariance matrices, respectively Ψ_{kt} and M_{rf}, and solving the equation with the Wiener filter:

$$E^H\Psi_{kt}^{-1}s_{kt} = (E^H\Psi_{kt}^{-1}E + M_{rf}^{-1})\rho_{rf} \tag{6.2}$$

This is the generalised version of *k-t*, intended for arbitrary *k-t* acquisition pattern, and requiring iterative numerical solvers. As for SENSE, a simpler version of *k-t* SENSE can be formulated in the image domain for the case of Cartesian regular undersampling.

In the context of *k-t* acquisition patterns, regular Cartesian undersampling, which yields a simple aliasing PSF, becomes the sheared-grid acquisition pattern, as illustrated in Fig.6.1: for easier depiction of *k-t* acquisition patterns, the time axes is discretised, with each time point corresponding to the acquisition of one set of regularly undersampled (1 line out of $N_{AccFactor}$) phase-encoded lines, spanning the entire field of view. This line set is shifted in the phase-encoding direction by

a constant number of lines for each time point, which results in the sheared-grid pattern.

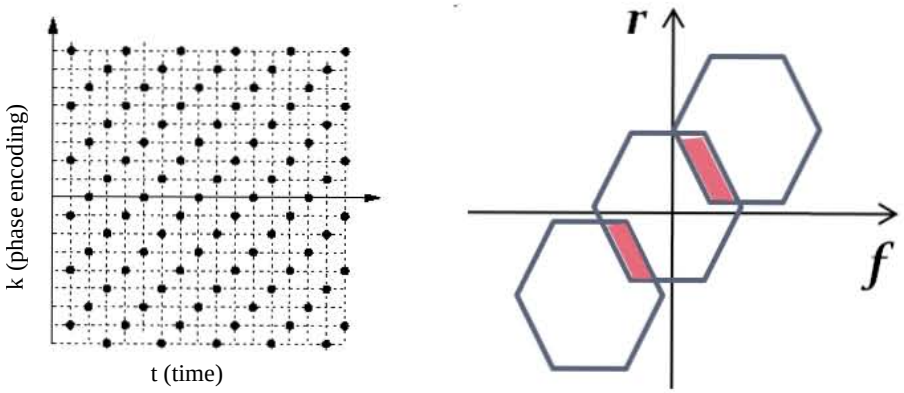

***Figure 6.1**: Illustration of the regular sheared-grid undersampled pattern for k-t SENSE, causing aliasing in r-f domain*

In this case, (6.2) can be simplified into:

$$(PSFc)^H \Psi_{kt}^{-1} \rho_{aliased,rf} = ((PSFc)^H \Psi_{kt}^{-1} PSFc + M_{rf}^{-1}) \rho_{rf} \tag{6.3}$$

As in SENSE, this problem can be divided into many smaller problems, and it is also solved in a direct manner with the Moore-Penrose inverse:

$$\rho_{rf} = ((PSFc)^H \Psi_{kt}^{-1} PSFc + M_{rf}^{-1})^{\dagger} (PSFc)^H \Psi_{kt}^{-1} \rho_{aliased,rf} \tag{6.4}$$

Since the result is in the *r-f* domain, additional FFT from f to t has be to performed, in order to obtain a temporal series of 2D or 3D spatial images.

If parallel imaging is not used, i.e. if there is only one receiver coil, the operator c is suppressed, and this version is known as *k-t*BLAST, because it was inspired by **BLAST**, Tsao et al. [91]. In this case, the equation is underdetermined, and the only constraint is the image prior. The difference between *k-t*BLAST and UNFOLD (see 1.2.3) lies in the fact that UNFOLD is designed so that no signal overlapping occurs, in order to be able to filter non-aliased data, whereas in *k-t*BLAST overlapping is allowed to occur to some extent, though it is reduced to the minimum. Therefore, *k-t*BLAST allows for higher acceleration factors, and is not as strictly limited by the spatial support as UNFOLD.

*k-t*FOCUSS (*k-t* space FOCal Underdetermined System Solver), Jung et al. [45] is a sort of a generalisation of *k-t*BLAST. It is a versatile iterative method: it employs l_2 norm, but, for the parameter $p = 0.5$ and infinite number of iteration, it converges towards a reconstruction which is optimal from the compressed sensing point of view. For the parameter $p = 1$, and only one iteration, it becomes equivalent to *k-t*BLAST.

6.1.2 Constraints

6.1.2.1 Noise

The noise covariance matrix is estimated from the undersampled data in *k-t* domain, by selecting automatically the border zone which contains mostly noise and calculating its variance. It is assumed that there is no coupling between coils and that noise from one coil is independent from other coils, so that noise covariance between different coils is equal to zero. Therefore, the noise covariance matrix has only diagonal non-zero elements (equal to noise variance from each coil). Additional acquisitions can also be used for estimating the noise covariance matrix, with both diagonal and non-diagonal elements.

6.1.2.2 Image prior

The prior estimate of the image (in *r-f* domain) is obtained from low-resolution, fully sampled training data, simply by applying FFT from *k-t* to *r-f*. This estimate has a much lower spatial resolution than the unknown image. In r direction, the global shape of the estimate is rather accurate, but in f direction the shape of the support might be tighter than it should be, with lower temporal frequency components. This occurs if some very small structures in the imaged object move or exhibit intensity changes, because they will not be much visible in the low-resolution estimate, and higher temporal frequencies will be less present in the estimate. This can cause slight temporal smoothing of the final solution. Also, the higher the undersampling, the more pixels form one aliased pixel, and the higher the requirements on the accuracy of the prior.

6.1.2.3 Other constraints

Initially, in Tsao et al. [92], an additional constraint was used: the image was assumed to be close to an estimated temporal mean value, so that only the deviation from this mean value was solved by the equation. For that purpose, an estimate of this temporal image mean was subtracted from both the aliased $\rho_{aliased,rf}$ and the unknown image ρ_{rf}. The estimate was formed from the aliased data, by taking the value at zero temporal frequency $\rho_{aliased,rf}(r, f = 0)$. However, this approach has the following disadvantage: when this mean is subtracted, the residual aliased image in 6.4 becomes 0 at its own centre $f = 0$, but it also becomes very close to 0 at the locations where the point $f = 0$ is folded over. The equations written for those points will become very poorly conditioned, thus jeopardising the recovery of those points. This constraint was more or less abandoned afterwards.

Various constraints can be added, but thorough attention has to be paid to their filtering properties, depending on the application and its diagnostic/medical use. For instance, if the spatial resolution is very important, and very small structures

are of interest, spatial smoothing can be dangerous for medical reading. Temporal filtering can be very problematic, especially in the case of DCE-MRI: as the estimation of diagnostic parameters is based on the post-processing of intensity-time curves, any degree of temporal smoothing can jeopardise detection and assessment of pathological tissue. Usually, a compromise has to be made between the conditioning of the system and filtering, although it is often very difficult to assess the required limits, especially in the case of pathologies, when the outcomes are difficult to predict and control.

6.1.3 Acquisition patterns

Initially, the training data were acquired before the undersampled data. This approach has several disadvantages: inconsistency may occur between training and actual undersampled data (due to motion, difference in parameters etc), and it is inapplicable to any acquisition which implies contrast agent injection, such as dynamic contrast-enhanced MRI. Therefore, training data were incorporated in the main acquisition: some central part of k-space is fully sampled for all time points, whereas other parts are heavily undersampled, as shown in Fig.6.2. Data acquired in this manner are then split into training and sheared-grid undersampled data. The number of central fully acquired lines and the undersampling factor have to be optimised, depending on the application. For instance, the application of *k-t* SENSE for real-time cardiac imaging has been optimised in Tsao et al. [93], and for myocardial perfusion in Plein et al. [70].

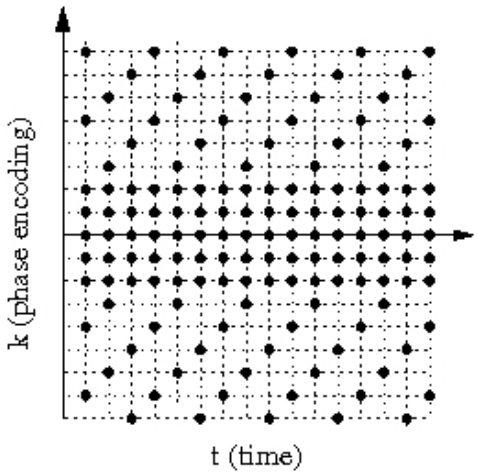

***Figure 6.2**: Sheared-grid regularly undersampled k-t SENSE sampling pattern with interleaved training data (fully sampled central part of k-t)*

6.1.4 Influence of motion

The unaliasing property of *k-t* SENSE depends on the PSF (in *r-f* domain) and the spatio-temporal support of the acquired data. The algorithm has been optimised in terms of sampling pattern and size of training data for different applications, with different spatio-temporal properties. If these properties unexpectedly change, if some unwanted and unpredicted motion occurs, the reconstruction quality might drop. Additional motion widens f profiles of some r parts of the image, and strenghtens some components, thus causing heavier aliasing, as illustrated in Fig.6.3. The conditioning of the equations containing these protuberant regions in f will be poorer. The result (in *r-t* domain) will present some residual aliasing, and the temporal behaviour of badly recovered regions will contain inaccuracies and smoothing.

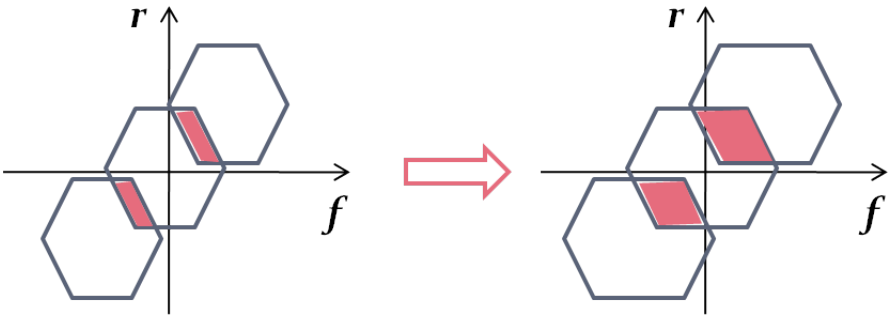

***Figure 6.3**: If some unpredicted additional motion occurs, the signal support in $r - f$ becomes wider, with stronger components, and the aliasing becomes heavier.*

In the application of *k-t* SENSE to myocardial perfusion DCE-MRI, cardiac motion is resolved with ECG triggering. Respiratory motion is dealt with by breath hold, though its duration is not sufficient for covering the whole dynamic acquisition. Usually, the patient is asked to hold his breath as long as possible, at least during the first pass of the contrast agent. Therefore, rather heavy respiratory motion may occur towards the end of the acquisition. Inter-TR respiratory motion can be reasonably neglected in *k-t* SENSE acquisitions, due to very swift acquisition of data in one cardiac cycle. However, respiratory motion between two time points in the *k-t* sampling pattern, each time point corresponding to a different cardiac cycle, can cause artefacts, and has to be accounted for.

This motion-related issue in *k-t* SENSE is the second argument for combining GRICS with *k-t* SENSE. If motion is compensated prior to the application of the unfolding *k-t* SENSE operator, the support of the image in the $r - f$ domain will be slightly reduced, and the spatio-temporal unaliasing will be easier to resolve.

6.2 *k-t* PCA

The prior information contained in the training data is very redundant and correlated, especially in time. Therefore, it could be compacted and reduced only to its important independent components. This was done in Pedersen et al. [69]: principal component analysis was performed on the training data P_{train}, resulting in the representation of P_{train} with weighting coefficients $W_{train}(x, f)$ in the coordinate system of its principal components in f dimension (contained in $B_{train}(f)$)):

$$P_{train}(r, f) = W_{train}(r)B_{train}(f) \tag{6.5}$$

The obtained principal components were rearranged to figure on the left side of matrix multiplication and then integrated in the *k-t* SENSE equation, by simply replacing the unknown image ρ_{rf} with precalculated principal components in B and unknown coefficients W:

$$\rho_{rf} = B_{train}(f)W(r) \tag{6.6}$$

Hence, the unknown image is assumed not to resemble directly the training data, but to have the same principal components as the training data. It is not reconstructed in terms of complex image intensities in *r-f* domain, but in terms of principal component weights W. The number of principal components and thus weights is less or equal than the number of samples in f direction. Hence the number of unknowns can be the same as for *k-t* SENSE, but with information compression, or reduced. In any way, the conditioning of the equation system is improved, depending on the number of principal components and the spatio-temporal properties of the data.

This framework has been extended and adapted to 3D myocardial perfusion imaging, Vitanis et al. [94]: compartmental-based processing attributes different principal components to differently enhancing regions in the heart.

6.3 DCE-GRICS with a k-t undersampled pattern

Since DCE-GRICS deals with temporal changes, in terms of both motion and contrast change, it would be interesting to change the standard linear sampling pattern into a sort of a k-t sampling pattern. This should be tested ideally by changing the pulse sequence, which is not feasible for tests on patients. Retrospective tests (here on the clinical data used for the validation of DCE-GRICS) can be easily biased, because the performance of the algorithm depends on the motion and contrast phase during which a k-space line was acquired. For instance, it would be biased to retrospectively test a k-t sheared grid sampling pattern without any undersampling, because there are 1-3 level changes in the respiratory phase during the acquisition of one image. However, it is rather reasonable to test retrospectively an undersampled sheared grid pattern with interleaved training

data, as used for k-t SENSE. Since the echo train length is 4 in the available data, a low undersampling factor of 2 or 4 does not change anything in the timing of the sequence with respect to motion. It would not be interesting to test higher undersampling factors anyway, because the conditioning of the equation system would be too poor.

Therefore, available clinical data were retrospectively undersampled in a sheared grid fashion with a factor of 2, and the central (training) part contained 32 lines. The net undersampling factor was 1.6, the same as for regular undersampling tests, see 5.3.2.5. The result was very similar to the test performed with the standard regular undersampling. The rms relative error between intensity-time curves from fully sampled and undersampled data was in average 2.2%, with a standard deviation of 3%, and an increase in noise was noticed. In conclusion, k-t undersampling didn't perform better than regular undersampling. An explanation to this is that DCE-GRICS does not have any additional tools for unfolding the image in the time frequency direction. By adopting the sheared grid pattern, the folding is diminished in the phase-encoding direction, which alleviates the requirements on the parallel imaging part of the algorithm, but the folding in time frequency appears, and there are no constraints to aid the unfolding, except maybe a feeble constraint imposed by the contrast change model. A better solution would consist in combining DCE-GRICS or GRICS with *k-t* SENSE.

6.4 Integration of DCE-GRICS/GRICS with k-t SENSE

Two main arguments corroborate the coupling of GRICS with *k-t* SENSE: motion is one of the main issues in *k-t* SENSE, and Dynamic Contrast-Enhanced MRI requires accelerated acquisition and methods for image reconstruction from undersampled data.

Introducing motion compensation into *k-t*SENSE comprises two tasks.

First, some motion compensation (here GRICS-like), has to be integrated into *k-t*SENSE unfolding operators. It is not feasible to integrate DCE-GRICS as it is into *k-t* SENSE, because the contrast change model is not compatible with the formulation of *k-t* SENSE. The contrast change model operates in $r-t$ domain, and reduces the number of unknowns in time, whereas *k-t* SENSE performs unfolding in $r-f$ domain. Therefore, the *k-t* SENSE unfolding operator was coupled with GRICS. If motion compensation is performed prior to the application of the *k-t* SENSE unfolding operator, the unaliasing task for this operator will be reduced, because of reduced signal support in $r-f$ space, and the solution will be easier to obtain.

Second, since the solution represents a motion compensated image, the training data have to be motion compensated as well, in order to be consistent.

6.4.1 Theory

6.4.1.1 *k-t* GRICS

The motion compensation in GRICS is performed by a spatial transformation operator T: it performs interpolation in space domain (r) based on displacements of each image voxel from t_1 to t_2 time instant. The term image will refer either to image in space (r), or image in space-temporal frequency domain ($r-f$), but it will be explicitely stated.

In order to reduce the f bandwidth of the unknown ($r-f$)image solved by k-t SENSE, motion has to be compensated prior to the unaliasing part of the algorithm. Since the spatial transformation operator corresponds to one time instant, it is not possible to apply it directly to ρ_{rf}. Therefore, and also in view of a generalised approach, the operator T was extended to the $r-t$ domain and integrated into the generalised version of k-t SENSE:

$$s_{kt} = E_{motion}\rho_{rf} \quad , \quad E_{motion} = \xi_{kt} \cdot FT_{r\to k} \cdot c_{rt} \cdot T_{rt} \cdot FT_{f\to t} \tag{6.7}$$

T_{rt} represents actually a temporal series of spatial transformations T, each T corresponding to one spatial image in the temporal series. In this manner, motion between spatial images in the temporal series (inter-image motion) is accounted for, but not the motion occurring during the acquisition of one spatial image (inter-TR motion). This is due to $FT_{f\to t}$, which operates on the whole $r-f$ data. For inter-TR motion to be compensated for in this framework, the $r-f$ image to be reconstructed would have to be larger in f, i.e. have a higher temporal resolution, which implies more unknowns and generates many other acquisition and reconstruction problems. This step caused one feature (inter-TR motion compensation) of GRICS to disappear. However, in current applications of k-t SENSE, the acquisition time for one frame is so short, due to rapid acquisition and high under-sampling, that the influence of inter-TR respiratory motion can be neglected.

The second GRICS equation is written as in DCE-GRICS, for each frame in the $r-t$ series.

6.4.1.2 Image prior

Since the training data have to be motion compensated as well, they were reconstructed with DCE-GRICS. The multi-resolution framework was eliminated due to low spatial resolution of the training data. The inter-TR motion correction was also removed, because the acquisition of one frame is too swift for intra-image respiratory motion to cause problems. So, DCE-GRICS performed registration of the training data. The prior was then extracted from the training data in the same manner as for standard k-t SENSE.

6.4.2 Validation

This new method was naturally applied to myocardial perfusion DCE-MRI accelerated with undersampled *k-t* SENSE acquisition pattern. Because of difficulties for acquiring actual undersampled myocardial perfusion DCE-MRI data with a non clinical sequence and in free-breathing, the method was first tested on retrospectively undersampled clinical data used for the validation of DCE-GRICS. Some additional tests were performed on actual available *k-t* SENSE data, but their features and parameters were not optimal for *k-t* GRICS.

6.4.2.1 Retrospectively undersampled clinical data

Clinical data, used for the validation of DCE-GRICS, were retrospectively undersampled in the *k-t* SENSE manner, with the following parameters. 16 full central k-space lines were selected for the training data, and the rest was undersampled with the sheared grid pattern and a factor of 4. The net undersampling factor was 3.

DCE-GRICS performed good motion compensation (registration) of the training data. Motion-time profiles are shown in Fig.6.4.

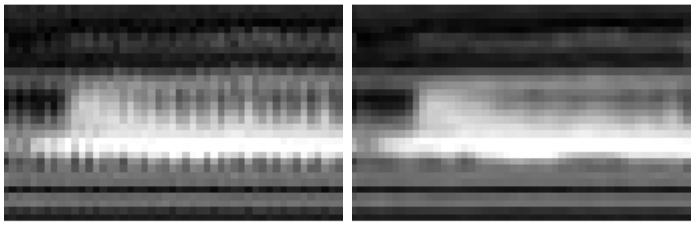

Figure 6.4*: Motion-time profiles after standard reconstruction (left) and DCE-GRICS (right) on retrospectively created k-t SENSE training data with 16 central lines*

k-t GRICS was then applied, and compared with the standard reconstruction from fully sampled data and with *k-t* SENSE (both without any motion compensation). The same method for validation was used as for DCE-GRICS. The registration was demonstrated with motion-time profiles, and the improvement of intensity-time curves was shown by visual comparison of the curves from myocardial segments for these 3 types of reconstruction. Motion-time profiles are shown on Fig.6.5, and present the motion compensation capacity of *k-t* GRICS for *k-t* SENSE undersampled data.

Intensity-time curves are shown on Fig.6.6. The variability, induced by respiratory motion, is visible in the curves after reconstructions without motion compensation (standard and *k-t* SENSE), whereas it is considerably reduced after *k-t* GRICS.

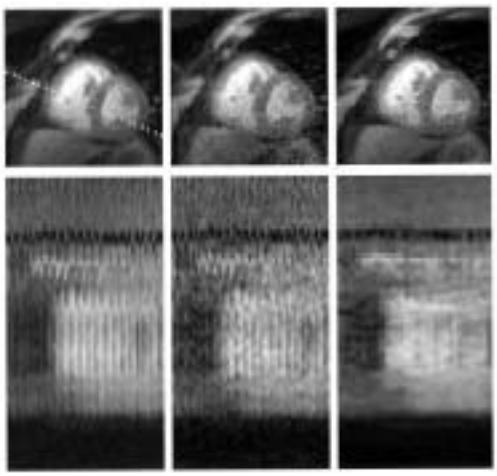

Figure 6.5*: Motion-time profiles (from left to right) after standard reconstruction from fully sampled data, k-t SENSE, (both without motion compensation), and after k-t GRICS performing motion compensation*

6.4.2.2 Actual *k-t* SENSE data

DCE-GRICS was also tested on real *k-t* SENSE training data. Such raw data were collected from clinical examinations of myocardial perfusion at the Division of Imaging Sciences, KCL, London. Acquisition was in 3D, with training data composed of 11 central k-space lines per cardiac cycle in phase encoding y direction. Data were acquired during 30s, with one undersampled/training 3D data set per cardiac cycle, in diastole. Partial Fourier was applied in y direction. The patient was asked to hold his breath as long as possible, at least during the first pass of the contrast agent. Therefore, the low resolution training image series presented no motion during the first 20s, but the last 10s showed rather strong respiratory motion. The dynamic image series reconstructed with the standard *k-t* SENSE (implemented on the scanner), presented good quality during breath hold, but aliasing artefact's appeared in the last 10 images, degraded image quality, and compromised quantification.

Since there was no physiological signals available, respiratory signals were generated manually for the first tests: two points were placed on each image in the temporal series, one at the endocardial border and one on the spleen. The position of selected points through time resulted in two respiratory signals, shown on Fig.6.7.

DCE-GRICS, modified for the training data, was further extended to 3D. The original size of the training data was 164x11x10, but they were zero-padded in phase encoding directions (y and z) in order to allow motion coefficient maps to be regularised in the second equation (regularisation-induced smoothing applied on 10-11 voxels would be aberrant).

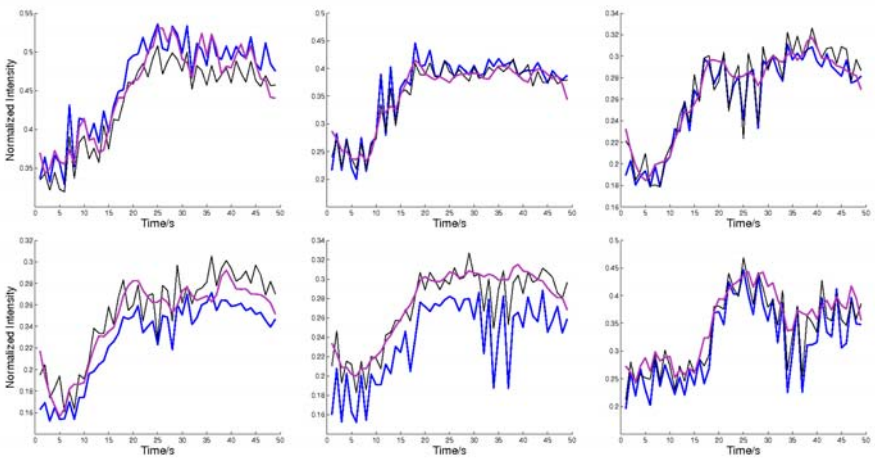

***Figure 6.6**: Intensity-time curves after standard reconstruction from fully sampled data (blue), k-t SENSE (black), both without motion compensation, and after motion compensated reconstruction k-t GRICS (pink)*

The result was unsuccessful: visually, almost the same motion appeared in the training data reconstructed with the sum-of-squares and with DCE-GRICS. The failure was attributed to very few data/equations available for the determination of motion coefficient maps: only the last 10 images presented motion and changes in respiratory signals, so that there were only 10 equations.

6.4.3 Discussion

An important problem encountered when working with DCE-MRI is the difficulty of performing test acquisitions. Usually only data acquired in the clinical setting under research protocols are available, and they often don't have

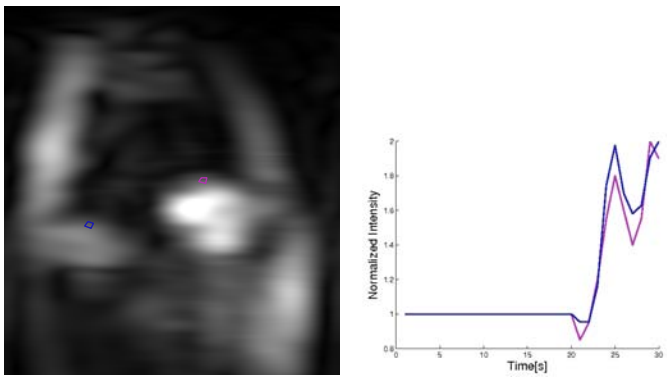

***Figure 6.7**: k-t SENSE training data: points selected manually on each image in the temporal series (left) and obtained respiratory signals (right)*

features optimal for the tested reconstruction algorithm. The alternative is to perform simulations, but they have to be extremely realistic to be useful. Performing a proper simulation involving realistic motion and contrast change is quite challenging. For instance, *k-t* SENSE was optimised for the support of the image in $r - f$ domain for myocardial perfusion imaging. As soon as the support changes slightly, the algorithm has to be optimised again. The results from actual *k-t* SENSE training data suggest that the acquisition should be preferably in free-breathing for this new method.

6.5 Conclusion and Prospects

A temporally optimised, motion compensated image reconstruction method for accelerated Dynamic Contrast-Enhanced MRI was developed and showed promising results. It has to be tested further on actual *k-t* SENSE data acquired in free-breathing and the undersampling factor has to be optimised.

Conclusion and Prospects

The initial goal of these doctoral studies was achieved: a new image reconstruction method, DCE-GRICS, has been developed for motion compensation of Dynamic Contrast-Enhanced MRI. It corrects for image artefacts and misregistration induced by non-rigid physiological motion. The method was applied and validated for the compensation of respiratory motion in myocardial perfusion DCE-MRI. This work resulted in several communications at french and international conferences, and in one peer-reviewed article in the journal Magnetic Resonance in Medicine. A clinical research trial has been approved and is to be carried out for testing and validating the diagnostic performance of DCE-GRICS, for different pathologies in several DCE-MRI applications (myocardial, renal, hepatic perfusion, ...). As DCE-MRI benefits highly from accelerated acquisition, the second part of these studies was dedicated to the coupling of DCE-GRICS with temporally optimised methods, namely *k-t* SENSE. This work resulted in a new method, *k-t* GRICS, which performs motion compensation of undersampled DCE-MRI. It was validated on retrospectively undersampled myocardial perfusion DCE-MRI, and further tests are to be performed on actual *k-t* SENSE data, acquired in free-breathing.

Conclusion et Perspectives

L'objectif initial de ces études doctorales a été atteint: une nouvelle méthode de reconstruction d'images, DCE-GRICS, a été développée afin de compenser le mouvement dans l'IRM dynamique avec rehaussement de contraste. La correction est effectuée sur les artéfacts de mouvement et les décalages dans les images, provoqués par le mouvement physiologique. La méthode a été appliquée et validée pour la compensation du mouvement respiratoire dans l'IRM de perfusion myocardique. Ce travail a abouti à plusieurs communications aux conférences françaises et internationales, ainsi qu'à un article dans le journal avec comité de lecture, Magnetic Resonance in Medicine. Un protocole de recherche clinique a été approuvé et sera mis en éxecution, afin de tester et valider la performance diagnostique de DCE-GRICS, pour différentes pathologies et plusieurs applications de l'IRM dynamique avec rehaussement de contraste (perfusion myocardique, rénale, hépatique, ...). Comme l'acquisition accélérée est très bénéfique pour l'IRM dynamique, la deuxième partie de ces études a été dédiée au couplage de DCE-GRICS avec les méthodes basées sur l'optimisation temporelle, notamment *k-t* SENSE. Ce travail a produit une nouvelle méthode, *k-t* GRICS, qui effectue la compensation de mouvement de l'IRM dynamique avec rehaussement de contraste sous-échantillonée. Cette méthode a été validée sur l'IRM de perfusion myocardique sous-échantillonée a posteriori, et des tests futurs vont être effectués sur de vraies données *k-t* SENSE, acquises en respiration libre.

Part III

Annexes

Appendix A

Data

This section lists the MRI data and physiological signals used in this work. They are described as entries in the local database ArchiMed, used in the IADI laboratory. Paths in the SVN database of Matlab codes are also given.

A.1 Physiological signals

Data in the ArchiMed database:
Research protocol 2008-014, Examination Code 01-00xV2, where $x \in 3, 9, 11, 12, 13, 14, 16, 17$, and Series numbers 4,5,6,7.

A.2 DCE-GRICS and *k-t* GRICS

Data in the ArchiMed database:
Study Code 650, Examination Codes 3TR500, 3TR501, 3TR529, 3TR530, 3TR542, 3TR543, Series numbers respectively 8, 9, 10, 10, 12, 10.
Matlab code in the SVN Database:
Applications/Research/SAEC/Reconstruction/DCE-GRICS/
Applications/Research/SAEC/Reconstruction/kt-GRICS/
Matlab code used during the thesis, saved on the server:
user/PhD/CodesCopy/
Results archived on the server:
user/PhD/Results/DCE-GRICS/
user/PhD/Results/ktGRICS/
user/PhD/Results/Article_DCE-GRICS (results published in the MRM article)

Bibliography

[1] A. H. Association. Standardized myocardial segmentation and nomenclature for tomographic imaging of the heart. a statement for healthcare professionals from the cardiac imaging committee of the council on clinical cardiology of the american heart association. *Int J Cardiovasc Imaging*, 18(1):539–42, 2002.

[2] D. Atkinson, D. L. Hill, P. N. Stoyle, P. E. Summers, S. Clare, R. Bowtell, and S. F. Keevil. Automatic compensation of motion artifacts in MRI. *Magn Reson Med*, 41(1):163–70, Jan. 1999.

[3] D. Atkinson, S. Counsell, J. V. Hajnal, P. G. Batchelor, D. L. G. Hill, and D. J. Larkman. Nonlinear phase correction of navigated multi-coil diffusion images. *Magnetic Resonance in Medicine: Official Journal of the Society of Magnetic Resonance in Medicine / Society of Magnetic Resonance in Medicine*, 56(5): 1135–1139, Nov. 2006.

[4] S. P. Awate, E. V. R. DiBella, T. Tasdizen, and R. T. Whitaker. Model-based image reconstruction for dynamic cardiac perfusion MRI from sparse data. *Conf Proc IEEE Eng Med Biol Soc*, 1:936–41, 2006.

[5] P. G. Batchelor, D. Atkinson, P. Irarrazaval, D. L. G. Hill, J. Hajnal, and D. Larkman. Matrix description of general motion correction applied to multishot images. *Magn Reson Med*, 54(5):1273–80, Nov. 2005.

[6] M. A. Bernstein, K. F. King, and X. J. Zhou. *Handbook of MRI pulse sequences*. Elsevier, 2004. ISBN 9780120928613.

[7] M. Bertero and P. Boccacci. *Introduction to inverse problems in imaging*. Institute of Physics Pub., 1998. ISBN 9780750304351.

[8] J. M. Blackall, S. Ahmad, M. E. Miquel, J. R. McClelland, D. B. Landau, and D. J. Hawkes. MRI-based measurements of respiratory motion variability and assessment of imaging strategies for radiotherapy planning. *Physics in Medicine and Biology*, 51(17):4147–4169, Sept. 2006.

[9] L. Bokacheva, H. Rusinek, Q. Chen, N. Oesingmann, C. Prince, M. Kaur, E. Kramer, and V. S. Lee. Quantitative determination of Gd-DTPA concentration in t1-weighted MR renography studies. *Magnetic Resonance in Medicine: Official Journal of the Society of Magnetic Resonance in Medicine / Society of Magnetic Resonance in Medicine*, 57(6):1012–1018, 2007.

[10] L. Bokacheva, H. Rusinek, J. L. Zhang, Q. Chen, and V. S. Lee. Estimates of glomerular filtration rate from MR renography and tracer kinetic models. *Journal of Magnetic Resonance Imaging: JMRI*, 29(2):371–382, 2009.

[11] A. C. S. Brau and J. H. Brittain. Generalized self-navigated motion detection technique: Preliminary investigation in abdominal imaging. *Magn Reson Med*, 55(2):263–70, 2006.

[12] F. A. Breuer, P. Kellman, M. A. Griswold, and P. M. Jakob. Dynamic autocalibrated parallel imaging using temporal GRAPPA (TGRAPPA). *Magnetic Resonance in Medicine: Official Journal of the Society of Magnetic Resonance in Medicine / Society of Magnetic Resonance in Medicine*, 53(4): 981–985, Apr. 2005.

[13] T. Brox, A. Bruhn, N. Papenberg, and J. Weickert. *High accuracy optical flow estimation based on a theory for warping*, volume 3024. 2004.

[14] M. Buehrer, K. P. Pruessmann, P. Boesiger, and S. Kozerke. Array compression for MRI with large coil arrays. *Magnetic Resonance in Medicine: Official Journal of the Society of Magnetic Resonance in Medicine / Society of Magnetic Resonance in Medicine*, 57(6):1131–1139, June 2007.

[15] M. Buehrer, J. Curcic, P. Boesiger, and S. Kozerke. Prospective self-gating for simultaneous compensation of cardiac and respiratory motion. *Magn Reson Med*, 60(3):683–90, Sept. 2008.

[16] M. Bydder, D. J. Larkman, and J. V. Hajnal. Detection and elimination of motion artifacts by regeneration of k-space. *Magnetic Resonance in Medicine: Official Journal of the Society of Magnetic Resonance in Medicine / Society of Magnetic Resonance in Medicine*, 47(4):677–686, Apr. 2002.

[17] D. W. Chakeres, A. Kangarlu, H. Boudoulas, and D. C. Young. Effect of static magnetic field exposure of up to 8 tesla on sequential human vital sign measurements. *Journal of Magnetic Resonance Imaging: JMRI*, 18(3): 346–352, Sept. 2003.

[18] T. F. Christian, D. W. Rettmann, A. H. Aletras, S. L. Liao, J. L. Taylor, R. S. Balaban, and A. E. Arai. Absolute myocardial perfusion in canines measured

by using dual-bolus first-pass MR imaging. *Radiology*, 232(3):677–684, Sept. 2004.

[19] N. Cindea, F. Odille, G. Bosser, J. Felblinger, and P. Vuissoz. Reconstruction from free-breathing cardiac MRI data using reproducing kernel hilbert spaces. *Magnetic Resonance in Medicine: Official Journal of the Society of Magnetic Resonance in Medicine / Society of Magnetic Resonance in Medicine*, 63(1): 59–67, Jan. 2010.

[20] M. E. Crowe, A. C. Larson, Q. Zhang, J. Carr, R. D. White, D. Li, and O. P. Simonetti. Automated rectilinear self-gated cardiac cine imaging. *Magn Reson Med*, 52(4):782–8, Oct. 2004.

[21] M. Doneva and P. Börnert. Automatic coil selection for channel reduction in SENSE-based parallel imaging. *Magma (New York, N.Y.)*, 21(3):187–196, May 2008.

[22] D. Donoho. Compressed sensing. *Information Theory, IEEE Transactions on*, 52(4):1289–1306, Apr. 2006.

[23] J. Du and M. Bydder. High-resolution time-resolved contrast-enhanced MR abdominal and pulmonary angiography using a spiral-TRICKS sequence. *Magnetic Resonance in Medicine: Official Journal of the Society of Magnetic Resonance in Medicine / Society of Magnetic Resonance in Medicine*, 58(3): 631–635, Sept. 2007.

[24] J. Du, T. J. Carroll, H. J. Wagner, K. Vigen, S. B. Fain, W. F. Block, F. R. Korosec, T. M. Grist, and C. A. Mistretta. Time-resolved, undersampled projection reconstruction imaging for high-resolution CE-MRA of the distal runoff vessels. *Magnetic Resonance in Medicine: Official Journal of the Society of Magnetic Resonance in Medicine / Society of Magnetic Resonance in Medicine*, 48(3):516–522, Sept. 2002.

[25] R. L. Ehman and J. P. Felmlee. Adaptive technique for high-definition MR imaging of moving structures. *Radiology*, 173(1):255–263, Oct. 1989.

[26] J. Felblinger and C. Boesch. Amplitude demodulation of the electrocardiogram signal (ECG) for respiration monitoring and compensation during MR examinations. *Magn Reson Med*, 38:129–36, 1997.

[27] J. Felblinger, C. Lehmann, and C. Boesch. Electrocardiogram acquisition during MR examinations for patient monitoring and sequence triggering. *Magnetic Resonance in Medicine: Official Journal of the Society of Magnetic Resonance in Medicine / Society of Magnetic Resonance in Medicine*, 32(4): 523–529, Oct. 1994.

[28] B. Fernandez, J. Oster, M. Lohezic, D. Mandry, O. Pietquin, P. Vuissoz, and J. Felblinger. Adaptive black blood fast spin echo for end-systolic rest cardiac imaging. *Magnetic Resonance in Medicine: Official Journal of the Society of Magnetic Resonance in Medicine / Society of Magnetic Resonance in Medicine*, 64(6):1760–1771, 2010.

[29] M. Filipovic, P. Vuissoz, A. Codreanu, M. Claudon, and J. Felblinger. Motion compensated reconstruction for free breathing dynamic contrast-enhanced MRI. In *ISMRM Conference*, 2009.

[30] M. Filipovic, P. Vuissoz, A. Codreanu, M. Claudon, and J. Felblinger. Motion compensated reconstruction for thoracoabdominal dynamic contrast-enhanced MRI in free-breathing. In *ISMRM Conference*, 2010.

[31] M. Filipovic, P. Vuissoz, A. Codreanu, M. Claudon, and J. Felblinger. Motion compensated generalized reconstruction for free-breathing dynamic contrast-enhanced MRI. *Magnetic Resonance in Medicine*, 65(3):812–822, 2011.

[32] M. A. Griswold, P. M. Jakob, R. M. Heidemann, M. Nittka, V. Jellus, J. Wang, B. Kiefer, and A. Haase. Generalized autocalibrating partially parallel acquisitions (GRAPPA). *Magn Reson Med*, 47(6):1202–10, 2002.

[33] E. M. Haacke. *Magnetic resonance imaging: physical principles and sequence design*. J. Wiley & Sons, 1999. ISBN 9780471351283.

[34] E. M. Haacke and J. L. Patrick. Reducing motion artifacts in two-dimensional fourier transform imaging. *Magnetic Resonance Imaging*, 4(4):359–376, 1986.

[35] F. Huang, J. Akao, S. Vijayakumar, G. R. Duensing, and M. Limkeman. k-t GRAPPA: a k-space implementation for dynamic MRI with high reduction factor. *Magn Reson Med*, 54(5):1172–84, Nov. 2005.

[36] F. Huang, S. Vijayakumar, Y. Li, S. Hertel, and G. R. Duensing. A software channel compression technique for faster reconstruction with many channels. *Magnetic Resonance Imaging*, 26(1):133–141, Jan. 2008.

[37] T. Ichihara, M. Ishida, K. Kitagawa, Y. Ichikawa, T. Natsume, N. Yamaki, H. Maeda, K. Takeda, and H. Sakuma. Quantitative analysis of first-pass contrast-enhanced myocardial perfusion MRI using a patlak plot method and blood saturation correction. *Magnetic Resonance in Medicine: Official Journal of the Society of Magnetic Resonance in Medicine / Society of Magnetic Resonance in Medicine*, 62(2):373–383, Aug. 2009.

[38] I. C. F. Ipsen and C. D. Meyer. The idea behind krylov methods. *The American Mathematical Monthly*, 105(10):889–899, Dec. 1998.

[39] C. Jahnke, I. Paetsch, S. Achenbach, B. Schnackenburg, R. Gebker, E. Fleck, and E. Nagel. Coronary MR imaging: breath-hold capability and patterns, coronary artery rest periods, and beta-blocker use. *Radiology*, 239(1):71–78, 2006.

[40] P. Jehenson, D. Duboc, T. Lavergne, L. Guize, F. Guerin, M. Degeorges, and A. Syrota. Change in human cardiac rhythm induced by a 2-T static magnetic field. *Radiology*, 166(1 Pt 1):227–230, Jan. 1988.

[41] M. Jerosch-Herold. Quantification of myocardial perfusion by cardiovascular magnetic resonance. *Journal of Cardiovascular Magnetic Resonance: Official Journal of the Society for Cardiovascular Magnetic Resonance*, 12:57, 2010.

[42] M. Jerosch-Herold, C. Swingen, and R. T. Seethamraju. Myocardial blood flow quantification with MRI by model-independent deconvolution. *Med Phys*, 29(5):886–97, 2002.

[43] P. Jhooti, J. Keegan, and D. N. Firmin. A fully automatic and highly efficient navigator gating technique for high-resolution free-breathing acquisitions: Continuously adaptive windowing strategy. *Magnetic Resonance in Medicine: Official Journal of the Society of Magnetic Resonance in Medicine / Society of Magnetic Resonance in Medicine*, 64(4):1015–1026, Oct. 2010.

[44] B. Jung, M. Markl, D. Foell, and J. Hennig. Investigating myocardial motion by MRI using tissue phase mapping. *European Journal of Cardio-Thoracic Surgery: Official Journal of the European Association for Cardio-Thoracic Surgery*, 29 Suppl 1:S150–157, 2006.

[45] H. Jung, J. C. Ye, and E. Y. Kim. Improved k-t BLAST and k-t SENSE using FOCUSS. *Phys Med Biol*, 52(11):3201–26, 2007.

[46] P. Kellman and A. E. Arai. Imaging sequences for first pass perfusion –a review. *J Cardiovasc Magn Reson*, 9(3):525–37, 2007.

[47] P. Kellman, F. H. Epstein, and E. R. McVeigh. Adaptive sensitivity encoding incorporating temporal filtering (TSENSE). *Magnetic Resonance in Medicine: Official Journal of the Society of Magnetic Resonance in Medicine / Society of Magnetic Resonance in Medicine*, 45(5):846–852, 2001.

[48] H. W. Korin, J. P. Felmlee, S. J. Riederer, and R. L. Ehman. Spatial-frequency-tuned markers and adaptive correction for rotational motion. *Magnetic Resonance in Medicine: Official Journal of the Society of Magnetic Resonance in Medicine / Society of Magnetic Resonance in Medicine*, 33(5): 663–669, 1995.

[49] F. R. Korosec, R. Frayne, T. M. Grist, and C. A. Mistretta. Time-resolved contrast-enhanced 3D MR angiography. *Magn Reson Med*, 36(3):345–51, Sept. 1996.

[50] D. J. Larkman and R. G. Nunes. Parallel magnetic resonance imaging. *Physics in Medicine and Biology*, 52(7):R15–55, Apr. 2007.

[51] A. C. Larson, R. D. White, G. Laub, E. R. McVeigh, D. Li, and O. P. Simonetti. Self-gated cardiac cine MRI. *Magn Reson Med*, 51(1):93–102, Jan. 2004.

[52] M. Lustig, D. Donoho, and J. M. Pauly. Sparse MRI: the application of compressed sensing for rapid MR imaging. *Magn Reson Med*, 58(6):1182–95, 2007.

[53] B. Madore. UNFOLD-SENSE: a parallel MRI method with self-calibration and artifact suppression. *Magnetic Resonance in Medicine: Official Journal of the Society of Magnetic Resonance in Medicine / Society of Magnetic Resonance in Medicine*, 52(2):310–320, 2004.

[54] B. Madore, G. H. Glover, and N. J. Pelc. Unaliasing by fourier-encoding the overlaps using the temporal dimension (UNFOLD), applied to cardiac imaging and fMRI. *Magnetic Resonance in Medicine: Official Journal of the Society of Magnetic Resonance in Medicine / Society of Magnetic Resonance in Medicine*, 42(5):813–828, Nov. 1999.

[55] F. Maes, A. Collignon, D. Vandermeulen, G. Marchal, and P. Suetens. Multimodality image registration by maximization of mutual information. *IEEE Transactions on Medical Imaging*, 16(2):187–198, Apr. 1997.

[56] J. Milles, R. J. van der Geest, M. Jerosch-Herold, J. H. C. Reiber, and B. P. F. Lelieveldt. Fully automated motion correction in first-pass myocardial perfusion MR image sequences. *IEEE Trans Med Imaging*, 27(11):1611–21, Nov. 2008.

[57] K. Nehrke and P. Boernert. Prospective correction of affine motion for arbitrary MR sequences on a clinical scanner. *Magn Reson Med*, 54(5):1130–8, Nov. 2005.

[58] K. Nehrke, P. Boernert, D. Manke, and J. C. Boeck. Free-breathing cardiac MR imaging: study of implications of respiratory motion–initial results. *Radiology*, 220(3):810–815, Sept. 2001.

[59] F. Odille, C. Pasquier, R. Abaecherli, P. Vuissoz, G. P. Zientara, and J. Felblinger. Noise cancellation signal processing method and computer

system for improved real-time electrocardiogram artifact correction during MRI data acquisition. *IEEE Trans Biomed Eng*, 54(4):630–40, 2007.

[60] F. Odille, N. Cindea, D. Mandry, C. Pasquier, P. Vuissoz, and J. Felblinger. Generalized MRI reconstruction including elastic physiological motion and coil sensitivity encoding. *Magn Reson Med*, 59(6):1401–11, 2008.

[61] F. Odille, P. Vuissoz, P. Marie, and J. Felblinger. Generalized reconstruction by inversion of coupled systems (GRICS) applied to free-breathing MRI. *Magn Reson Med*, 60(1):146–57, 2008.

[62] F. Odille, S. Uribe, P. G. Batchelor, C. Prieto, T. Schaeffter, and D. Atkinson. Model-based reconstruction for cardiac cine MRI without ECG or breath holding. *Magnetic Resonance in Medicine*, 63(5):1247–57, 2010.

[63] M. B. Ooi, S. Krueger, W. J. Thomas, S. V. Swaminathan, and T. R. Brown. Prospective real-time correction for arbitrary head motion using active markers. *Magnetic Resonance in Medicine: Official Journal of the Society of Magnetic Resonance in Medicine / Society of Magnetic Resonance in Medicine*, 62(4):943–954, Oct. 2009.

[64] J. Oster, O. Pietquin, R. Abaecherli, M. Kraemer, and J. Felblinger. Independent component analysis-based artefact reduction: application to the electrocardiogram for improved magnetic resonance imaging triggering. *Physiological Measurement*, 30(12):1381–1397, 2009.

[65] J. Oster, O. Pietquin, M. Kraemer, and J. Felblinger. Nonlinear bayesian filtering for denoising of electrocardiograms acquired in a magnetic resonance environment. *IEEE Transactions on Bio-Medical Engineering*, 57(7): 1628–1638, 2010.

[66] N. A. Pack, E. V. R. DiBella, T. C. Rust, D. J. Kadrmas, C. J. McGann, R. Butterfield, P. E. Christian, and J. M. Hoffman. Estimating myocardial perfusion from dynamic contrast-enhanced CMR with a model-independent deconvolution method. *J Cardiovasc Magn Reson*, 10(1):52, 2008.

[67] G. J. M. Parker, C. Roberts, A. Macdonald, G. A. Buonaccorsi, S. Cheung, D. L. Buckley, A. Jackson, Y. Watson, K. Davies, and G. C. Jayson. Experimentally-derived functional form for a population-averaged high-temporal-resolution arterial input function for dynamic contrast-enhanced MRI. *Magn Reson Med*, 56(5):993–1000, Nov. 2006.

[68] H. Pedersen, S. Kelle, S. Ringgaard, B. Schnackenburg, E. Nagel, K. Nehrke, and W. Y. Kim. Quantification of myocardial perfusion using free-breathing

MRI and prospective slice tracking. *Magn Reson Med*, 61(3):734–8, Mar. 2009.

[69] H. Pedersen, S. Kozerke, S. Ringgaard, K. Nehrke, and W. Y. Kim. k-t PCA: temporally constrained k-t BLAST reconstruction using principal component analysis. *Magn Reson Med*, 62(3):706–16, Sept. 2009.

[70] S. Plein, S. Ryf, J. Schwitter, A. Radjenovic, P. Boesiger, and S. Kozerke. Dynamic contrast-enhanced myocardial perfusion MRI accelerated with k-t sense. *Magnetic Resonance in Medicine: Official Journal of the Society of Magnetic Resonance in Medicine / Society of Magnetic Resonance in Medicine*, 58(4):777–785, Oct. 2007.

[71] K. P. Pruessmann, M. Weiger, M. B. Scheidegger, and P. Boesiger. SENSE: sensitivity encoding for fast MRI. *Magn Reson Med*, 42(5):952–62, Nov. 1999.

[72] K. P. Pruessmann, M. Weiger, and P. Boesiger. Sensitivity encoded cardiac MRI. *J Cardiovasc Magn Reson*, 3(1):1–9, 2001.

[73] L. Qin, P. van Gelderen, J. A. Derbyshire, F. Jin, J. Lee, J. A. de Zwart, Y. Tao, and J. H. Duyn. Prospective head-movement correction for high-resolution MRI using an in-bore optical tracking system. *Magnetic Resonance in Medicine: Official Journal of the Society of Magnetic Resonance in Medicine / Society of Magnetic Resonance in Medicine*, 62(4):924–934, Oct. 2009.

[74] A. J. Raper, D. W. Richardson, H. A. Kontos, and J. L. Patterson. Circulatory responses to breath holding in man. *Journal of Applied Physiology*, 22(2): 201–206, 1967.

[75] P. M. Robson, A. K. Grant, A. J. Madhuranthakam, R. Lattanzi, D. K. Sodickson, and C. A. McKenzie. Comprehensive quantification of signal-to-noise ratio and g-factor for image-based and k-space-based parallel imaging reconstructions. *Magnetic Resonance in Medicine: Official Journal of the Society of Magnetic Resonance in Medicine / Society of Magnetic Resonance in Medicine*, 60(4):895–907, Oct. 2008.

[76] P. B. Roemer, W. A. Edelstein, C. E. Hayes, S. P. Souza, and O. M. Mueller. The NMR phased array. *Magnetic Resonance in Medicine: Official Journal of the Society of Magnetic Resonance in Medicine / Society of Magnetic Resonance in Medicine*, 16(2):192–225, Nov. 1990.

[77] L. Rousselet, M. Filipovic, Z. Ramdan-Cherif, V. Laurent, C. Pasquier, and J. Felblinger. MR compatible sensor for measuring respiratory motion based on acceleration. Hawaii, 2010.

[78] L. Rousselet, S. Jovanovic, C. Pasquier, and J. Felblinger. Advantages of digital vs analog accelerometer-based sensor for respiratory motion correction. Sweden, 2011.

[79] D. Rueckert, L. I. Sonoda, C. Hayes, D. L. Hill, M. O. Leach, and D. J. Hawkes. Nonrigid registration using free-form deformations: application to breast MR images. *IEEE Trans Med Imaging*, 18(8):712–21, 1999.

[80] Y. S. Saad. GMRES: a generalized minimal residual algorithm for solving nonsymmetric linear systems. *SIAM J. Sci. Stat. Comput.*, 7:856–869, 1986.

[81] J. A. Schnabel, D. Rueckert, M. Quist, J. M. Blackall, A. D. C. Smith, T. Hartkens, G. P. Penney, W. A. Hall, H. Liu, C. L. Truwit, F. A. Gerritsen, D. L. G. Hill, and D. J. Hawkes. A generic framework for non-rigid registration based on non-uniform multi-level free-form deformation. *In Fourth Int. Conf. on Medical Image Computing and Computer-Assisted Intervention (MICCAI '01)*, 1:573–581, 2001.

[82] J. Schwitter. Myocardial perfusion. *Journal of Magnetic Resonance Imaging: JMRI*, 24(5):953–963, Nov. 2006.

[83] J. Schwitter, C. M. Wacker, A. C. van Rossum, M. Lombardi, N. Al-Saadi, H. Ahlstrom, T. Dill, H. B. W. Larsson, S. D. Flamm, M. Marquardt, and L. Johansson. MR-IMPACT: comparison of perfusion-cardiac magnetic resonance with single-photon emission computed tomography for the detection of coronary artery disease in a multicentre, multivendor, randomized trial. *European Heart Journal*, 29(4):480–489, Feb. 2008.

[84] A. D. Scott, J. Keegan, and D. N. Firmin. Motion in cardiovascular MR imaging. *Radiology*, 250(2):331–51, 2009.

[85] G. S. Slavin, S. D. Wolff, S. N. Gupta, and T. K. Foo. First-pass myocardial perfusion MR imaging with interleaved notched saturation: feasibility study. *Radiology*, 219(1):258–63, 2001.

[86] D. K. Sodickson and W. J. Manning. Simultaneous acquisition of spatial harmonics (SMASH): fast imaging with radiofrequency coil arrays. *Magn Reson Med*, 38(4):591–603, Oct. 1997.

[87] S. Sourbron, M. Dujardin, S. Makkat, and R. Luypaert. Pixel-by-pixel deconvolution of bolus-tracking data: optimization and implementation. *Physics in Medicine and Biology*, 52(2):429–447, Jan. 2007.

[88] R. B. Thompson and E. R. McVeigh. Cardiorespiratory-resolved magnetic resonance imaging: measuring respiratory modulation of cardiac function. *Magn Reson Med*, 56(6):1301–10, 2006.

[89] P. S. Tofts, G. Brix, D. L. Buckley, J. L. Evelhoch, E. Henderson, M. V. Knopp, H. B. Larsson, T. Y. Lee, N. A. Mayr, G. J. Parker, R. E. Port, J. Taylor, and R. M. Weisskoff. Estimating kinetic parameters from dynamic contrast-enhanced t(1)-weighted MRI of a diffusable tracer: standardized quantities and symbols. *J Magn Reson Imaging*, 10(3):223–32, Sept. 1999.

[90] J. Tsao. On the UNFOLD method. *Magnetic Resonance in Medicine: Official Journal of the Society of Magnetic Resonance in Medicine / Society of Magnetic Resonance in Medicine*, 47(1):202–207, Jan. 2002.

[91] J. Tsao, B. Behnia, and A. G. Webb. Unifying linear prior-information-driven methods for accelerated image acquisition. *Magnetic Resonance in Medicine: Official Journal of the Society of Magnetic Resonance in Medicine / Society of Magnetic Resonance in Medicine*, 46(4):652–660, Oct. 2001.

[92] J. Tsao, P. Boesiger, and K. P. Pruessmann. k-t BLAST and k-t SENSE: dynamic MRI with high frame rate exploiting spatiotemporal correlations. *Magn Reson Med*, 50(5):1031–42, Nov. 2003.

[93] J. Tsao, S. Kozerke, P. Boesiger, and K. P. Pruessmann. Optimizing spatiotemporal sampling for k-t BLAST and k-t SENSE: application to high-resolution real-time cardiac steady-state free precession. *Magnetic Resonance in Medicine: Official Journal of the Society of Magnetic Resonance in Medicine / Society of Magnetic Resonance in Medicine*, 53(6):1372–1382, 2005.

[94] V. Vitanis, R. Manka, D. Giese, H. Pedersen, S. Plein, P. Boesiger, and S. Kozerke. High resolution three-dimensional cardiac perfusion imaging using compartment-based k-t principal component analysis. *Magnetic Resonance in Medicine: Official Journal of the Society of Magnetic Resonance in Medicine / Society of Magnetic Resonance in Medicine*, Oct. 2010.

[95] M. von Siebenthal, G. Szekely, U. Gamper, P. Boesiger, A. Lomax, and P. Cattin. 4D MR imaging of respiratory organ motion and its variability. *Physics in Medicine and Biology*, 52(6):1547–1564, Mar. 2007.

[96] Y. Wang. Description of parallel imaging in MRI using multiple coils. *Magnetic Resonance in Medicine: Official Journal of the Society of Magnetic Resonance in Medicine / Society of Magnetic Resonance in Medicine*, 44(3): 495–499, Sept. 2000.

[97] M. J. White, D. J. Hawkes, A. Melbourne, D. J. Collins, C. Coolens, M. Hawkins, M. O. Leach, and D. Atkinson. Motion artifact correction in free-breathing abdominal MRI using overlapping partial samples to recover image deformations. *Magn Reson Med*, 62(2):440–9, 2009.

[98] G. Wollny, M. J. Ledesma-Carbayo, P. Kellman, and A. Santos. Exploiting quasiperiodicity in motion correction of free-breathing myocardial perfusion MRI. *IEEE Transactions on Medical Imaging*, 29(8):1516–1527, Aug. 2010.

[99] K. K. Wong, E. S. Yang, E. X. Wu, H. Tse, and S. T. Wong. First-pass myocardial perfusion image registration by maximization of normalized mutual information. *J Magn Reson Imaging*, 27(3):529–37, Mar. 2008.

[100] M. L. Wood and R. M. Henkelman. MR image artifacts from periodic motion. *Medical Physics*, 12(2):143–151, 1985.

[101] E. N. Yeh, C. A. McKenzie, M. A. Ohliger, and D. K. Sodickson. Parallel magnetic resonance imaging with adaptive radius in k-space (PARS): constrained image reconstruction using k-space locality in radiofrequency coil encoded data. *Magnetic Resonance in Medicine: Official Journal of the Society of Magnetic Resonance in Medicine / Society of Magnetic Resonance in Medicine*, 53(6):1383–1392, June 2005.

[102] M. Zaitsev, C. Dold, G. Sakas, J. Hennig, and O. Speck. Magnetic resonance imaging of freely moving objects: prospective real-time motion correction using an external optical motion tracking system. *NeuroImage*, 31(3): 1038–1050, 2006.

[103] L. K. Zierler. Theoretical basis of Indicator-Dilution methods for measuring flow and volume. *Circulation Research*, 10(3):393–407, 1962.

[104] E. M. Zimmermann and M. M. Al-Hawary. MRI of the small bowel in patients with crohn's disease. *Current Opinion in Gastroenterology*, 27(2):132–138, Mar. 2011.

Title : *Application of adaptive techniques to Magnetic Resonance Imaging of perfusion*

Abstract : Magnetic Resonance Imaging (MRI) requires tools for managing physiological and other motion of the patient. The generation of MR images consists of three steps: data acquisition with a pulse sequence, image reconstruction and image post-processing. Adaptive image reconstruction techniques aim at integrating motion information into the process of image generation from the acquired data, in order to compensate for motion-induced artefacts and problems. Dynamic contrast-enhanced (DCE) MRI is a technique designed for assessing the function of organs, by following dynamically the passage of a contrast agent in the body after a bolus injection. Motion-induced problems, especially in abdominal and thoracic DCE-MRI, consist of motion artefacts and misregistration. A new image reconstruction method, DCE-GRICS (Dynamic Contrast-Enhanced Generalized Reconstruction by Inversion of Coupled Systems), has been developed for solving these issues. Motion is estimated with a non rigid linear model based on physiological signals obtained from external sensors. Dynamic intensity changes caused by the passage of the contrast agent are described using a linear contrast change model based on B-splines. The method is applied and validated on myocardial perfusion imaging. Motion-induced inaccuracies in intensity-time curves are compensated, in order to allow for more reliable myocardial perfusion quantification by curve post-processing.

Key words : Magnetic Resonance Imaging, Image reconstruction, Motion, Myocardial perfusion

---

Titre: *Application des techniques adaptatives à l'Imagerie par Résonance Magnétique de perfusion*

Résumé: L'Imagerie par Résonance Magnétique (IRM) nécessite des outils pour gérer le mouvement physiologique et autre du patient. La création des images par l'IRM comporte trois étapes: l'acquisition des données avec une séquence d'impulsions, la reconstruction d'images, et le post-traitement. Les techniques adaptatives de reconstruction d'images visent à intégrer des informations liées au mouvement dans le processus de génération d'images à partir de données acquises, ceci dans le but de compenser les artéfacts et problèmes provoqués par le mouvement. L'IRM dynamique avec rehaussement de contraste est une technique destinée à l'estimation de la fonction d'organes, en suivant le passage d'un produit de contrast dans le corps. Les problèmes dus au mouvement, surtout dans l'application thoraco-abdominale de cette technique, se présentent sous forme d'artéfacts de mouvement et de décalages. Une nouvelle méthode de reconstruction d'images, DCE-GRICS (Reconstruction généralisée dynamique avec rehaussement de contraste par inversion des systèmes couplés), a été développée pour résoudre ces problèmes. Le mouvement est estimé avec un modèle linéaire non rigide basé sur les signaux physiologiques issus de capteurs externes. Les changements d'intensité causés par le passage de l'agent de contraste sont rendus avec un modèle linéaire de changement de contraste basé sur les fonctions B-spline. Cette méthode a été appliquée et validée sur l'imagerie de la perfusion myocardique. Les inexactitudes causées par le mouvement dans les courbes intensité-temps sont compensées, afin de rendre plus fiable le post-tratement des courbes pour l'estimation de la perfusion myocardique.

Mots clé: Imagerie par Résonance Magnétique, Reconstruction d'images, Mouvement, Perfusion myocardique